# Quantum statistical van der Waals equation and its QCD applications

Dissertation
zur Erlangung des Doktorgrades
der Naturwissenschaften

vorgelegt beim Fachbereich Physik
der Johann Wolfgang Goethe - Universität
in Frankfurt am Main

von
Volodymyr Vovchenko
aus Kiew, Ukraine

Frankfurt am Main 2017
(D 30)

vom Fachbereich Physik der

Johann Wolfgang Goethe-Universität als Dissertation angenommen.

Dekan: Prof. Dr. O. Philipsen

Gutachter: Prof. Dr. H. Stoecker

Prof. Dr. C. Greiner

Datum der Disputation: 9. März 2018

# Abstract

The theory of strong interactions – Quantum Chromodynamics (QCD) – is well-defined mathematically. However, direct applications of this theory to experiment are rather limited due to significant technical obstacles. Even some general features of QCD remain unclear to date. Hence, phenomenological input is important and needed for practical applications, e.g. for theoretical analysis of the heavy-ion collision experiments.

In this thesis the role of hadronic interactions is studied in the hadron resonance gas (HRG) model – a popular model for the confined phase of QCD. The description of hadronic interactions is based on the famous van der Waals (VDW) equation and its quantum statistical generalization. While this is not the conventional choice for nuclear/hadronic physics applications, the simplicity of the VDW approach makes it extremely useful. In particular, this framework allows to include the two most basic ingredients of hadron-hadron interaction: the short-range repulsion, modeled by excluded-volume (EV) corrections, and the intermediate range attraction.

The first part of the thesis considers just the repulsive EV interactions between hadrons. A hitherto unknown, but surprisingly strong sensitivity of the long known thermal fits to heavy-ion hadron yield data to the choice of hadron eigenvolumes is uncovered. It challenges the robustness of the chemical freeze-out temperature and baryochemical potential determination from the thermal fits. However, at the same time, the extracted value of the entropy per baryon is found to be a robust observable which depends weakly on this systematic uncertainty of the HRG model. A Monte Carlo procedure to treat EV interactions in HRG is also introduced in this thesis. It allows to study simultaneous effects of EV and of exact charge conservation in HRG for the first time.

Generalizations of the classical VDW equation are required for its applications in hadronic physics. The grand canonical ensemble (GCE) formulation of the classical VDW equation is presented. Remarkably, this important aspect of the VDW equation was not discovered before. The GCE formulation yields the analytic structure of the critical fluctuations, both in the vicinity of and far off the critical point. These critical fluctuations are presently actively being used as probes for the QCD critical point.

Another extension is the hitherto undiscovered generalization of the VDW equation to include quantum Bose-Einstein and Fermi-Dirac statistics. It is performed for both single-component and multi-component fluids. The Fermi-Dirac VDW equation is applied for the first time. It is used to describe nucleons and basic properties of nuclear matter. The quantum statistical generalization of the VDW equation developed in this work is quite general, and can be applied for any fluid. Thus, its applications are not restricted to QCD physics, but may also find themselves in chemistry and/or industry.

The quantum statistical VDW equation is used to describe baryonic interactions in full HRG. The VDW parameters $a$ and $b$ are fixed to the nuclear ground state and the predictions of the model are confronted with lattice QCD calculations. The inclusion of baryonic interactions leads to a qualitatively different behavior of the fluctuations of conserved charges in the crossover region. In many cases it resembles the lattice data. These results suggest that hadrons do not melt quickly with increasing temperature, as one could conclude on the basis of the common simple ideal HRG model. Calculations at finite chemical potentials show that the nuclear liquid-gas transition manifests itself by non-trivial fluctuations of the net baryon number in heavy ion collisions.

In the final part of the thesis the pure glue initial scenario for high-energy hadron and heavy-ion collisions is explored. This scenario is shown not to spoil the existing agreement of the hadronic and electromagnetic observables description in Pb+Pb collisions at energies available at the CERN Large Hadron Collider. Hydrodynamic calculations suggest that collisions of small-sized nuclei at lower collision energies available at the BNL Relativistic Heavy Ion Collider are promising in the search for the traces of the chemically non-equilibrium gluon-dominated phase transition.

# Zusammenfassung

Diese Arbeit basiert auf folgenden Publikationen:

- "Hadron resonance gas equation of state from lattice QCD"
  V. Vovchenko, D. V. Anchishkin, M. I. Gorenstein
  Physical Review C **91**, 024905 (2015) [56]

- "Hadron multiplicities and chemical freeze-out conditions in proton-proton and nucleus-nucleus collisions"
  V. Vovchenko, V. V. Begun, M. I. Gorenstein
  Physical Review C **93**, 064906 (2016) [59]

- "Surprisingly large uncertainties in temperature extraction from thermal fits to hadron yield data at LHC"
  V. Vovchenko, H. Stoecker
  Journal of Physics G **44**, 055103 (2017) [60]

- "Examination of the sensitivity of the thermal fits to heavy-ion hadron yield data to the modeling of the eigenvolume interactions"
  V. Vovchenko, H. Stoecker
  Physical Review C **95**, 044904 (2017) [61]

- "Chemical freeze-out conditions in hadron resonance gas"
  V. Vovchenko, M. I. Gorenstein, L. M. Satarov, H. Stoecker
  in "New Horizons in Fundamental Physics" of FIAS Interdisciplinary Science Series, pp. 127-137 (2017) [62]

- "Analysis of hadron yield data within hadron resonance gas model with multi-component eigenvolume corrections"

V. Vovchenko, H. Stoecker

Journal Physics: Conference Series **779**, 012078 (2017) [63]

- "Particle number fluctuations for the van der Waals equation of state"
  V. Vovchenko, D. V. Anchishkin, M. I. Gorenstein
  Journal of Physics A **48**, 305001 (2015) [125]

- "Non-Gaussian particle number fluctuations in vicinity of the critical point for van der Waals equation of state"
  V. Vovchenko, R. V. Poberezhnyuk, D. V. Anchishkin, M. I. Gorenstein
  Journal of Physics A **49**, 015003 (2016) [126]

- "Van der Waals Equation of State with Fermi Statistics for Nuclear Matter"
  V. Vovchenko, D. V. Anchishkin, M. I. Gorenstein
  Physical Review C **91**, 064314 (2015) [138]

- "Scaled variance, skewness, and kurtosis near the critical point of nuclear matter"
  V. Vovchenko, D. V. Anchishkin, M. I. Gorenstein, R. V. Poberezhnyuk
  Physical Review C **92**, 054901 (2015) [139]

- "Equations of state for real gases on the nuclear scale"
  V. Vovchenko
  Physical Review C **96**, 015206 (2017) [140]

- "van der Waals Interactions in Hadron Resonance Gas: From Nuclear Matter to Lattice QCD"
  V. Vovchenko, M. I. Gorenstein, H. Stoecker
  Physical Review Letters **118**, 182301 (2017) [166]

- "Entropy production in chemically nonequilibrium quark-gluon plasma created in central Pb+Pb collisions at energies available at the CERN Large Hadron Collider"
  V. Vovchenko, M. I. Gorenstein, L. M. Satarov, I. N. Mishustin, L. P. Csernai, I. Kisel, H. Stoecker
  Physical Review C **93**, 014906 (2016) [192]

- "Electromagnetic probes of a pure-glue initial state in nucleus-nucleus collisions at energies available at the CERN Large Hadron Collider"
  V. Vovchenko, Iu. A. Karpenko, M. I. Gorenstein, L. M. Satarov, I. N. Mishustin, B. Kämpfer, H. Stoecker
  Physical Review C **94**, 024906 (2016) [193]

- "Hydrodynamic modeling of a pure-glue initial scenario in high-energy hadron and heavy-ion collisions"
  V. Vovchenko, L. G. Pang, H. Niemi, Iu. A. Karpenko, M. I. Gorenstein, L. M. Satarov, I. N. Mishustin, B. Kämpfer, H. Stoecker
  Proceedings of Science BORMIO **2016**, 039 (2016) [194]

## Einführung

Die Theorie der starken Wechselwirkung – Quantenchromodynamik (QCD) – ist mathematisch wohldefiniert. Nichtsdestotrotz, direkte Anwendungen dieser Theorie auf Experimente sind wegen signifikantem technischen Aufwand bis heute begrenzt: Selbst die allgemeinsten Eigenschaften der QCD sind bis heute nicht gänzlich verstanden. Folglich sind für theoretische Beschreibungen von Schwerionen-Kollisionen auch phänomenologische Zugänge notwendig.

In dieser Arbeit erforschen wir die Rolle hadronischer Wechselwirkungen im Rahmen des Hadronen-Resonanz-Gas (HRG) Modells, was ein weit verbreitetes Modell für die Confined Phase der QCD ist. Die Beschreibung der hadronischen Wechselwirkungen basiert hier auf der bekannten van-der-Waals-Gleichung. Es handelt sich hierbei nicht um die meist verbreitete Wahl im Bereich der Kern- und Hadronen-Physik, sie stellt aber einen einfachen und nützlichen Zugang dar. Insbesondere erlaubt dieser die Einbeziehung der beiden wichtigsten Bestandteile der Wechselwirkung zwischen Hadronen: kurzreichweitige Abstoßung, modelliert durch die Eigenvolumen-Korrektur, sowie die Anziehung auf mittleren Abstandsskalen. In dieser Arbeit wird das seit rund 150 Jahren erfolgreich in der Chemie genutzte einfache VDW-Gas Modell erstmals weiterentwickelt: in diesem neuen Formalismus wird die konsistente quantenstatistische Beschreibung in das VDW Modell eingeführt.

## Eigenvolumen-Wechselwirkung im Hadronen-Resonanz-Gas

Der konventionelle Zugang über punktuelle Wechselwirkung im Rahmen des Modells des Hadronen-Resonanz-Gases wurde schon seit längerem verwendet, um thermodynamische Parameter der erzeugten Materie in Schwerionen-Kollisionen abzuschätzen. Die umfangreichen experimentellen Daten bzgl. mittlerer Hadronen-Multiplizitäten verschiedener Experimente wird durch dieses Modell relativ gut beschrieben. Bei Temperaturen im Bereich von $T \sim 100 - 150$ MeV und verschwindendem chemischen Potential scheinen die Ergebnisse des punktuellen HRG auch viele Observablen der Gittereichrechnungen von QCD zu reproduzieren. Auf der anderen Seite zeigen schon einfache Abschätzungen, dass die Hadronen-Dichten beim "chemischen Freeze-Out" einer Schwerionen-Kollision eher hoch sind, so dass signifikante Abweichungen vom idealen Gas zu erwarten sind und insbesondere auch kurzreichweitige Abstoßungen betrachtet werden müssen.

Die kurzreichweitige und abstoßende Wechselwirkung zwischen Hadronen wird in dieser Arbeit durch Eigenvolumen-Korrekturen modelliert. Diese Erweiterung des HRG-Modells fand auch vorher schon eingeschränkt Anwendung in der Literatur. Im Rahmen dieser Arbeit findet dagegen eine systematische Untersuchung von Effekten bedingt durch Eigenvolumen statt, wobei insbesondere auf thermische Fits für Hadronen-Multiplizitäten eingegangen wird.

In Kapitel 2 wird die Formulierung unterschiedlicher HRG-Modelle mit Eigenvolumen-Korrekturen vorgestellt. Hierbei wird der Einfluss gleichzeitiger Eigenvolumen-Effekte sowie das exponentielle Hagedorn-Spektrum im Rahmen von HRG untersucht. Beide Erweiterungen führen bei hinreichend großen Temperaturen zu einer deutlich veränderten HRG-Thermodynamik. Ein Vergleich mit QCD-Gittereichrechnungen lässt vermuten, dass weder die Parameter des Eigenvolumens noch das Hagedorn-Massenspektrum eindeutig aus Gitter-Simulationen extrahiert werden können. Der Anstieg thermodynamischer Funktionen bedingt durch Hagedorn-Zustände kann über die unterdrückte Wechselwirkung der Eingenvolumen-Effekte kompensiert werden.

Bisher ist über die überraschend starke Abhängigkeit thermischer Fits für

Hadronen-Multiplizitäten vom Eigenvolumen wenig bekannt und diesem Sachverhalt widmet sich Kapitel 3. Abhängig vom angewandten Ansatz für das Eigenvolumen können aus thermischen Fits sehr unterschiedliche Werte für die chemische "Freeze-Out"-Temperatur und das baryochemische Potential extrahiert werden. Folglich stellt dies die Robustheit bzw. Gültigkeit der extrahierten Größ en in Frage. Gleichzeitig sind die extrahierten Werte für das Verhältnis der Entropie per Baryon $S/A$ robust bezüglich der vorher beschriebenen systematischen Unsicherheit des HRG-Modells und somit unabhängig von exakten Details der Modellierung des Eigenvolumens.

In Kapitel 4 wird ein Monte-Carlo-Zugang zur Beschreibung von EV-Wechselwirkungen in einem multi-komponentigen Gas beschrieben. Dieser erlaubt es zum ersten Mal die gleichzeitige Behandlung von exakter Ladungserhaltung und von EV-Wechselwirkungen im Rahmen des HRG-Modells. Auch die Relevanz dieser Effekte für die Hadronen-Produktion in $p + p$-Kollisionen wird diskutiert.

## Kritische Schwankungen in der klassischen van-der-Waals-Gleichung

Die klassische VDW-Gleichung enthält sowohl eine kurzreichweitige abstoßende sowie eine anziehende Wechselwirkung auf mittleren Abstandsskalen. Es ist dabei das einfachste Modell, welches einen Phasenübergang erster Ordnung sowie den kritischen Punkt vorhersagt. Die Anwendung dieser Gleichung für Hadronenphysik erfordert eine Verallgemeinerung, dabei präsentiert die hier vorliegende Arbeit eine groß kanonische Formulierung der klassischen VDW-Gleichung. Bemerkenswert ist, dass dieser einfache Aspekt der VDW-Gleichung vorher noch nicht publiziert wurde.

Die Formulierung im Rahmen des großkanonischen Ensembles (GCE) eröffnet die Möglichkeit für neue physikalische Anwendungen wie sie durch Fluktuationen der Teilchenzahl gegeben sind. Im kanonischen Ensemble, für welches die VDW-Gleichung anfänglich formuliert wurde, sind solche Fluktuationen per Definition nicht vorhanden. Im GCE sind Teilchenzahlen nur im Mittel erhalten und zeigen ein kritisches Verhalten in der Nähe des kritischen Punktes (CP). Dabei wer-

den kritische Fluktuationen als vielversprechende Observablen für den kritischen Punkt der QCD im Rahmen von Schwerionen-Kollisionen angesehen.

Die großkanonische Formulierung erlaubt es sogar eine analytische Struktur von kritischen Fluktuationen zu erhalten, was in Kapitel 5 diskutiert wird. Es werden volumenunabhängige Verhältnisse für die Kumulanten berechnet, dazu zählen die skalierte Varianz, Skewness und Kurtosis der Teilchenzahl-Fluktuation. Diese Größen zeigen ausgeprägte Strukturen nahe am kritischen Punkt. Dabei sind die Ergebnisse für jede klassische VDW-Flüssigkeit universal und sind qualitativ konsistent mit numerischen Ergebnissen diverser effektiver Theorien der QCD, die einen kritischen Punkt enthalten.

## Quantenstatistische van-der-Waals-Fluid

In Kapitel 6 wird zuerst die Verallgemeinerung der VDW-Gleichung zur Einbeziehung der Quantenstatistik (Bose- und Fermi-Statistik) vorgestellt. Die resultierende VDW-Gleichung erfüllt grundlegende Konsistenz-Anforderungen, dabei vereinfacht sie sich zur klassischen VDW-Gleichung, wenn die Quanteneffekte vernachlässigbar sind. Des Weiteren wird die Form einer idealen Quanten-Gas-Gleichung im nicht-wechselwirkenden Limes angenommen und das dritte Gesetz der Thermodynamik eingehalten. Unserer Kenntnis nach wurde diese relativ einfache quantenstatistische Erweiterung der VDW-Gleichung vorher noch nicht betrachtet.

Im Folgenden wird die Fermi-Dirac-Version der VDW-Gleichung zur Beschreibung von grundlegenden Eigenschaften symmetrischer Kernmaterie angewandt. Die VDW-Parameter $a$ und $b$ werden durch die Reproduktion des bekannten Grundzustandes der Kernmaterie festgelegt. Hierbei ergeben sich die Werte $a \cong 329$ MeV fm$^3$ und $b \cong 3.42$ fm$^3$. Das resultierende Modell enthält den Flüssig-Gas-Phasenübergang für Kernmaterie. Folgende kritische Parameter sind Vorhersagen des Modells: die kritische Temperatur beträgt $T_c \cong 19.7$ MeV und die kritische Dichte nimmt den Wert $n_c \cong 0.07$ fm$^{-3} \cong 0.4\, n_0$ an, was dem halben Wert der normalen Kernmaterie entspricht. Diese Werte liegen dabei nahe an experimentellen Schätzungen. Weitere Verbesserungen der Beschreibung können durch aufwendigere VDW-ähnliche Modelle erreicht werden. Die Möglichkeit

dazu wird ebenfalls in der vorliegenden Arbeit präsentiert.

Die quantenstatistische Verallgemeinerung der VDW-Gleichung ist in der vorliegenden Arbeit allgemein formuliert, also auf jedes Fluid anwendbar und ist insbesondere nicht nur auf QCD beschränkt, was ihre Anwendung im Bereich der Chemie sowie Industrie erlaubt.

## Von der Kernmaterie zur QCD-Gittereichrechnung

Innerhalb des entwickelten quantenstatistischen VDW-Formalismus für Spin-1/2 Nukleonen ist es möglich weitere Baryon-Baryon-Wechselwirkungen ins HRG-Modell aufzunehmen. Diese Studien werden in Kapitel 7 präsentiert. Wir berücksichtigen dabei die VDW-Wechselwirkungen für alle Baryon- sowie Anti-Baryon-Paare. Gleichzeitig werden VDW-Wechselwirkungen zwischen allen anderen Hadronen-Paaren vernachlässigt. Die VDW-Parameter der Baryon-Baryon-Wechselwirkung werden für alle Paare als identisch angenommen und durch den Grundzustand der Kernmaterie ($a \simeq 329$ MeV fm$^3$ und $b \simeq 3.42$ fm$^3$) festgelegt. Somit beschreibt das VDW-HRG-Modell, im Vergleich zum idealen HRG, grundlegende Eigenschaften der Kernmaterie.

Die Vorhersagen dieses Modells werden mit QCD-Gittereichrechnungen bei verschwindendem chemischen Potential verglichen. Die Einbeziehung der VDW-Wechselwirkungen zwischen Baryonen zerstört nicht die schon vorhandene Übereinstimmung des idealen HRG-Modells mit Gittereichrechnungen in Bezug auf Druck und Energiedichten. Es ergibt sich aber eine verbesserte Beschreibung der Schalgeschwindigkeit. Des Weiteren führt die VDW-Wechselwirkungen zu einem qualitativ unterschiedlichen Verhalten der Fluktuationen, die sich in veränderten Kumulanten von Erhaltungsgrößen äußern. Insbesondere sagt das VDW-HRG-Modell analog zu Gittereichrechnungen den Abfall für das Verhältnis $\chi_4^B/\chi_2^B$ von Suszeptibilitäten bzw. Kumulanten der Netto-Baryonen-Zahl im Crossover-Bereich voraus.

Diese Ergebnisse weisen daraufhin, dass sich die Hadronen nicht so schnell mit steigender Temperatur auflösen, wie man es von weitverbreiteten Analysen anhand des idealen HRG-Modells erwarten würde. Die Berechnungen innerhalb des VDW-HRG-Modells bei endlichem chemischen Potential deuten an, dass sich

der nukleare Flüssig-Gas-Phasenübergang bei Schwerionen-Kollisionen in nicht trivialen Fluktuationen der Netto-Baryonen-Zahl äußert. Das Vorhandensein von abstoßenden Baryon-Baryon-Wechselwirkungen wird auch durch vorläufige QCD-Gittereichrechnungen bei imaginärem chemischen Potential bestärkt.

In Kapitel 8 wird die multi-komponentige und quantenstatistische van-der-Waals-Gleichung eingeführt. Dieses Modell erlaubt es beliebige anziehende und abstoßende VDW-Parameter für beliebige Paare von Spezien in multi-komponentigen Systemen festzulegen. Hier wird untersucht welche Effekte von Flavor-abhängigen baryonischen VDW-Wechselwirkungen im Rahmen des HRG-Modells auftreten und welchen Einfluss diese auf Observablen der Gittereichtheorie haben.

## "Pure-Glue" Szenario

Im abschließenden Teil (Kapitel 9) der Thesis wird das reine Glue-Anfangsszenario in hochenergetischer Hadronphysik bzw. Schwerionen-Kollisionen untersucht. Dabei wird angenommen, dass eine heiße Gluo-nenflüssigkeit im Anfangsstadium der Kollision vorliegt, welche keine Quarks und Anti-Quarks enthält. Gemäß den QCD-Gittereichrechnungen sollte eine rein gluonische Materie einen Phasenübergang erster Ordnung bei der kritischen Temperatur von $T_c \simeq 270$ MeV aufweisen. In einem realistischeren Szenario sollte man berücksichtigen, dass Quarks schon kurz vorher und während des Phasenüberganges erster Ordnung erzeugt werden. Technisch kann dies model-liert werden, indem eine zeitabhängige effektive Zahl von Quarkfreiheitsgraden eingeführt wird und solch ein Szenario wird auch in dieser Arbeit angewandt, um Signaturen eines rein gluonischen Anfangszustandes zu untersuchen.

Die hydrodynamische Simulation dieser Arbeit zeigt, dass etwa 25% der to-talen finalen Entropie während der hydrodynamischen Expansion des chemischen Nichtgleichgewichts-Zustandes anfänglicher Gluonen erzeugt wird. Berechnungen von Photonen- und Dilepton-Spektren zeigen, dass die vorhandene Übereinstim-mung von Modellen mit experimentellen Daten am LHC im rein gluonischen Szenario nicht beeinträchtigt wird.

In der Tat wird der Effekt einer anfänglich rein durch Gluonen dominierten

Dynamik in den meisten Observablen fast vollständig ausgewaschen, bedingt durch die lange Zeitspanne während der Quark-Produktion. Weitergehende hydrodynamische Berechnungen weisen daraufhin, dass Kollisionen kleinerer Kerne bei niedrigen Kollisionsenergien, die am relativistischen Schwerionen-Collider von BNL verfügbar sind, vielversprechend auf der Spurensuche eines Gluonen-dominierten Phasenübergangs sein könnten.

# Contents

# Chapter 1

# Introduction

Relativistic collisions of heavy-ions create excited states of strongly interacting matter, which follows a complex dynamical evolution process. This field is dedicated to the study of the properties of the quantum chromodynamics (QCD) – the widely accepted theory of strong interactions, including the equilibrium properties of the equation of state, as well as the non-equilibrium features which are realized in the high-energy heavy-ion collision (HIC) experiments (see [1, 2, 3, 4, 5, 6] for reviews). The QCD is a non-Abelian gauge theory, its underlying symmetry group is SU(3), with the associated color charge. The fundamental particles are quarks and gluons. The non-Abelian nature of QCD leads to several peculiar features, the two most well-known ones are color confinement and asymptotic freedom.

Color confinement reflects our empirical experience that one never observes any free quark or free gluon. Instead, these constituents of QCD are always confined inside of hadrons. Hadrons are color neutral objects, most commonly described as consisting of three constituent quarks (baryons), or a quark-antiquark pair (mesons), although a quantum field theoretical treatment predicts that hadrons contain also an unlimited number of hard and soft gluons and sea quark pairs. The best example for a hadron are protons, $p$, and neutrons, $n$, – the building blocks of atomic nuclei. Due to color confinement, matter at moderate temperatures and densities can to a good approximation be effectively described as composed of $p$, $n$ and other hadrons.

Asymptotic freedom is a property of QCD which causes the coupling be-

tween its fundamental constituents to become asymptotically weak at high energies/small distances [7, 8]. Consequently, at extremely high temperatures and densities one expects to find a weakly coupled, quasi-free state of quarks and gluons dubbed quark-gluon plasma (QGP) – this state would correspond to a system of many interacting quarks and gluons which are no longer confined to the interior of one hadron.

The first principles theory of QCD is well-defined, but direct applications of this theory to experiment are quite limited due to significant technical obstacles. In fact the more general features of QCD remain unclear to date. In particular, the nature of the transformation of hadrons into quarks and gluons, and also the inverse process, hadronization of colored objects into hadrons, remains an open issue. Perturbative techniques, very successful in quantum electrodynamics, break down in QCD at moderate energies due to the dramatic growth of the coupling strength (the effective coupling constant $\alpha_s$ can become $\alpha_s > 1$ instead of $\alpha_s \ll 1$ [9, 10]). Thus, perturbative methods are inapplicable for describing the hadron-parton transformation. Nowadays, the best established first-principle tool available is lattice QCD – a direct numerical solution of QCD discretized on a finite space-time lattice. It allows a good representation of the low-lying hadron spectrum but for thermal QCD, technical limitations (sign doubling) confine lattice QCD simulations to the $\mu_B \cong 0$ (zero net-baryon density) region of the QCD phase diagram. Improved lattice techniques for hot QCD are rapidly developing and finite $\mu_B$ results may appear soon. In general, the phase diagram of the strongly interacting matter is expected to contain a rich structure at finite baryon density and at moderate temperatures. Sketch of the QCD phase diagram [11], containing many possible phases of QCD matter, is depicted in Fig. 1.1.

Lattice QCD simulations show that the thermal hadron-parton transition at zero net-baryon density, $\mu_B = 0$, is not a first or second order phase transition, but a smooth *crossover* – a continuous change of thermodynamic variables over a sizable temperature region, $T \sim 150 - 200$ MeV [9]. Presently, these simulations do not provide an answer about the nature of the hadron-parton transition at finite $\mu_B$. It is conjectured that this transition turns first-order somewhere in the finite net-baryon density region. Significant theoretical and experimental effort to locate or to disprove the associated critical point of QCD is currently in progress.
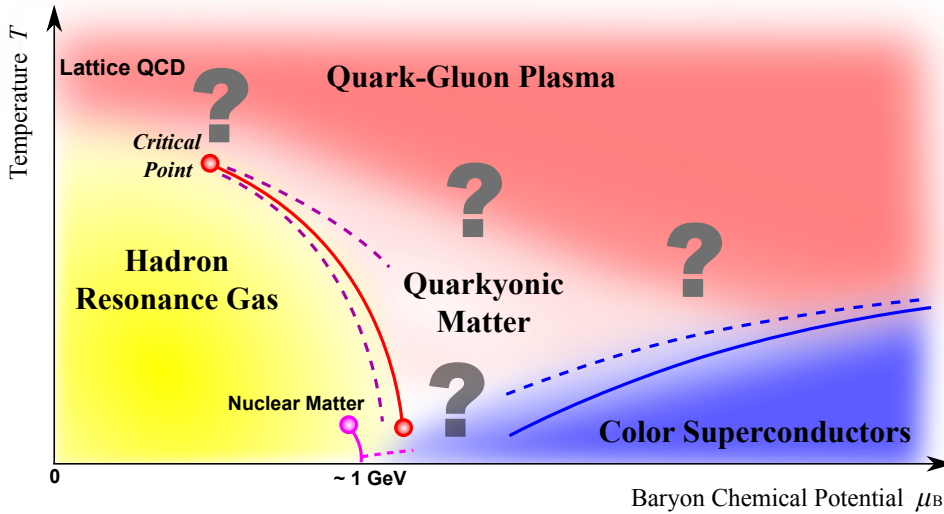
Figure 1.1: Schematic view of the conjectured QCD phase diagram, showing different possible phases of strongly interacting matter. This is the adapted version of the figure taken from Ref. [11].

While lattice field theoretical simulations provide QCD equation of state at $\mu_B = 0$ [12, 13], they do not give a direct answer as to which are the dominant degrees of freedom at a particular temperature and baryochemical potential. Hence it impossible to fix a sharp deconfinement temperature, $T_D$, above which partons become dominant degrees of freedom. A phenomenological input is needed. We study here a popular model for the confined phase of QCD, namely the hadron resonance gas (HRG) model, an equilibrated system of known hadrons and resonances. The HRG model in its simplest version is a gas of non-interacting hadrons and resonances. The HRG provides a reasonable description of lattice QCD data available at temperatures up to 150 MeV. Unlike lattice QCD, the HRG is easily extended to smaller temperatures and to finite $\mu_B$. The HRG has been remarkably successful to fit data on hadron production in HIC experiments (see, e.g., Refs. [14, 15, 16, 17] for reviews). Deviations from the ideal HRG (and from other, more sophisticated hadronic models) of lattice data at high temperatures have been interpreted as signatures of deconfinement.

However, modeling strongly interacting matter with a HRG-type ansatz needs detailed specifications of the input to be used, e.g. which particles to include, how to treat finite resonance widths, etc. Particular attention must be paid to

the poorly constrained phenomenological theory of hadron-hadron interactions. This thesis aims to study the sensitivity of the HRG model predictions, both for lattice and HIC observables, with regard to these uncertainties.

Hadronic interactions in thermal and chemical equilibrium in this thesis are based on the famous *van der Waals* (VDW) equation. While this is certainly not the most conventional choice for nuclear/hadronic physics applications, the simplicity of the VDW approach makes it extremely useful. The VDW framework allows to optionally include the two most basic ingredients of hadron-hadron interaction: the short-range repulsion, modeled by excluded-volume (EV) corrections, and the intermediate range attractions. Thus, the VDW model provides a reasonable description of the nuclear matter region of the QCD phase diagram (see Fig. 1.1). This is in contrast to the standard HRG model, where the nuclear matter features are missing completely. The VDW model, containing a first-order phase transition with a critical point (CP), is therefore also a useful tool for the ongoing search of the CP of QCD with fluctuation measurements: the model provides simple analytic predictions for the fluctuation patterns typical for a CP. It is quite remarkable, but it appears that the simple VDW equation was never properly used in the context of QCD, despite these many evident possibilities. We will present and discuss in this thesis also several extensions of the classical VDW model which are performed here for the first time. These include the grand canonical ensemble formulation of the classical VDW equation, the inclusion of quantum (Bose-Einstein and Fermi-Dirac) statistics in the VDW model, and thermodynamically consistent relativistic extensions to the multi-component systems with fluctuating numbers of particles. These are textbook level theory extensions, which for reasons unknown to us have never been published before, in spite of the great phenomenological usefulness of the VDW model.

Finally, it should be mentioned that HIC involve highly dynamical complex processes. The statistical description of hadron production with HRG, using just a few thermodynamic parameters certainly does not give justice to the enormous complexity of the collision processes. The dynamics of the HIC are usually described by microscopic hadronic/partonic transport models [18, 19, 20, 21, 22, 23, 24], or, especially at higher collision energies, by relativistic hydrodynamics [25, 26, 27, 28, 29]. Despite the success of the hy-

drodynamic model and of the statistical model at the RHIC and LHC energies, it is clear that a state even only close to chemical and/or thermal equilibrium is an extremely simplified scenario for HIC (see [30] for recent discussion).

The ambiguity in the interpretation of the experimental data leaves plenty of room for alternative scenarios. One possibility is that early, undersaturated matter, as created in the early stage of HIC, may, at sufficiently high energies consist initially purely of gluons [31, 32]. This long-standing prediction of the transport theory [23, 33, 34] is due to large gluon production cross sections and to non-equilibrium nature of the HIC process. This scenario is explored in some detail in the present thesis.

## Structure of the thesis

The role of the repulsive EV interactions between hadrons in the HRG model is studied first. In Chapter 2 different EV models of a multi-component hadron gas are described. The importance of EV interactions is illustrated by their strong influence on the most basic observables from lattice QCD.

Chapter 3 explores the sensitivity of thermal fits to hadron yields measured in different heavy-ion collision experiments to the modeling of the EV interactions in HRG model. Previous studies regarding this systematic uncertainty of the HRG model were limited to a particular case of constant eigenvolume for all hadron species. They are extended here to the species dependent eigenvolumes. Consequences of such scenario for the determination of chemical freeze-out parameters from thermal fits are described in detail.

In Chapter 4 the Monte Carlo approach to treat EV interactions in multi-component gas of particles is presented. It allows to study finite system size effects. These effects appear when an eigenvolume of a single particle is not completely negligible compared to the total system volume, and they cannot be described with commonly used analytic models since they all assume thermodynamic limit $V \to \infty$. The Monte Carlo formulation also allows to study for the first time the simultaneous effects of exact charge conservation and EV interactions in HRG model. Relevance of these effects for description of the hadron production in $p + p$ collisions is illustrated.

Subsequent parts of the work deal with the full VDW equation, with both attractive and repulsive interactions. The grand canonical ensemble formulation of the classical VDW equation is presented in Chapter 5. It is then used to study analytically the structure of the critical fluctuations of particle number in a system which contains a first-order phase transition with a CP. The VDW equation is also used to verify the presence of the critical behavior in the so-called strongly intensive quantities, which are presently being used in heavy-ion collision experiments as potential probes of the CP of QCD.

Chapter 6 introduces a quantum statistical extension of the VDW theory for a single-component fluid. This extension allows to include VDW interactions in the system of fermions or bosons in the phase diagram regions where quantum statistical effects are non-negligible. The formalism is then used to study properties of symmetric nuclear matter in the framework of a fermionic VDW equation for nucleons.

The quantum statistical VDW formalism is then employed to include the essential features of the nuclear matter physics into full HRG in Chapter 7. The VDW interaction terms are introduced into HRG for all baryon pairs, with VDW parameters $a$ and $b$ fixed by the fit to the nuclear ground state. The effects of these interactions on the behavior of second and higher moments of fluctuations of conserved charges in the so-called crossover region $T \sim 140 - 190$ MeV at zero chemical potential are studied in some detail. The model predictions are also confronted to the lattice QCD data.

Chapter 8 presents the multi-component quantum statistical van der Waals equation. This model allows to specify arbitrary attractive and repulsive VDW parameters for any pair of species in the multi-component system. Several applications of the formalism are illustrated: (i) The asymmetric nuclear matter as a two-component Fermi-Dirac VDW system of protons and neutrons; (ii) The EV interactions betweens $\alpha$ particles and nucleons as a mechanism of dissolution of $\alpha$ clusters in the high-density nuclear matter; (iii) Effects of the flavor-dependent baryonic VDW interactions in HRG on lattice QCD observables.

Chapter 9 discusses signatures of the pure glue scenario for the high-energy hadron and heavy-ion collisions. Space-time evolution, entropy production, photon and dilepton emission and other features of the chemically non-equilibrium

QCD matter created in such collisions are described in the framework of ideal hydrodynamics. Optimal experimental conditions for observing new exotic states of matter are discussed.

Summary and concluding remarks follow in the final Chapter 10.

# Chapter 2

# Excluded-volume interactions in hadron resonance gas

## 2.1 Ideal hadron resonance gas model

Thermodynamic models of description of properties of the strongly interacting matter are valuable tools in modern high-energy nuclear physics. The conventional ideal (point-particle) HRG model and its modifications have been used to extract thermodynamic parameters of matter created in heavy-ion collisions. Rich experimental data on mean hadron multiplicities in various experiments ranging from low energies at SchwerIonen-Synchrotron (SIS) to highest energy of the Large Hadron Collider (LHC) [15, 35, 36, 37, 38, 39, 40] exist and have been fitted for a long time. At temperatures between $T \sim 100 - 150$ MeV and at zero chemical potential, the point-particle HRG also appears to reproduce many lattice QCD observables [41, 42, 43, 44].

In the simplest setup, the conjectured hadronic phase is described by a multi-component, ideal gas of point-like hadrons – the ideal HRG model. In the grand canonical ensemble (GCE) formulation of the ideal HRG there are no correlations between different hadronic components. Thus, the pressure is given by

$$p_{\text{HRG}}^{\text{id}}(T, \mu) = \sum_i p_i^{\text{id}}(T, \mu_i),\qquad(2.1)$$

where the sum goes over all hadron species included in the model, $p_i^{\text{id}}(T, \mu_i)$ is

the pressure of the ideal Fermi or Bose gas at the corresponding temperature and chemical potential for species $i$:

$$p_i^{\text{id}}(T, \mu_i) = \frac{d_i}{6\pi^2} \int_0^\infty \frac{k^4 dk}{\sqrt{k^2 + m_i^2}} \left[ \exp\left( \frac{\sqrt{k^2 + m_i^2} - \mu_i}{T} \right) + \eta_i \right]^{-1}, \qquad (2.2)$$

where $d_i$ and $m_i$ are, respectively, the spin degeneracy factor and mass of hadron species $i$, and where $\eta_i$ equals +1 for fermions, -1 for bosons, and 0 for Boltzmann approximation.

Other thermodynamic quantities are also given in form similar to (2.1): a sum over the corresponding ideal gas quantities for all hadron species. The particle density of hadron species $i$ is $n_i^{\text{id}}(T, \mu_i)$, i.e. it is simply given by the ideal gas relation for species $i$:

$$n_i^{\text{id}}(T, \mu_i) = \frac{d_i}{2\pi^2} \int_0^\infty k^2 dk \left[ \exp\left( \frac{\sqrt{k^2 + m_i^2} - \mu_i}{T} \right) + \eta_i \right]^{-1}. \qquad (2.3)$$

Only light unflavored and strange hadrons are considered throughout this work in HRG. Within the GCE formulation, all conserved charges, such as baryonic number $B$, electric charge $Q$, and net strangeness $S$, are conserved on average. Therefore, there are three corresponding independent chemical potentials: $\mu_B$, $\mu_Q$, and $\mu_S$. The chemical potential of the $i$th hadron species is thus determined as

$$\mu_i = B_i \mu_B + S_i \mu_S + Q_i \mu_Q \qquad (2.4)$$

with $B_i = 0, \pm1$, $S_i = 0, \pm1, \pm2, \pm3$, and $Q_i = 0, \pm1, \pm2$ being the corresponding conserved charges of $i$th hadron: baryon number, strangeness, and electric charge. The notation $\mu$ will be used to denote all chemical potentials, $\mu \equiv (\mu_B, \mu_S, \mu_Q)$.

The finite width $\Gamma_i$ of resonance $i$ is taken into account by additional integration of the ideal gas functions over the mass distribution $f_i(m)$, i.e.

$$p_i^{\text{id}}(T, \mu_i) \Rightarrow \int dm \, f_i(m) \, p_i^{\text{id}}(T, \mu_i), \qquad (2.5)$$

$$n_i^{\text{id}}(T, \mu_i) \Rightarrow \int dm \, f_i(m) \, n_i^{\text{id}}(T, \mu_i), \qquad (2.6)$$

and so on. For the stable hadrons, $f_i(m) = \delta(m - m_i)$, where $\delta$ is the Dirac delta function. The same is also true for resonances whenever the zero-width approximation is applied.

The above formulation, a multi-component point-particle gas of all known hadrons and resonances, is presently the most commonly used realization applied to the thermal model analysis. In phenomenologically more "realistic" HRG model realizations one may take into account both the attractive and the repulsive interactions between hadrons. It has been argued [45], that the inclusion of all known resonances into the model as free non-interacting (point-like) particles (i.e. into the sum in Eq. (2.1)), may allow for an effective modeling of the attractive interactions between hadrons, including the formation of narrow resonances and of Hagedorn states. On the other hand, simple estimates show that hadron densities at the so-called "chemical freeze-out" stage of heavy-ion collision reactions are rather large. Therefore, we expect significant deviations from the ideal gas picture. Particularly, the short-range repulsive interactions need to be considered.

## 2.2 Excluded-volume models

The repulsive interactions between hadrons can be modeled by the eigenvolume correction of the van der Waals type, whereby the volume available for hadrons to be created and move in is reduced by the sum of all their eigenvolumes. Such a correction was first studied in the hadronic equation of state in Refs. [46, 47, 48, 49]. A thermodynamically consistent procedure for a single-component gas was first formulated in Ref. [50]. Hadrons may also have different eigenvolumes – this option is considered in the present work. Then, a multi-component eigenvolume HRG model is necessary.

### 2.2.1 Single-component van der Waals eigenvolume model

The simplest eigenvolume model is the classical VDW eigenvolume model. The excluded volume procedure in the VDW model corresponds to a substitution of

the system volume $V$ by the available volume $V_{av}$, i.e.

$$V \rightarrow V_{\mathrm{av}} = V - vN, \tag{2.7}$$

where $v = 4 \cdot (4\pi r^3/3)$ is the excluded volume parameter with $r$ being the corresponding hard sphere radius of particle $i$. This result, in particular, the presence of a factor of 4 in the expression for $v$, can be rigorously obtained for a low density gas of particles with hard sphere interaction potential (see, e.g., Ref. [51]). The classical VDW equation gives the pressure in the canonical ensemble. Neglecting the attraction term one has

$$P(T, V, N) = \frac{T\,N}{V - v\,N}. \tag{2.8}$$

In the GCE, the substitution (2.7) leads to a transcendental equation for the pressure [50]:

$$p(T, \mu) = p^{\mathrm{id}}(T, \mu - v\,p), \tag{2.9}$$

where $p^{\mathrm{id}}$ is the ideal gas pressure. The pressure $p(T, \mu)$ is obtained by solving the Eq. (2.9) numerically for given $T$ and $\mu$. The particle density $n(T, \mu) = (\partial p/\partial \mu)_T$ is

$$n(T, \mu) = \frac{n^{\mathrm{id}}(T, \mu^*)}{1 + v\,n^{\mathrm{id}}(T, \mu^*)}, \qquad \mu^* = \mu - b\,p(T, \mu), \tag{2.10}$$

where $n^{\mathrm{id}}$ is the ideal gas density.

## 2.2.2  "Diagonal" eigenvolume model

The single-component eigenvolume model of Ref. [50] was generalized to the multi-component case in Ref. [52]. It was assumed that the available volume of each of the hadron species is the same, and equals to the total volume minus the sum of the eigenvolumes of all hadrons in the system. Let us assume that we have $f$ different hadron species. The pressure as function of the temperature

and of hadron densities has the following form in the Boltzmann approximation:

$$p(T, n_1, \ldots, n_f) = T \sum_i \frac{n_i}{1 - \sum_j v_j n_j}, \qquad (2.11)$$

where the sum goes over all hadrons and resonances included in the model, and where $v_i$ is the eigenvolume parameter of hadron species $i$. The eigenvolume parameter $v_i$ can be identified with the 2nd virial coefficient of the single-component gas of hard spheres and is connected to the effective hard-core hadron radius as $v_i = 4 \cdot 4\pi r_i^3/3$. In the grand canonical ensemble (GCE) one has to solve the non-linear equation for the pressure, which reads

$$p(T, \mu) = \sum_i p_i^{\mathrm{id}}(T, \mu_i^*), \qquad (2.12)$$

where $p_i^{\mathrm{id}}(T, \mu_i^*)$ is the pressure of the ideal (point-like) gas at the corresponding temperature and chemical potential, and $\mu_i^* = \mu_i - v_i\, p(T, \mu)$ is the "shifted" chemical potential due to the eigenvolume interactions. The $v_i$ are the eigenvolume parameters of the distinct hadron species $i$. The number density of these species can be calculated as

$$n_i(T, \mu) = \frac{n_i^{\mathrm{id}}(T, \mu_i^*)}{1 + \sum_j v_j n_j^{\mathrm{id}}(T, \mu_j^*)}. \qquad (2.13)$$

The multi-component eigenvolume HRG model given by Eqs. (2.11)-(2.13) is the most commonly used EV-parametrization in the thermal model analysis. Since this model does not consider the important cross-terms in the virial expansion of the multi-component gas of hard spheres (see details below) we will refer to it in the present work as the "Diagonal" model. Quantum statistical effects are taken into account in this model if corresponding functions of ideal quantum gas are used in Eqs. (2.12) and (2.13). In this case dependence of pressure on temperature and densities has a more complicated form than given by Eq. (2.11).

### 2.2.3 "Crossterms" eigenvolume model

The virial expansion of the classical (Boltzmann) multi-component gas of hard spheres up to 2nd order can consistently be written as [51]

$$p(T, n_1, \ldots, n_f) = T \sum_i n_i + T \sum_{ij} b_{ij} n_i n_j + \ldots, \qquad (2.14)$$

where

$$b_{ij} = \frac{2\pi}{3} (r_i + r_j)^3 \qquad (2.15)$$

are the components of the symmetric matrix of the 2nd virial coefficients.

Comparing Eqs. (2.11) and (2.14) one can see that the "Diagonal" model is not consistent with the virial expansion of the multi-component gas of hard spheres up to 2nd order. It rather corresponds to a different matrix of 2nd virial coefficients, namely $b_{ij} = v_i$. While we do not require hadrons to be non-deformable spherical objects and expect the "Diagonal" model to capture the essential features of a system of particles with different sizes, the interpretation of $r_i$ as a hard-core hadron radius can be problematic in such model.

Therefore, we additionally consider the van der Waals-like multi-component eigenvolume model of Ref. [53], which is formulated in the grand canonical ensemble (GCE) assuming Boltzmann statistics, and which is consistent with the 2nd order virial expansion in Eq. (2.14). The pressure in this model reads

$$p(T, n_1, \ldots, n_f) = \sum_i p_i = T \sum_i \frac{n_i}{1 - \sum_j \widetilde{b}_{ji} n_j}, \qquad (2.16)$$

where $\widetilde{b}_{ij}$ is

$$\widetilde{b}_{ij} = \frac{2 \, b_{ii} \, b_{ij}}{b_{ii} + b_{jj}} \qquad (2.17)$$

while the $b_{ij}$ are given by (2.15). Here the quantities $p_i$ can be regarded as "partial" pressures. This eigenvolume model given by (2.16) is initially formulated in the canonical ensemble. In Ref. [53] it was transformed to the grand canoni-

cal ensemble. In the GCE formulation one has to solve the following system of non-linear equations for $p_i$:

$$p_i = p_i^{\text{id}} \left( T, \mu_i - \sum_j \widetilde{b}_{ij} \, p_j \right), \qquad i = 1, \ldots, f, \qquad (2.18)$$

where $f$ is the total number of the hadronic components in the model. Hadronic densities $n_i$ can then be recovered by solving the system of linear equations connecting $n_i$ and $p_i$:

$$T n_i + p_i \sum_j \widetilde{b}_{ji} n_j = p_i, \qquad i = 1, \ldots, f \ . \qquad (2.19)$$

We refer to this model, as given by Eqs. (2.16)-(2.19), as the "Crossterms" eigenvolume model. From technical point of view, the "Crossterms" model is more difficult to solve than the "Diagonal" model: a set of coupled non-linear equations (2.18) needs to be solved, instead of a single equation (2.12) for the total pressure in the "Diagonal" model. In practice, the solution to (2.18) can be obtained by using an appropriate iterative procedure. In the present calculations, Broyden's method [54] is employed to obtain the solution of the "Crossterms" model, using the corresponding solution of the "Diagonal" model as the initial guess.

The coefficients $\widetilde{b}_{ij}$ may also be specified differently from Eq. (2.17). This allows then to model the repulsive interactions between different hadron pairs in each own specific way. In the specific case of $\widetilde{b}_{ij} \equiv v_i$ the "Crossterms" EV model reduces to the "Diagonal" EV model.

The eigenvolume models described above are implemented as a C++ package, which is provisionally named CuteHRG [55]. All HRG-related calculations presented in this work are obtained within CuteHRG.

## 2.3 Comparison with lattice QCD

The role of the excluded-volume effects in a hadron gas can be studied in the context of the lattice QCD results for the QCD equation of state at zero chem-

ical potential. In particular, we consider the lattice QCD data for pressure and energy density at zero baryonic chemical potential, as obtained by the Wuppertal-Budapest collaboration for the (2+1)-flavor QCD [12]. Two rather different strategies are employed.

In our first analysis [56], only small temperatures, $T < 160$ MeV, below the crossover-type transition, are considered. The hadron list contains all strange and non-strange hadrons listed in the Particle Data Tables [57], which have an established (three or more stars) status there.

Optionally, the hadron list is supplemented by an exponentially increasing Hagedorn mass spectrum. For this Hagedorn mass spectrum the parameterization $\rho(m) = C\,\theta(m-M_0)\,(m^2+M_0^2)^{-a}\,\exp(m/T_H)$ with $M_0 = 2$ GeV, $T_H = 160$ MeV, $m_0 = 0.5$ GeV, and $a = 5/4$ is employed. Normalization parameter $C$ can be fixed by fitting lattice data. For simplicity, in the present analysis it is assumed that all hadrons, including the Hagedorn states, have identical eigenvolumes, characterized by a single hard-core radius parameter $r$. In this particular case, the "Diagonal" and the "Crossterms" EV models are then identical.

Results of the calculations for the temperature dependence of both the scaled pressure and energy density, for different values of $r$, are depicted in Fig. 2.1. The excluded-volume corrections decrease both the pressure and the energy density while the inclusion of the Hagedorn mass spectrum leads to their enhancement. If the EV corrections and the Hagedorn mass spectrum are considered simultaneously, we find that the lattice data can be well fitted for $r \lesssim 0.4$ fm and $C \lesssim 0.2$ GeV$^{3/2}$ with $\chi^2/N_{\rm dof} \lesssim 1$ for $T < 160$ MeV. These results indicate that neither the EV parameters neither nor the Hagedorn mass spectrum can be extracted in a definitive way from the lattice data.

It should be noted that here a constant eigenvolume was assumed for all hadrons. Since the matter is meson-dominated at $\mu = 0$, the obtained restrictions on the value of $r$ do mainly apply to mesons. It is quite feasible, however, that the EV interactions are different for mesons and baryons (see, e.g., Ref. [58] and also Chapter 7 of the present work).

In the second analysis method, a different strategy is adopted: instead of considering a limited temperature range, we rather analyze how far the HRG alone is able to describe the lattice data for pressure and energy density. The
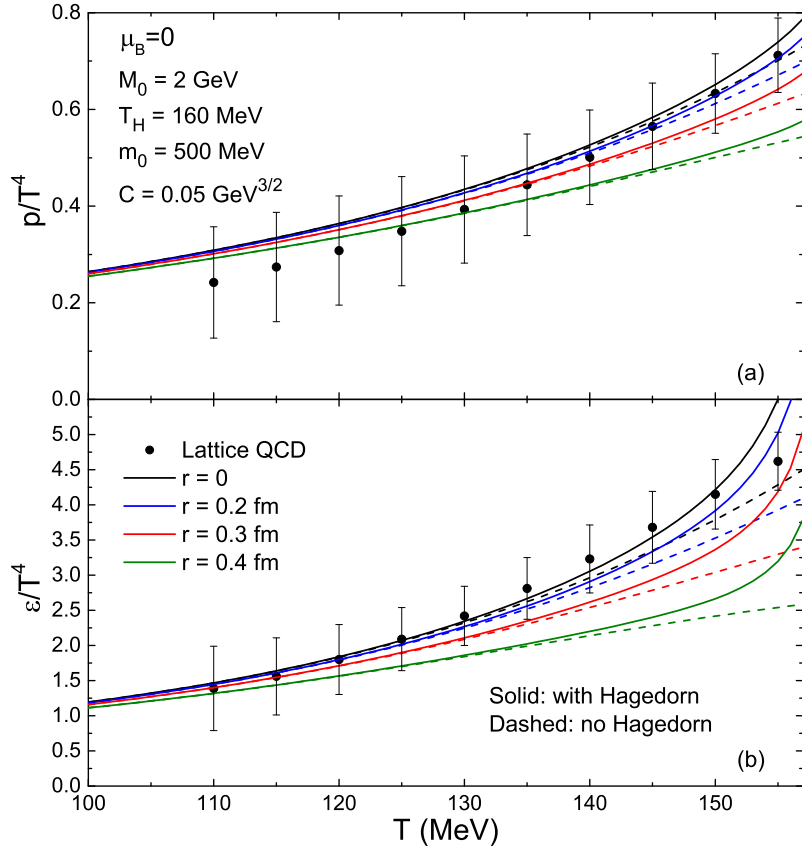
Figure 2.1: Results of the EV-HRG model calculations for (a) $p/T^4$ and (b) $\varepsilon/T^4$ in comparison with the lattice QCD data. Solid lines correspond to calculations with additional Hagedorn spectrum. Dashed lines show calculations only with PDG input. Different line colors correspond to different values of the hadron hard-core radius $r$.

commonly used point-particle HRG can describe these data up to $T \sim 150 - 180$ MeV. At high temperatures, the ideal HRG overshoots significantly the lattice data due to the quickly increasing number of hadronic degrees of freedom. In fact, it shows signs of the Hagedorn divergence. In the present analysis the HRG, with the conventional PDG hadron input, and with mass-proportional eigenvolumes

$$v_i = m_i/\varepsilon_0, \tag{2.20}$$

is used. For this particular calculation the "Diagonal" EV model formulation is used. For simplicity, the Hagedorn states are omitted.

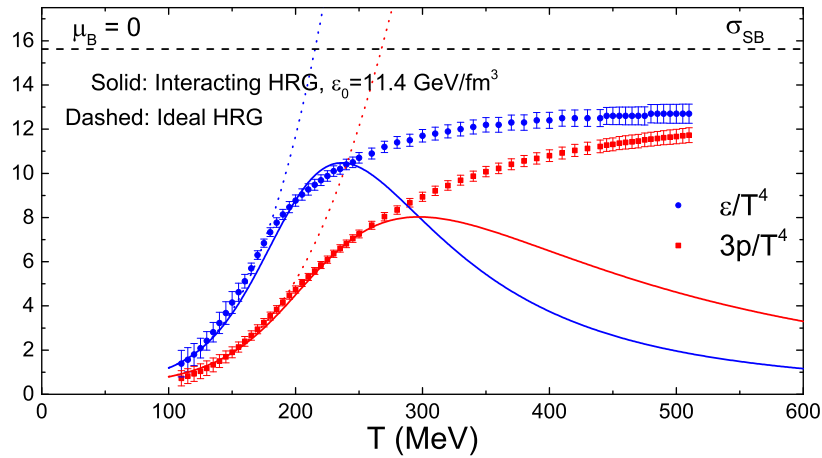Figure 2.2:   Results of the "Diagonal" EV-HRG model calculations for $p/T^4$ and $\varepsilon/T^4$ employing the mass-proportional eigenvolumes in comparison with the lattice QCD data. The value of $\varepsilon_0 \simeq 11.4$ GeV/fm$^3$ is used in Eq. (2.20), which gives a good agreement with lattice data.

Figure 2.2 depicts the temperature dependence of the scaled pressure and energy density for the point-particle HRG and for the EV-HRG with $\varepsilon_0 = 11.4$ GeV/fm$^3$. It is seen that the inclusion of the EV corrections leads to a significant improvement of the agreement between HRG and the lattice QCD: the data are described fairly well by the EV-HRG up to $T = 250$ MeV. This alternative interpretation is that the lattice results may in fact to a large extent be represented by hadrons even above $T = 150$ MeV, which are conventionally totally attributed to deconfined matter. This ambiguous result shows that the interpretation of lattice data remains challenging. It should be stressed that the main purpose of the calculation shown in Fig. 2.2 is to illustrate the importance of the EV effects at higher temperatures/densities, motivating further careful studies of these effects in the various hadron gas models. The results do by no means imply that EV parametrization in Fig. 2.2 is "the right one"!

# Chapter 3

# Thermal fits to heavy-ion hadron yield data

## 3.1 Hadron yield fitting in HRG

The HRG model has been used to reproduce the hadron yields from heavy-ion collisions by fitting the experimental data. Such an approach assumes full thermodynamic equilibrium between all stable hadrons and all resonances at a so-called "chemical freeze-out" moment of all heavy-ion reactions. Contributions from resonance decays to yields of different hadrons can naturally be included in this model. Results presented in this Chapter are based on [59, 60, 61, 62, 63].

Commonly, a GCE formulation of the HRG is used for relativistic central heavy-ion reactions, which is usually justified by the large system size created in such reactions. Within this formulation, all conserved charges, such as baryonic number $B$, electric charge $Q$, and net strangeness $S$, are conserved on average. As mentioned in the previous chapter, the chemical potential of the $i$th hadron species is thus determined as $\mu_i = B_i\mu_B + Q_i\mu_Q + S_i\mu_S$. At each fixed temperature $T$ and baryochemical potential $\mu_B$, the $\mu_Q$ and $\mu_S$ are determined in a unique way in order to satisfy two "initial" conditions: the electric-to-baryon charge ratio of $Q/B = 0.4$, and the vanishing net strangeness $S = 0$. If pre-freezeout radiation is neglected, both of these conditions can be fulfilled for the systems created in collisions of heavy ions. Otherwise, such a pre-freezeout emission of particles will lead to additional uncertainty in the determination of $\mu_B$, $\mu_Q$, and $\mu_S$.

In the simplest setup there are only three fit parameters: the temperature $T$, the baryonic chemical potential $\mu_B$, and the system volume parameter $V$. Of course, realistic modifications such as chemical under- or over-saturation of the light and/or strange quarks introduce additional parameters (see, e.g., Refs. [15, 64]).

As mentioned above, the HRG model provides a rather satisfactory description of hadron production over a wide range of collision energies [15, 40, 65]. The moderate number of fit parameters, as well as the simplicity of the model, let the HRG appear as a very powerful and attractive tool for modeling particle production in heavy-ion collisions. On the other hand, this simple model suffers from significant systematic uncertainties it its formulation. In particular, there is a rather limited knowledge of the properties of heavy hadronic states and their decay branching ratios. These properties serve as an input into the HRG model, thus one has to rely on various assumptions. Also, the short-range repulsive hadronic interactions and its role for the thermal fits is not properly understood. These interactions are normally modeled via the EV corrections. However, the EV parameters cannot be constrained sufficiently by the current knowledge of the hadron-hadron interactions. The role of the EV effects on thermal fits is studied in detail in this work.

Unless stated otherwise, in all present calculations the HRG includes strange and non-strange hadrons as listed in the Particle Data Tables [57], along with their decay branching ratios. This includes mesons up to $f_2(2340)$, (anti)baryons up to $N(2600)$. Those hadrons with charm and bottom quark content, as well as light nuclei are not included in the standard setup. The finite width of the resonances is taken into account by additional integrations over their relativistic Breit-Wigner shapes in the point-particle gas expressions in the $\pm 2\Gamma_i$ interval around the pole mass (see [66, 67]). Here $\Gamma_i$ is the width of the resonance $i$.

The HRG model fits are done by minimizing the value

$$\frac{\chi^2}{N_{\text{dof}}} = \frac{1}{N_{\text{dof}}} \sum_{i=1}^{N} \frac{\left(N_i^{\text{exp}} - N_i^{\text{HRG}}\right)^2}{\sigma_i^2} \, , \tag{3.1}$$

where $N_i^{\text{exp}}$ and $N_i^{\text{HRG}}$ are the experimental and calculated in the HRG hadron

multiplicities, respectively; $N_{\mathrm{dof}}$ is the number of degrees of freedom, that is the number of the data points minus the number of fitting parameters; and $\sigma_i^2 = (\sigma_i^{syst})^2 + (\sigma_i^{stat})^2$ is the sum of the squares of the statistical and systematic experimental errors. The $N_i$ may also represent ratio of two yields in some cases. The MINUIT2 package [68] is employed for the minimization procedure in CuteHRG.

The mean multiplicity $\langle N_i \rangle$ of $i$th particle species is calculated in the HRG model as a sum of the primordial mean multiplicity $\langle N_i^{\mathrm{prim}} \rangle \equiv n_i V$ and resonance decay contributions as follows

$$\langle N_i \rangle \;=\; \langle N_i^{\mathrm{prim}} \rangle \;+\; \sum_R \langle n_i \rangle_R \, \langle N_R^{\mathrm{prim}} \rangle \,, \qquad (3.2)$$

where $\langle n_i \rangle_R$ is the average number of particles of type $i$ resulting from decay of resonance $R$.

It should be stressed that Eq. (3.2) is also valid for calculating yields of unstable particles, such as the $\phi$ meson, $K^*(892)$ resonance, or $\Lambda(1520)$ resonance. This is important since yields of these unstable particles have been measured, and they are used in the thermal fits. These decay contributions are properly taken into account in the CuteHRG package that is used in this work. At the same time, this not the default behavior of the popular THERMUS package [67]. Extra care should be taken to deal with this subtlety properly in THERMUS (see Ref. [59] for details).

## 3.2 Chemical freeze-out line in ideal HRG

The systematics of the chemical freeze-out description in heavy-ion collisions within the ideal HRG appeared to be well established for several years. Early on, it was observed empirically that the hadrochemical composition of the system at chemical freeze-out corresponds in the ideal HRG to an energy per hadron (including hadron rest masses) being approximately 1 GeV per hadron in the rest frame of the produced system [36], independent of the freeze-out $T^{\mathrm{fo}}$-$\mu_B^{\mathrm{fo}}$ values found in fits. This parametrization leads to a chemical freeze-out curve in the $T$-$\mu_B$ plane. The temperature $T^{\mathrm{fo}}$ and the baryon chemical potential $\mu_B^{\mathrm{fo}}$
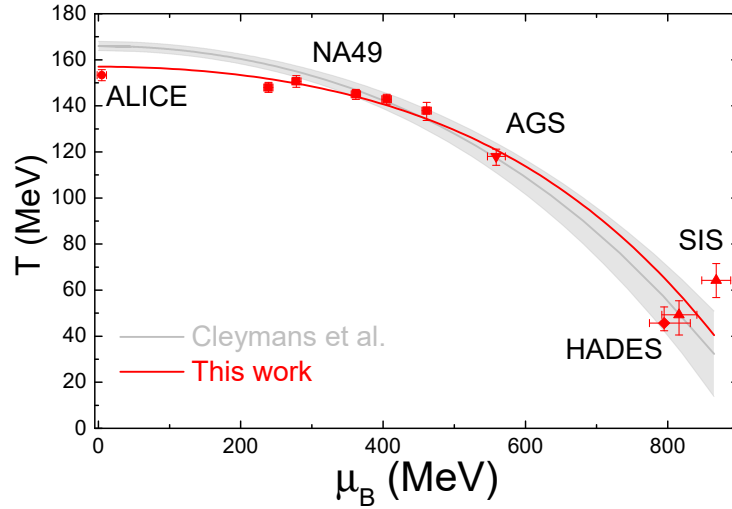
Figure 3.1:   The values of temperature and baryochemical potential on the $T$-$\mu_B$ plane as extracted within ideal HRG by fitting the hadron yields data in central Au+Au and Pb+Pb at SIS, AGS, SPS, and LHC using the CuteHRG package. The grey line shows the chemical freeze-out parametrization from Ref. [69] while the red line shows the updated parametrization obtained in this work (coincides with Ref. [59], see text).

follow a simple analytic dependence as the function of collision energy [69, 70]. Some data, in particular the data measured at the SPS, are not well described in the chemical equilibrium scenario. An improved description has been obtained by introducing chemical non-equilibrium parameters for strangeness [65], and, additionally, for light quarks [15, 71]. Notably, the above findings remain valid also for a particular but widely used choice of an excluded-volume HRG with constant eigenvolume for all hadrons [69]. This is so because EV corrections "cancel out" in all ratios for this special case.

Let us first revisit the analysis of the hadron yield data at SIS, AGS, SPS, and LHC within the ideal HRG model. This is done for two reasons: First, this serves as a cross-check for the CuteHRG package, whether it reproduces the known systematics of chemical freeze-out within ideal HRG. Secondly, the NA49 data analysis for central Pb+Pb collisions was extended [72, 73, 74, 75, 76, 77, 78] in comparison to the results used in previous studies [40, 65]. Recent GSI data of the HADES collaboration for Au+Au collisions at $E_{\text{kin}} = 1.23A$ GeV [79], the Au+Au data for $E_{\text{kin}} = 0.8A$, $1.0A$ GeV, the Au+Au data for $E_{\text{lab}} = 11.6A$ GeV

from BNL Alternating Gradient Synchrotron (AGS) [38, 80, 81, 82, 83, 84], and data from central Pb+Pb data of the ALICE collaboration at the LHC at $\sqrt{s_{\mathrm{NN}}} = 2.76$ TeV [85, 86, 87, 88] are also added to the analysis. The ideal HRG with full chemical equilibrium does not provide an adequate description of data. Thus, the parameter $\gamma_S$ is also fitted. This subsection summarizes briefly the results obtained in Ref. [59]:

The resulting values of the temperature and the baryochemical potential are shown on the $T$-$\mu_B$ plane in Fig. 3.1. The grey band shows the freeze-out curve parametrization from the Ref. [69],

$$T_{\mathrm{A+A}}(\mu_B) \; = \; a \; - \; b\mu_B^2 \; - \; c\mu_B^4 \; , \tag{3.3}$$

where $a = 0.166 \pm 0.002$ GeV, $b = 0.139 \pm 0.016$ GeV$^{-1}$, and $c = 0.053 \pm 0.021$ GeV$^{-3}$. The fit of the CuteHRG results for central Pb+Pb and Au+Au collisions (excluding the ALICE point) with the same analytical function (3.3) yields quite different parameters, namely: $a = 0.157$ GeV, $b = 0.087$ GeV$^{-1}$, and $c = 0.092$ GeV$^{-3}$. This updated parametrization is shown by the red line in Fig. 3.1. The main difference to the old parameterization, particularly in the values of parameters $b$ and $c$, is primarily caused by the fits to the data at top two SPS energies, and the absence of the RHIC data. Exclusion of the ALICE point from the fit makes the $\mu_B = 0$ temperature value a prediction. Notably, this value in the updated line is close to the temperature extracted from the LHC data, both in the present analysis and by other authors [89, 90, 91].

## 3.3 Excluded-volume effects and thermal fits at LHC

In this section we study the EV effects on thermal fits by considering at first the model with the minimum number of fitting parameters: the chemical equilibrium HRG with "Diagonal" EV corrections. Hadron yields are analyzed at the highest available collision energy, namely in Pb+Pb collisions at $\sqrt{s_{\mathrm{NN}}} = 2.76$ TeV in the ALICE experiment at LHC. Here the asymmetry in the production of particles and anti-particles is vanishingly small. This implies that, within the HRG sce-

nario, the (baryo)chemical potential $\mu_B$ is close to zero. Then the hadron yield ratios are determined in the HRG by a single parameter, the chemical freeze-out temperature $T^{\text{fo}}$.

### 3.3.1    Scenarios for eigenvolume interactions

Different hadron-hadron interactions are simulated by employing three different parametrizations for the hadron EV interactions. The trivial case, namely that all hadrons have the same constant eigenvolumes, is omitted. In this case EV corrections cancel out when ratios of yields are fitted, and do not influence $T^{\text{fo}}$ [40, 69, 92]

1. Our first case assumes that all mesons are point-like, i.e. $v_M = 0$, and that all baryons have a fixed, finite EV, $v_B > 0$. Note that in this case mesons and baryons still "see" each other: the point-like mesons cannot penetrate into the finite-sized baryons. The effective hard-core radius of baryon here is $r_B = 0.3$ fm. This choice is motivated by the successful comparison of this model with lattice QCD data on pressure. As reported in Ref. [93], the lattice data are described up to at least $T = 190$ MeV. Our calculations suggest that the lattice QCD pressure is described fairly well by this model even up to $T = 250$ MeV.

2. The second case employs the Bag-model motivated parametrization [94] where the hadrons' eigenvolumes are proportional to hadrons' masses, i.e.

$$v_i = m_i/\varepsilon_0. \tag{3.4}$$

   This had been used for heavy Hagedorn resonance thermodynamics [46, 49]. The effect on the particle yield ratios was studied in [95]. The HRG with eigenvolume corrections as given by (3.4) has recently also been used successfully to model the hadronic part of the crossover QCD equation of state, which compares favorably to the lattice data [96, 97].

3. The third case includes only baryon-baryon and antibaryon-antibaryon EV interactions and neglects the EV interactions for baryon-antibaryon, meson-baryon, and meson-meson pairs. In this case the system consists of three

Table 3.1: The hadron midrapidity yields for $0-5\%$ most central Pb+Pb collisions measured by the ALICE collaboration and used in the thermal fits in this work.

| Particle | Measurement $(dN/dy)$ | Reference |
|:---:|:---:|:---:|
| $\pi^+$ | $733 \pm 54$ | [85] |
| $\pi^-$ | $732 \pm 52$ | [85] |
| $K^+$ | $109 \pm 9$ | [85] |
| $K^-$ | $109 \pm 9$ | [85] |
| $p$ | $34 \pm 3$ | [85] |
| $\bar{p}$ | $33 \pm 3$ | [85] |
| $\Lambda$ | $26 \pm 3$ | [86] |
| $\Xi^-$ | $3.57 \pm 0.27$ | [87], [91] |
| $\Xi^+$ | $3.47 \pm 0.26$ | [87], [91] |
| $\Omega + \bar{\Omega}$ | $1.26 \pm 0.22$ | [87], [91] |
| $K_S^0$ | $110 \pm 10$ | [86] |
| $\phi$ | $13.8 \pm 0.5 \pm 1.7$ | [88] |

independent sub-systems: non-interacting mesons, EV baryons, and EV antibaryons. Hence, meson densities are given by the ideal gas relations. The densities of (anti)baryons are calculated by solving Eqs. (2.12) and (2.13), separately for baryons and for antibaryons. The eigenvolume parameter value $v_B$ of the baryon-baryon interaction is fixed by fitting the ground state of nuclear matter with the van der Waals equation (see details in Chapter 7). This gives $v_B = 3.42$ fm$^3$, corresponding to an "effective hard-core radius" of $r_B \simeq 0.6$ fm.

## 3.3.2 Results of the thermal fits

The thermal fits are performed using CuteHRG for the midrapidity yields of the charged pions, charged kaons, (anti)protons, $\Xi^-$, $\Xi^+$, $\Omega$, $\bar{\Omega}$, $\Lambda$, $K_S^0$, and $\phi$, measured by the ALICE collaboration in the 0-5% most central Pb+Pb collisions at $\sqrt{s_{\mathrm{NN}}} = 2.76$ TeV [85, 86, 87, 88]. Note that the centrality binning for $\Xi$ and $\Omega$ hyperons is different from the other hadrons. Thus, we take the midrapidity yields of $\Xi$ and $\Omega$ in the $0-5\%$ centrality class from Ref. [91], where they were obtained using the interpolation procedure. The data used in thermal fits is listed in Table 3.1.

Figure 3.2 shows the dependence of the $\chi^2/N_{\mathrm{dof}}$ of the fit on the temperature
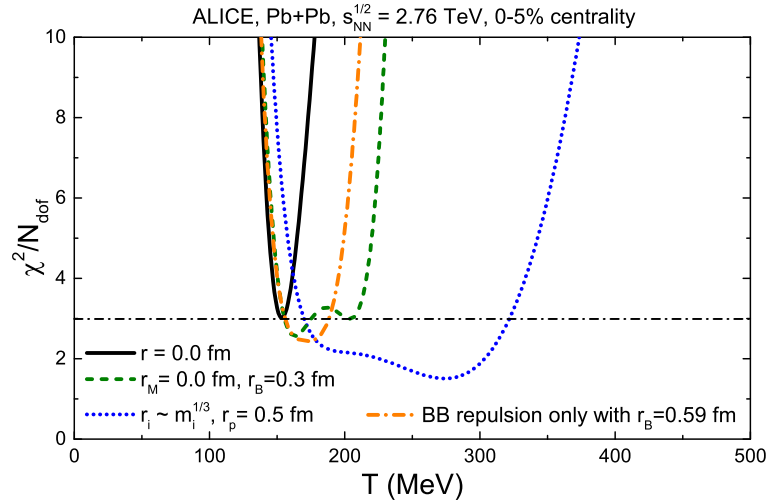
Figure 3.2:    The temperature dependence of $\chi^2/N_{\mathrm{dof}}$ of fit to ALICE data on hadron yields in 0-5% most central Pb+Pb collisions at 2.76 TeV within the point-particle HRG model (solid black curve), the two-component eigenvolume HRG model with point-like mesons and baryons of fixed size (dashed green line), the bag-like eigenvolume HRG model (dotted blue line), and the model with only baryon-baryon and antibaryon-antibaryon eigenvolume interactions (orange dash-dotted line).

for four cases: the hadron resonance gas with point-particle hadrons, i.e. for $v_i = 0$, and for the three distinct eigenvolume interactions scenarios described above. At each temperature, the only remaining free parameter, namely the system volume (radius) per unit slice of rapidity, is fixed to minimize the $\chi^2$ at this temperature.

Different considered cases give drastically different pictures. The point-particle HRG yields a narrow minimum around $T \simeq 154$ MeV with $\chi^2/N_{\mathrm{dof}} \simeq 30.1/10$. These values are consistent with previous fits to the ALICE hadron yields [89, 90]. Finite eigenvolumes, on the other hand, generally increase the freeze-out temperature and improve the fit quality.

The first eigenvolume case, $r_M = 0$ and $r_B = 0.3$ fm, yields two broad minima at about 160 MeV and at about 210 MeV in the temperature dependence of the $\chi^2$ values (see dashed green line in Fig. 3.2). The global minimum is located at $T \simeq$ 163 MeV with $\chi^2/N_{\mathrm{dof}} \simeq 25.6/10$. In general, the fit quality stays comparable to the point-particle case in the whole $T = 155 - 210$ MeV temperature range. The

fit result is rather sensitive to the choice of the baryon radius $r_B$. For example, for $r_B = 0.35$ fm there is a narrower minimum around $T \simeq 173$ MeV in the temperature dependence of the $\chi^2$ distribution, while for $r_B = 0.25$ fm there are two local minima, at $T \simeq 159$ MeV and at $T \simeq 234$ MeV (not shown here).

The bag model mass-proportional eigenvolumes with $r_p = 0.5$ fm (second EV case) lead to drastic changes in the $\chi^2$ profile: the data are described better than in the point-particle ($r_p = 0$ fm) case, for a very wide $T = 170 - 320$ MeV temperature range. The global minimum is located at $T = 274$ MeV with $\chi^2/N_{\mathrm{dof}} \simeq 15.1/10$. The 2nd minimum at $T \simeq 270$ MeV is definitely prone to controversy: the corresponding equation of state is plagued by superluminal speeds of sound at high temperatures, and is characterized by large hadron densities. This implies that the high-temperature part seems to be outside of the range where van der Waals excluded volume model should be applied. We do not suggest this as a new, improved, set of chemical freeze-out parameters. Nevertheless, this is a remarkable illustration of the sensitivity of the thermal fits to the modeling of the EV interactions.

The third case considers only baryon-baryon and antibaryon-antibaryon eigenvolume interactions. This yields a rather wide minimum around $T = 172$ MeV with a minimum value of $\chi^2/N_{\mathrm{dof}} \simeq 24.4/10$. The fit is improved over the point-particle HRG. The result appears rather similar to the first EV case studied here. This model is also fully consistent with the lattice QCD pressure up to at least $T = 200$ MeV.

### 3.3.3 Origin of the two minima

The $\chi^2$ profiles shown in Fig. 3.2 for first two EV cases both feature two distinct minima. This is in stark contrast to the ideal HRG, where only one local minimum is observed. Where does the 2nd minimum come from?

Let us consider the temperature dependence of the proton-to-pion ratio: In the ideal HRG this dependence is strictly monotonic: the $p/\pi$ ratio increases with temperature. In the "Diagonal" EV HRG, the particle densities have an additional Boltzmann factor[1] $n_i \propto \exp(-v_i \, p/T)$. If protons and pions have the

---

[1]For this qualitative analysis we neglect the role of quantum statistics which does not play
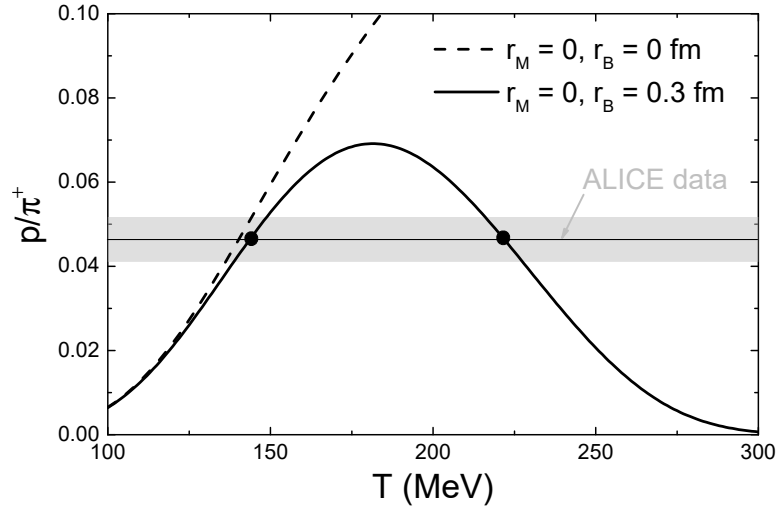
Figure 3.3:    The temperature dependence of the $p/\pi^+$ ratio in the ideal HRG (dashed line) and in the first EV case (solid line). The horizontal line with a band corresponds to the ALICE data.

same eigenvolumes, then this factor cancels out. However, if protons have a large EV as compared to pions then the protons are suppressed more strongly. Hence, the proton-to-pion ratio will decrease at high densities, and, thus, the $T$-dependence of the $p/\pi$ ratio will be non-monotonic. The right panel of Fig. 3.3 shows this ratio as calculated for the ideal HRG (dashed line), and for the first EV case (solid line). This numerical calculation also includes the feeddown correction. The non-monotonic structure of $p/\pi$ is clearly observed: the ALICE measurement of the value of the $p/\pi$ ratio does correspond to *two* different temperatures, $T_1 \simeq 150$ MeV and $T_2 \simeq 250$ MeV, in clear contrast to the ideal HRG and to the "all constant" eigenvolume assumption. This kind of non-monotonic dependence is present also for many other hadronic ratios. It is the basic reason for the appearance of two minima in the $\chi^2$ profiles.

More EV scenarios for thermal fits at LHC were recently considered in Ref. [58], mainly regarding different possibilities for meson-meson, meson-baryon, baryon-baryon, and antibaryon-baryon EV interactions. The emergence of the 2nd minimum was reported and similar conclusions regarding general sensitivity of thermal fits to the modeling of EV interactions were obtained.

---

a significant role.

These results show that thermal fits are very delicate – they are surprisingly sensitive to the details of the modeling of the eigenvolume interactions. It appears that chemical freeze-out temperatures can be fitted to LHC heavy-ion data on hadron yields only with a sizable uncertainty.

### 3.3.4   Role of light nuclei

The yields of the light nuclei were not considered in all previous fits presented in this thesis. There are reasons why inclusion of light nuclei into thermal fits is questionable, in particular related to their small binding energies. Nevertheless, they are sometimes included into thermal fits [89], and may help to stabilize them in some cases. It was checked that the inclusion of light nuclei into fits does not influence the fits considerably for the mass-proportional EV parameterization. For another EV scenarios it appears that the fit is extremely sensitive to the assumptions regarding the eigenvolumes of different nuclei.

To illustrate this let us consider the (anti)deuteron yields in the 0-10% AL-ICE centrality. The actual data used for fitting thus now includes the hadronic midrapidity yields of charged pions, charged kaons, and (anti)protons [85], (anti)$\Xi^-$ and (anti)$\Omega$ [87], (anti)$\Lambda$ and $K_S^0$ [86, 98], $\phi$ [88], and, additionally,c (anti)deuterons [99].

The addition of light nuclei requires additional assumptions regarding their eigenvolumes. Two scenarios for deuteron eigenvolume are considered: (1) deuteron has same eigenvolume as baryons, i.e. $r_p = r_d = 0.3$ fm; (2) deuteron has a twice larger eigenvolume compared to baryons, i.e. $v_d = 2v_p$ which implies $r_d \simeq 0.38$ fm. The results of the calculations of $\chi^2$ temperature profile are depicted in Fig. 3.4. Note that here $\mu_B$ is also fitted at each $T$ and found to be consistent with zero within fit errors.

If deuterons are assumed to have same eigenvolume as protons then the $\chi^2$ profile has a regular structure with a minimum at $T \simeq 161$ MeV. Thus, it would seem that inclusion of deuterons into thermal fit would stabilise them with regards to the modeling of EV corrections. This conclusion, however, is not supported by further analysis. Changing deuteron eigenvolume to a physically more motivated value equal to twice that of proton one gets a very different $\chi^2$ profile: a two-
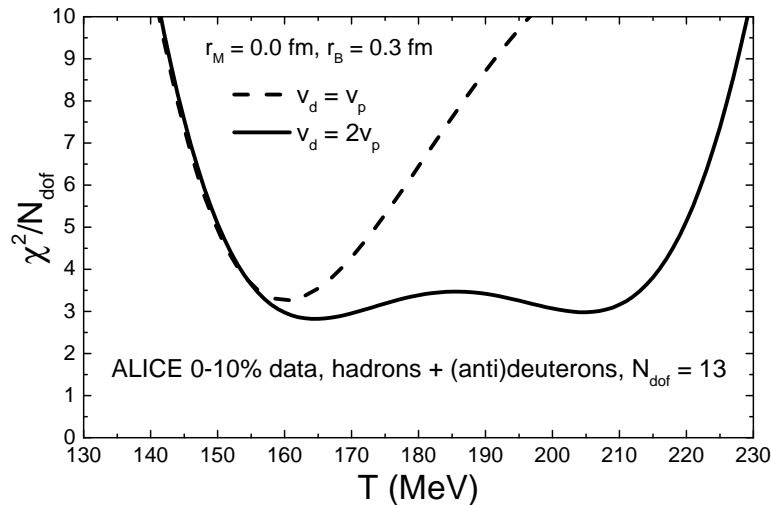
Figure 3.4: The temperature dependence of $\chi^2/N_{\rm dof}$ of fit to ALICE data on hadron + (anti)deuteron yields in 0-10% most central Pb+Pb collisions at 2.76 TeV within eigenvolume HRG model with point-like mesons, baryons with hard-core radius of 0.3 fm. Two different assumptions for an eigenvolume of a deuteron are considered: $r_d = r_p = 0.30$ fm (dashed line) and $r_d = 2^{1/3} r_p \simeq 0.38$ fm (solid line).

minimum structure in a wide 155-210 MeV temperature range, with improved fit quality at global minimum. This change is attributed to a larger suppression of (anti)deuteron yield at higher temperatures due to having a larger eigenvolume.

It is quite remarkable that a fit can be so sensitive to the properties of only single particle species. Similarly, the inclusion of heavier nuclei ($^3$He and $^3_\Lambda$H) does not help to stabilise the fit, as it requires more assumptions regarding their eigenvolumes. The thermal fits remain very sensitive to these assumptions (see [63] for further details). We therefore conclude that introduction of light nuclei into thermal fits leads to a further destabilisation of the fit as it requires non-trivial assumptions regarding their eigenvolumes. Due to this large sensitivity, and to the generally questionable nature of inclusion of light nuclei into thermal fits, the yields of light nuclei are not considered further.
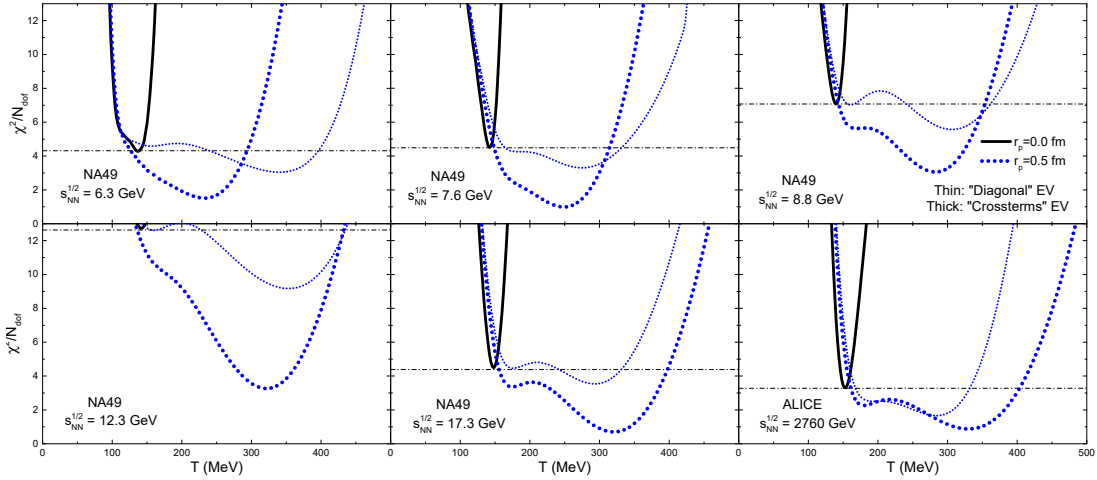
Figure 3.5: The temperature dependence of $\chi^2/N_{\mathrm{dof}}$ of fits to data of the NA49 and ALICE collaborations on hadron yields in central Pb+Pb and Au+Au collisions within the ideal HRG model (solid black lines), the "Diagonal" eigenvolume model (thin dotted blue lines), and the "Crossterms" eigenvolume model (thick dotted blue lines). The mass-proportional eigenvolumes with a hard-core proton radius of 0.5 fm are used.

## 3.4 Excluded-volume effects at lower energies

The surprisingly strong sensitivity of thermal fits to LHC data to the details of the modeling of eigenvolume interactions does of course also influences the HRG analysis at lower collision energies: Here the different, finite (baryo)chemical potentials play an important additional role. Hence the hadron yield data from the NA49 collaboration are analyzed for the most central Pb+Pb collisions at $\sqrt{s_{\mathrm{NN}}} = 6.3, 7.6, 8.8, 12.3,$ and $17.3$ GeV. Both the "Diagonal" and the "Crossterms" EV models, within the Boltzmann approximation, are employed here, and the bag-model mass-proportional EV parametrization is considered.

The resulting temperature profiles of the $\chi^2$ are shown in Fig. 3.5 for $r_p = 0.5$ fm. The results confirm the findings at the LHC energy: the ideal HRG fits give single narrow minima while the bag model EV fits yield improved $\chi^2$ values in very wide high-temperature range, at all considered collision energies. The appearance of two local minima in $\chi^2(T)$ at SPS energies in the EV fits has the same origin as the one previously elaborated for the LHC energy. Both EV models considered give the same qualitative picture. However, there are signifi-
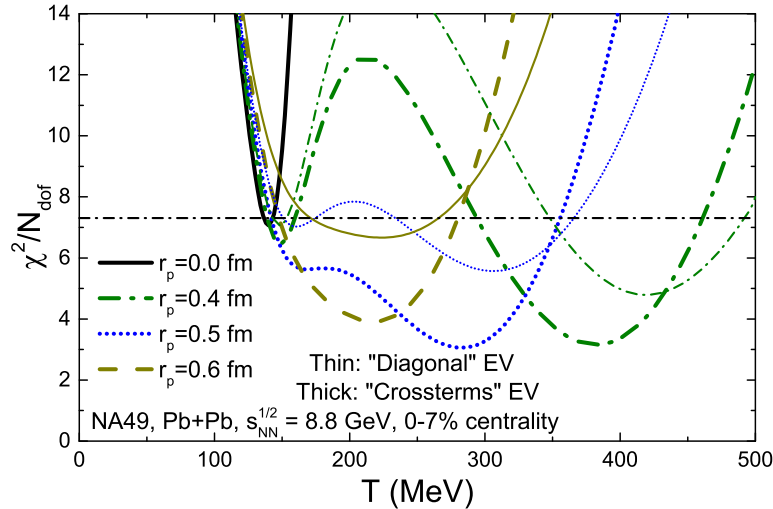
Figure 3.6: The temperature dependence of $\chi^2/N_{\mathrm{dof}}$ of fits to data of the NA49 Collaboration on hadron yields in central Pb+Pb collisions at $\sqrt{s_{\mathrm{NN}}} = 8.8$ GeV within the point-particle HRG model (solid black curve), the "Diagonal" eigenvolume model (thin colored lines), and the "Crossterms" eigenvolume model (thick colored lines). The mass-proportional eigenvolumes with hard-core proton radius of 0.4, 0.5, and 0.6 fm are used.

cant quantitative differences, especially at higher temperatures: the "Crossterms" model yields a considerably better description of the data, however with challengingly high HRG temperatures ($T_{\mathrm{fit}} \sim 300$ MeV). Can this be reconciled in a new paradigm, namely that there is a large contribution of hadrons in the system, even at these extreme temperatures? Or do we see pre-freezeout emission of hadrons from the hot initial phase of the temporal evolution of the early system?

In Fig. 3.6 the temperature dependence of the $\chi^2$ for three different values of $r_p$, namely for $r_p = 0.4$, 0.5, 0.6 fm is shown for the SPS data at $\sqrt{s_{\mathrm{NN}}} = 8.8$ GeV. The behavior of the $\chi^2$ for different values of $r_p$ shown in Fig. 3.6 is representative for all other collision energies considered in the present work. For $r_p = 0.4$ fm the temperature dependence of $\chi^2$ shows two distinct local minima: the first one is located close to the minimum for point-particle HRG and the second one is at much higher temperatures and with considerably smaller $\chi^2$. This trend is continued when even lower values of $r_p$ are considered. For $r_p = 0.5$ fm and $r_p = 0.6$ fm a wide (double)minimum structure is observed in the temperature dependence of $\chi^2$ and, at all energies, the fit quality is better in EV models than
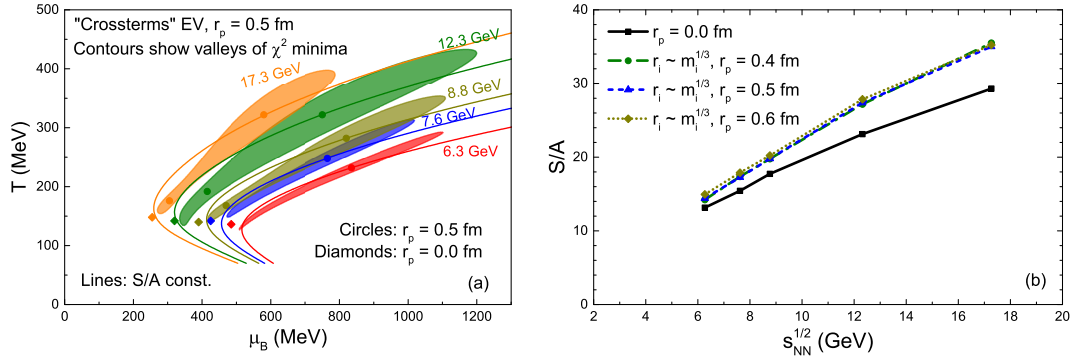
Figure 3.7: (a) Regions in the $T$-$\mu_B$ plane where the "Crossterms" eigenvolume HRG model with bag-like constant $\varepsilon_0$ fixed to reproduce the hard-core radius of $r_p = 0.5$ fm yields a better fit to the NA49 data as compared to the point-particle HRG model. The solid lines show the isentropic curves for the eigenvolume model, which go through the global $\chi^2$ minima. (b) Collision energy dependence of entropy per baryon at global minima of thermal fits to NA49 data.

in the point-particle case for a very wide high-temperature range.

The EV effects on the fitted values of $\mu_B$ are illustrated by the structure of the $\chi^2$ values in the $T$-$\mu_B$ plane in Fig. 3.7. Only the "Crossterms" model is shown for clarity. Figure 3.7a depicts contours of the regions in the $T$-$\mu_B$ plane where the fit quality of NA49 data in the EV model is better than in the ideal HRG. The locations of the fit minima within ideal HRG are shown by diamonds, consistent with the systematics established in numerous previous studies. The EV HRG model fits each yield a whole range of $T - \mu_B$ pairs, each with similarly good fit quality for all considered cases, at a given bombarding energy and for a given set of radii. These $T$-$\mu_B$ pair contours form valleys in the $T - \mu_B$ plane, following lines of nearly constant entropy per baryon, $S/A$. The energy dependence of these $S/A$ values is exhibited in Fig. 3.7b. Note that the $S/A$ values, as extracted at different energies, are robust: $S/A$ is virtually independent of the details of the EV interactions modeling and also of the specific $T - \mu_B$ values in which the $\chi^2$-values are similar.

The interpretation of the high values of temperature and baryochemical potential obtained within the EV HRG fits at SPS is prone to controversy, as in the case of the LHC data fits. These fits do give a significant and systematic improvement in the reproduction of the data. They are also plagued by the irregular behavior

of the speed of sound, by a difficulty in reconciliation of lattice QCD results, and by high values of the packing fraction. Thus, the extracted high values of $T$ and $\mu_B$ are not interpreted as realistic estimates of chemical equilibrium freeze-out conditions, but rather as an illustration of the hitherto unexplored sensitivity of thermal fits to the modeling of EV interactions in the HRG.

# Chapter 4

# Monte Carlo approach to excluded-volume interactions

The EV effects were considered only for HRG in the GCE in the previous two chapters. Conserved charges are conserved only on average in the GCE, but differ from one microscopic state to another. The exact conservation of the conserved charges becomes important for smaller systems. Such exact conservation of charges can be enforced within the canonical ensemble (CE) [100]. The CE formulation of the ideal HRG model was successfully used to describe the hadron production data in small systems, such as (anti)proton-proton and $e^+e^-$ collisions [101, 102, 103, 104]. The CE strongly influences the strange [105, 106] and charm [107] hadron multiplicities as the average total numbers of strange and charm charges are often not large (of the order of unity or smaller). It should be also noted that for systems of non-interacting particles the CE effects lead to noticeable suppression of particle number fluctuations for statistical systems even in the thermodynamic limit [108].

To the best of our knowledge, the CE formulation for the excluded-volume HRG is presently missing. Thus, the influence of EV effects on the thermodynamic properties within the CE was never explored. In this chapter a Monte Carlo (MC) procedure is proposed which allows to do exactly that.

# 4.1  GCE partition function of different EV models

Our consideration will be restricted to the case of classical (Maxwell-Boltzmann) statistics. It is useful to define the single-particle function:

$$z_i(T) \;=\; \frac{d_i}{2\pi^2} \int_0^\infty k^2 dk \; \exp\left[ - \frac{(k^2 + m_i^2)^{1/2}}{T} \right] \;,\qquad (4.1)$$

where $d_i$ and $m_i$ are, respectively, the $i$th particle degeneracy factor and mass, and where $T$ is the system temperature. In the single-component system the ideal gas GCE partition function reads ($z_i \equiv z$):

$$\mathcal{Z}_{\mathrm{id}}(T,V,\mu) = \sum_{N=0}^\infty \exp\left( \frac{\mu N}{T} \right) \frac{(z\,V)^N}{N!} \;=\; \exp(e^{\mu/T} z\, V) \;,\qquad (4.2)$$

where $V$ is the total volume of the system and $\mu$ is the chemical potential. The number of particles $N$ is fixed in the CE, and has the Poisson distribution, $P(N) = \langle N \rangle^N \exp(-\langle N \rangle)/N!$, in the GCE with average value $\langle N \rangle = \exp(\mu/T) z V$.

### van der Waals EV model

In the van der Waals EV model the volume $V$ is substituted by the available volume $V_{\mathrm{av}} = V - vN$, where $v = 16\pi r^3/3$ is the eigenvolume parameter. This results in the following GCE partition function

$$\mathcal{Z}_{\mathrm{EV}}(T,V,\mu) = \sum_{N=0}^\infty \exp\left( \frac{\mu N}{T} \right) \frac{(V \,-\, vN)^N}{N!} \theta(V - vN) z^N \;,\qquad (4.3)$$

where the $\theta$-function ensures that sum of eigenvolumes of the particles does not exceed the total system volume. In the thermodynamic limit, i.e. when $V \to \infty$, the system pressure and particle number density are calculated according to (2.9) and (2.10), respectively.

In the GCE one finds that the particle number, $N$, fluctuates around its aver-

age value $\langle N \rangle = V n$. A useful measure of the particle number fluctuations is the scaled variance $\omega[N]$. It was calculated analytically in Ref. [109]:

$$\omega[N] \equiv \frac{\langle N^2 \rangle - \langle N \rangle^2}{\langle N \rangle} = (1 - v\,n)^2 \,, \tag{4.4}$$

see also Ref. [110]. Note that analytical expressions in Eqs. (2.9), (2.10), and (4.4) are obtained in the thermodynamic limit $V \to \infty$. At $v = 0$ they are reduced to the ideal gas expressions. In particular, the particle number distribution $\mathcal{P}(N)$ is transformed to the Poisson distribution with $\omega[N] = 1$.

## "Diagonal" EV model

The GCE partition function of the "Diagonal" EV model (Sec. 2.2.2) has the following form for $f$ hadron species ($i, j = 1, \ldots, f$):

$$\mathcal{Z}_{\mathrm{DE}}(T, V, \mu_1, \ldots, \mu_f) = \prod_{i=1}^{f} \sum_{N_i=0}^{\infty} \exp\left(\frac{\mu_i N_i}{T}\right) \frac{[(V - \sum_j v_j N_j)\, z_i]^{N_i}}{N_i!}$$
$$\times\, \theta(V - \sum_{j=1} v_j N_j) \,, \tag{4.5}$$

where subscript DE will denote this model in this chapter. The analytic expressions for pressure and particle number densities in the thermodynamic limit are given by Eqs. (2.12) and (2.13).

## "Crossterms" EV model

The GCE partition function of the "Crossterms" EV model (Sec. 2.2.3) has the following form

$$\mathcal{Z}_{\mathrm{CRS}}(T, V, \mu_1, \ldots, \mu_f) = \prod_{i=1}^{f} \sum_{N_i=0}^{\infty} \exp\left(\frac{\mu_i N_i}{T}\right) \frac{[(V - \sum_j \tilde{b}_{ji} N_j)\, z_i]^{N_i}}{N_i!}$$
$$\times\, \theta(V - \sum_{j=1} \tilde{b}_{ji} N_j) \,, \tag{4.6}$$

where subscript CRS will denote the Crossterms model in this chapter, and where $\tilde{b}_{ij}$ are given by (2.15) and (2.17).

The pressure and particle densities in the thermodynamic limit are given by Eqs. (2.18) and (2.19), respectively.

## 4.2 Canonical ensemble

In the CE, the conserved charges are conserved in each microscopic state of the system. This can be achieved by adding the corresponding delta functions in the GCE partition function. For the three EV models described in the previous section one has the following CE partition functions:

$$
Z_{\mathrm{EV}}(T, V, N) \;=\; \frac{(V \; - \; vN)^N}{N!} \, z^N \;,
\tag{4.7}
$$

$$
Z_{\mathrm{DE}}(T, V, \{Q\}) \;=\; \sum_{N_1=0}^{\infty} \cdots \sum_{N_f=0}^{\infty} \frac{\left[ \left(V - \sum_j v_j N_j\right) z_i \right]^{N_i}}{N_i!}
$$

$$
\times \; \theta\!\left(V - \sum_j v_j N_j\right) \prod_{k=1}^{q} \delta\!\left(Q_k - \sum_j Q_k^{(j)} N_j\right) ,
\tag{4.8}
$$

$$
Z_{\mathrm{CRS}}(T, V, \{Q\}) \;=\; \sum_{N_1=0}^{\infty} \cdots \sum_{N_f=0}^{\infty} \frac{\left[ \left(V - \sum_j \tilde{b}_{ji} N_j\right) z_i \right]^{N_i}}{N_i!}
$$

$$
\times \; \theta\!\left(V - \sum_j \tilde{b}_{ji} N_j\right) \prod_{k=1}^{q} \delta\!\left(Q_k - \sum_j Q_k^{(j)} N_j\right) .
\tag{4.9}
$$

In Eqs. (4.8) and (4.9), $\{Q\} = Q_1, \dots, Q_q$ are the set of conserved charges and $Q_k^{(j)}$ is the $k$th charge of the particle species $j$. For a single-component case one identifies the single conserved charge $Q$ with the particle number $N$, i.e. $Q \equiv N$.

For the ideal gas, i.e. for $v_i \equiv 0$ in (4.8) or $\tilde{b}_{ij} \equiv 0$ in (4.9), the thermodynamic properties can be calculated analytically [108]. To our knowledge, no approach has been developed to calculate the moments of the multiplicity distribution for the EV models in the CE formulation of HRG.

## 4.3   Monte Carlo approach

### 4.3.1   Grand canonical ensemble

The GCE partition functions listed in Section 4.1 determine the probability distribution of particle numbers at given values of the thermodynamic parameters for the corresponding EV models. In the general case, the probability to have a microstate with number of particles $(N_1, \ldots, N_f)$ has the form

$$\mathcal{P}(N_1, \ldots, N_f; T, V, \{\mu_Q\}) \propto F(N_1, \ldots, N_f; T, V, \{\mu_Q\}) \times \Theta(N_1, \ldots, N_f; V),$$
(4.10)

where $\Theta(N_1, \ldots, N_f; V)$ ensures that only the microstates where the sum of all proper particle eigenvolumes does not exceed the total volume of the system are considered, $\{\mu_Q\} \equiv \mu_1, \ldots, \mu_q$ corresponds to the independent chemical potentials which regulate the conserved charges $Q_1, \ldots, Q_q$ in the system. The function $F(N_1, \ldots, N_f; T, V, \{\mu_Q\})$ is a smooth function of particle numbers within the domain of allowed microstates. The chemical potential of $i$th particle species is

$$\mu_i \;=\; \sum_{k=1}^{q} Q_k^{(i)} \, \mu_k \;,$$
(4.11)

where $Q_k^{(i)}$ is the $k$th charge of $i$th particle. In the HRG the number of conserved charges is normally much smaller than the number of particle species (i.e., $q \ll f$). It is evident that $F$ is defined up to a multiplicative factor which may depend on thermodynamic variables but is independent of the particle numbers.

Both the $F$ and $\Theta$ functions are completely defined for the models listed in Section 4.1:

$$F_{\mathrm{EV}}(N; T, V, \mu) \;=\; \frac{\left[(V - vN) \, z \, e^{\mu/T}\right]^N}{N!} \;,$$
(4.12)

$$\Theta(N; V) \;=\; \theta(V - vN) \;;$$
(4.13)

$$F_{\mathrm{DE}}(N_1,\ldots,N_f;T,V,\{\mu_Q\}) = \prod_{i=1}^{f} \frac{\left[(V - \sum_j v_j N_j)\, z_i\, e^{\mu_i/T}\right]^{N_i}}{N_i!} \,, \qquad (4.14)$$

$$\Theta(N_1,\ldots,N_f;V) = \theta(V - \sum_j v_j N_j) \,; \qquad (4.15)$$

$$F_{\mathrm{CRS}}(N_1,\ldots,N_f;T,V,\{\mu_Q\}) = \prod_{i=1}^{f} \frac{\left[(V - \sum_j \tilde{b}_{ji} N_j)\, z_i\, e^{\mu_i/T}\right]^{N_i}}{N_i!} \,, \qquad (4.16)$$

$$\Theta(N_1,\ldots,N_f;V) = \prod_{i=1}^{f} \theta(V - \sum_j \tilde{b}_{ji} N_j) \,. \qquad (4.17)$$

In the ideal gas limit the probability $\mathcal{P}$ (4.10) is reduced to a product of the $f$ independent Poisson distributions, i.e. $\mathcal{P} \propto \Pi$ where

$$\Pi(\{N_i\};T,V,\{\mu_Q\}) = \prod_{i=1}^{f} \frac{\langle N_i\rangle^{N_i}}{N_i!}\, e^{-\langle N_i\rangle} \,. \qquad (4.18)$$

The probability function $\mathcal{P}$ (4.10) cannot be decomposed into a product of independently distributed variables in the presence of finite eigenvolumes in a multi-component system. Thus, a straightforward sampling of particle numbers looks problematic. To avoid this problem we rewrite the probability $\mathcal{P}$ (4.10) in the following form

$$\mathcal{P}(\{N_i\};T,V,\{\mu_Q\}) \propto \frac{F(\{N_i\};T,V,\{\mu_Q\})}{\Pi(\{N_i\};T,V,\{\mu_Q\})} \times \Pi(\{N_i\};T,V,\{\mu_Q\}) \times \Theta(\{N_i\};V),$$
$$(4.19)$$

where $\Pi(\{N_i\};T,V,\{\mu_Q\})$ is an auxiliary function, taken in the form of Eq. (4.18) with Poisson rate parameters $\langle N_i\rangle$ which can, in general, be chosen arbitrarily and differently for different values of $T$, $V$, and $\{\mu_Q\}$. The Monte Carlo (MC) sampling of the particle numbers can be then performed with the help of the importance sampling technique (see e.g. [111]). In practical calculations, the parameters $\langle N_i\rangle$ should be chosen in a way so that the auxiliary distribution $\Pi$ resembles the true distribution $F$ as closely as possible. This helps to avoid over-sampling of the "unimportant" low-probability regions and makes the statistical

convergence faster. In our calculations we will utilize the multi-Poisson distribution in Eq. (4.18) with parameters $\langle N_i \rangle$ calculated within the corresponding analytic models defined in Section 4.1. Of course, it is also possible to use an auxiliary distribution which is different from the multi-Poisson distribution in Eq. (4.18).

Denoting the ratio $F/\Pi$ as weight $w$, the probability distribution can be written

$$P(\{N_i\}; T, V, \{\mu_Q\}) \propto w(\{N_i\}; T, V, \{\mu_Q\}) \times \Pi(\{N_i\}; T, V, \{\mu_Q\}) \times \Theta(\{N_i\}; V).$$
(4.20)

The MC sampling procedure includes the following steps:

1. Sample the numbers $(N_1, \ldots, N_f)$ from the auxiliary multi-Poisson distribution $\Pi$ (4.18).

2. If the indicator function $\Theta$ (4.10) fails for the sampled numbers, then reject the event and go back to the first step. If $\Theta$ passes, then go to the next step.

3. Calculate the weight $w = F/\Pi$ and accept the event with this weight.

Let us have $l = 1, \ldots, M$ samples of particle numbers $\{N_i\}_l$ with weights $w_l$. The sample mean of any function $f(N_1, \ldots, N_f)$ of the particle numbers is calculated in the following way

$$\langle f(N_1, \ldots, N_f) \rangle_M = \frac{\sum_{l=1}^{M} w_l f(\{N_i\}_l)}{\sum_{l=1}^{M} w_l}.$$
(4.21)

It is evident that in the limit of $M \to \infty$ the sample mean will converge to the GCE expectation value, i.e.

$$\langle f(N_1, \ldots, N_f) \rangle_M \xrightarrow[M \to \infty]{} \langle f(N_1, \ldots, N_f) \rangle_{\mathrm{GCE}}.$$
(4.22)

The statistical error estimate for $\langle f(N_1, \ldots, N_f) \rangle_M$ reads

$$\sigma_f^2 = \frac{\sum_{l=1}^{M} w_l^2 [f_l - \langle f \rangle_M]^2}{(\sum_{l=1}^{M} w_l)^2},$$
(4.23)

where $f_l \equiv f(\{N_i\}_l)$.

### 4.3.2   Monte Carlo method in the canonical ensemble

In the CE, the conserved charges $\{Q\} = Q_1, \ldots, Q_q$ in the system are fixed to their exact values in each microscopic state. The exact charge conservation is enforced by adding the corresponding delta functions into the probability distribution, i.e.

$$\mathcal{P}(\{N_i\}; T, V, \{Q\}) \propto F(\{N_i\}; T, V, \{\mu_Q = 0\}) \times \Theta(\{N_i\}; V)$$
$$\times \prod_{k=1}^{q} \delta(Q_k - \sum_j Q_k^{(j)} N_j) \,. \qquad (4.24)$$

Similarly to the GCE, the MC approach within the CE proceeds by introducing into (4.24) the product of auxiliary Poisson distributions, i.e.

$$\mathcal{P}(\{N_i\}; T, V) \propto w(\{N_i\}; T, V, \{Q\}) \times \Pi(\{N_i\}; T, V, \{Q\})$$
$$\times \Theta(\{N_i\}; V) \times \prod_{k=1}^{q} \delta(Q_k - \sum_j Q_k^{(j)} N_j) \,. \qquad (4.25)$$

The MC sampling in CE includes only one additional step: if the generated configuration does not satisfy the exact charge conservation laws then it is rejected. Our approach is quite similar to the importance sampling of ideal HRG in micro canonical ensemble performed previously in Refs. [112, 113]. In fact, we use the multi-step procedure of [113] for sampling the CE particle yields, which are subject to the constraint of exact charge conservation. This algorithm gives a significant performance boost compared to a straightforward independent sampling of all particle multiplicities from a multi-Poisson distribution.

## 4.4   Calculation results

### 4.4.1   Finite-size effects in the GCE

Let us consider first a single-component gas with EV interactions in the GCE. When the EV effects are present, the intensive quantities depend explicitly on

the total system volume. In particular, the particle number density equals to zero if the system volume $V$ is smaller than the eigenvolume of a single particle. The finite-size effects cannot be described by the analytic formulas presented in Section 4.1, as they all are derived under the assumption of the thermodynamic limit. However, these effects can be studied with the help of the MC procedure described in Section 4.3.

A simple example to illustrate the finite-size effect is considered. We assume a single-component gas of particles with mass of 1 GeV, which is a typical energy scale for hadronic systems. Vanishing chemical potential, i.e. $\mu = 0$, and a temperature of $T = 150$ MeV are taken. In order to mimic a presence of large number of hadron states in a realistic HRG a rather high degeneracy factor of $g = 150$ is employed in calculations. This is important as the magnitude of the eigenvolume effects scales with the total number of the finite-sized hadrons in the system.

The system-size dependence of the particle number density, $n = \langle N \rangle / V$, is calculated using the MC method. Additionally, we consider the scaled variance, $\omega[N]$, of the particle number fluctuations. The Poisson rate parameter $\langle N \rangle$ in the auxiliary distribution $\Pi$ (4.18) is taken to be $\langle N \rangle = n_{\mathrm{EV}}(T, \mu = 0; r) \, V$, where $n_{\mathrm{EV}}(T, \mu = 0; r)$ is the particle number density in thermodynamic limit ($V \to \infty$), which is calculated analytically from Eqs. (2.9) and (2.10). The dependence of $n$ on the total system radius $R$ (defined as $V \equiv 4\pi R^3 / 3$) is depicted in Fig. 4.1 for four different values of the hard-core particle radius ($r = 0$, 0.3 fm, 0.5 fm, and 1 fm). For each pair of $R$ and $r$ values we generate and perform an averaging over $10^5$ MC events. The calculations show a consistent approach of the particle density $n$ to its limiting value with increasing of $R$. The resulting limiting values at large $R$ in all cases appear to coincide with the corresponding values in the thermodynamic limit calculated from Eqs. (2.13) and (4.4). This is an expected result.

The number of terms in the GCE EV partition function (4.3) is finite due to the presence of the $\theta$-function. Thus, it is also possible to calculate the moments of the multiplicity distribution analytically, by explicitly summing over all $N$-states. More specifically, the GCE EV average of arbitrary function $f(N)$ is calculated
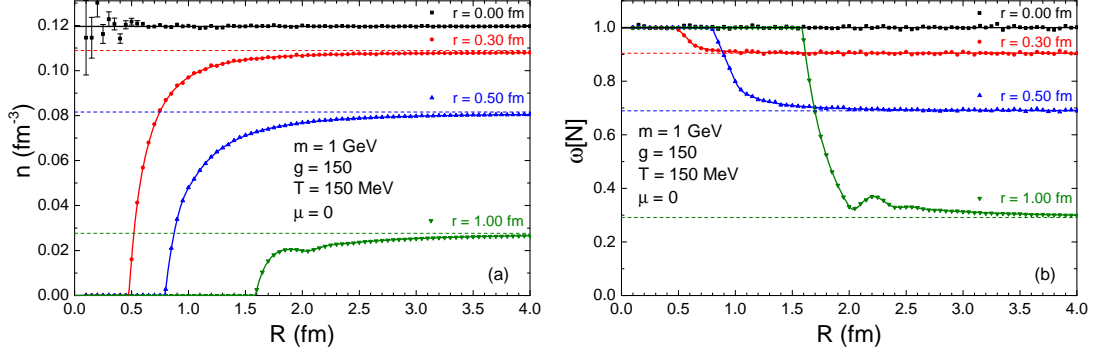
Figure 4.1:   (a) The GCE particle number density $n$ and (b) the scaled variance $\omega[N]$ as functions on the system radius $R$ for the EV model for particles of mass $m = 1$ GeV and degeneracy $g = 150$ at $T = 150$ MeV and $\mu = 0$. Dots show the MC results for four different values of the hard-core radius: $r = 0$, 0.3 fm, 0.5 fm, and 1 fm. Dashed horizontal lines show the values of the particle density (a) and scaled variance (b) calculated in the thermodynamic limit from Eqs. (2.10) and (4.4), respectively. Solid lines show the analytic results obtained by a direct summation of the GCE partition function.

as the following

$$\langle f(N) \rangle = \frac{\displaystyle\sum_{N=0}^{\lfloor V/v \rfloor} f(N)\, Z_{\mathrm{EV}}(T, V, N)}{\displaystyle\sum_{N=0}^{\lfloor V/v \rfloor} Z_{\mathrm{EV}}(T, V, N)}. \qquad (4.26)$$

Such a calculation was performed in order to cross-check the MC results. The results of these analytic calculations are shown in Fig. 4.1 by solid lines and they are fully consistent with the MC results. Note that a calculation of a direct sum over all states in the grand canonical partition function becomes numerically intractable in the multi-component gas with a large number of components. The MC procedure, on the other hand, does not suffer from such a complication.

As seen from Fig. 4.1a, both analytical and MC calculations show a presence of a small region where particle number density locally decreases with an increase of the system volume for $r = 1$ fm. More pronounced presence of such region(s) was also verified for larger values of particle radius parameter $r$. This result seems counterintuitive. Recall, however, that particle number density is given as

the ratio $n \equiv \langle N \rangle / V$. The number of terms $N_{\text{tot}} = \lfloor V/v \rfloor$ in Eq. (4.26), which is used to calculate $\langle N \rangle$, is finite. The $N_{\text{tot}}$ increases by one once the ratio $V/v$ reaches the next integer number. However, until that happens, the $N_{\text{tot}}$ value is fixed and this severely limits the growth of $\langle N \rangle$ with $V$. For this reason, the ratio $n = \langle N \rangle / V$ can locally be a decreasing function of $V$. The same mechanism is responsible for appearance of non-monotonous regions in the $V$-dependence of the scaled variance, seen in Fig. 4.1b.

### 4.4.2 Simultaneous effects of exact charge conservation and excluded-volume

In order to study the EV effects in the CE we consider a two-component system of particles and antiparticles. The degeneracy factor of $g_{\pm} = 75$, particle mass of $m_{\pm} = 1$ GeV, zero net charge, $Q = N_+ - N_- = 0$, and the system temperature $T = 150$ MeV are employed. Using the MC method we calculate the system-size dependence of the (anti)particle number density $n_{\pm}$ and the scaled variance $\omega[N_{\pm}]$. The MC CE and GCE results for four different values of the hard-core particle radius are shown in Fig. 4.2.

The MC results for $n_{\pm}$ and $\omega[N_{\pm}]$ at $r = 0$ can be directly compared to the analytical results for the ideal gas obtained in Ref. [108]. Our MC calculations are fully consistent with these analytical results (shown by black solid lines). In particular, $\omega[N_{\pm}] = 1/2$ at $R \to \infty$.

The analytic results for $r > 0$, obtained from a direct summation of the partition function, are also shown in Fig. 4.2 by colored solid lines. They are fully consistent with the MC results. The presence of the CE effects due to the exact charge conservation leads to further suppression of $n_{\pm}$ at finite $R$, in addition to the suppression due to the EV effects. The same is generally true for $\omega[N_{\pm}]$. There is, however, one important difference. The CE suppression effects for $n_{\pm}$ disappear in the thermodynamic limit $R \to \infty$, whereas both the CE and EV suppressions of $\omega[N_{\pm}]$ survive. Particularly, at $R \to \infty$ the CE values of $\omega[N_{\pm}]$ shown in Fig. 4.2b are smaller at $r > 0$ than the ideal gas CE value of $1/2$. At $R \to \infty$, the CE values of $\omega[N\pm]$ are also smaller than the corresponding GCE limiting values at the same $r$ shown in Fig. 4.1b.
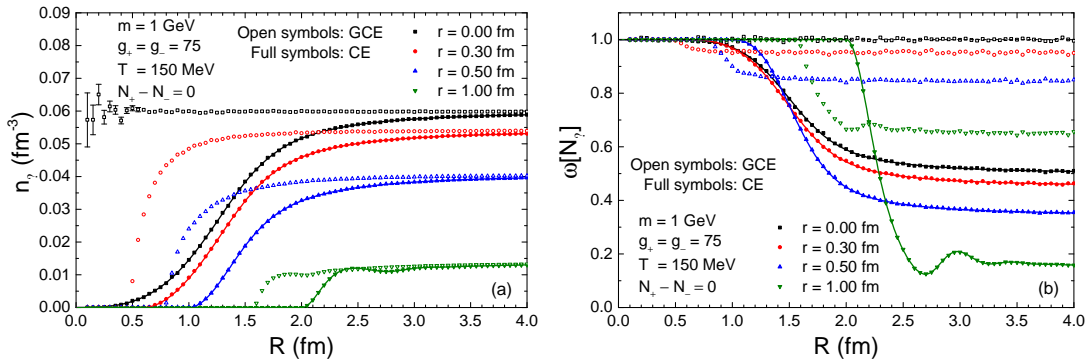
Figure 4.2: The MC results for (a) $n_\pm$ and (b) $\omega[N_\pm]$ as functions of $R$. The MC calculations are performed at $m = 1$ GeV, $g_\pm = 75$, $T = 150$ MeV, and $Q \equiv N_+ = N_- = 0$. Open symbols show the MC results in the GCE and full symbols in the CE for four different values of hard-core radius: $r = 0$, 0.3 fm, 0.5 fm, and 1 fm. Solid lines show the analytic results obtained by a direct summation of the partition function. The lines for $r = 0$ coincide with values (a) $n_\pm$ and (b) $\omega[N_\pm]$ calculated analytically in Ref. [108].

It is seen from Fig. 4.2a that there is a minimum system volume, below which the particle number density is strictly zero, similar to the GCE case. However, this minimum volume is approximately twice larger in the CE as compared to the GCE. The reason is that no microstate with a single particle is permitted in the CE since that would violate the exact charge neutrality condition. The presence of an antiparticle for each particle is required.

### 4.4.3 Hadron number fluctuations in HRG

The MC formulation of the full HRG model can be used to describe the hadron yields and their fluctuations in the presence of both the EV interactions and the exact charge conservation effects.

To illustrate the role of both EV and exact charge conservation effects in HRG a system with zero conserved charges, $B = S = Q = 0$, will be considered at first. It may correspond to hadron states created in $p\bar{p}$ or $e^+e^-$ reactions. Three values of the hadron hard-core radius, $r = 0$ (ideal HRG), 0.3 fm, and 0.5 fm, same for all hadron species, are considered within the MC formulation of the multi-component EV HRG. Note that in the considered case the Diagonal and the Crossterms EV models are equivalent. In Fig. 4.3a the scaled variance $\omega[N_\pm]$ of the number
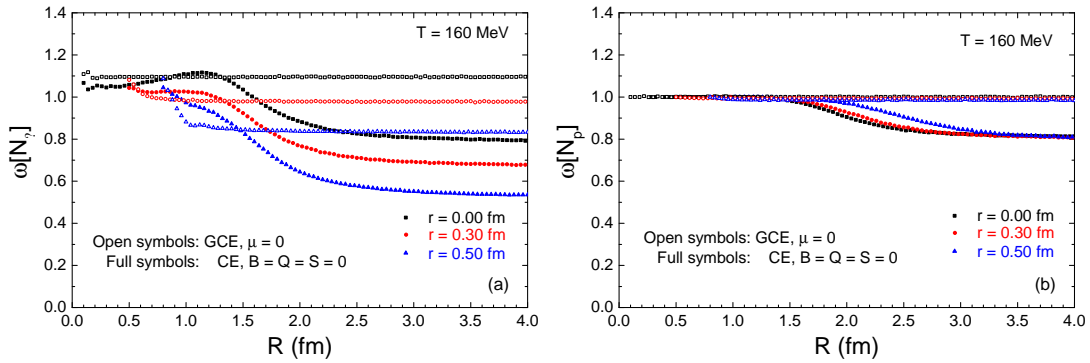
Figure 4.3: The MC results for $\omega[N_\pm]$ (a) and $\omega[N_p]$ (b) in full HRG at $T = 160$ MeV as functions of $R$. Open symbols show the MC results in the GCE with $\mu_B = \mu_Q = \mu_S = 0$ while full symbols depict the MC results in the CE for $p\bar{p}$-like systems ($B = Q = S = 0$). Three different values of hard-core radius are considered: $r = 0$, 0.3 fm and 0.5 fm.

of all positively or negatively charged hadrons in HRG is shown as a function of the system radius $R$. The system temperature is fixed at $T = 160$ MeV. In these calculations we additionally take into account contributions to $N_\pm$ from resonance decays. Thus, the MC procedure contains one additional step at the end: simulation of the chain of probabilistic decays of all resonances.

From Fig. 4.3a one observes that both EV and exact charge conservation effects suppress the $N_\pm$ fluctuations in the thermodynamical limit $R \to \infty$. For $r = 0.5$ fm the numerical values of both suppression effects are rather similar. At small $R$ the fluctuations are additionally sensitive to the finite size effects.

In Fig. 4.3b the scaled variance $\omega[N_p]$ for the fluctuations of the number of protons is shown as a function of the system radius $R$. In the considered example, the EV effects are defined by the total number $N_{\text{tot}}^{\text{prim}}$ of primary hadrons and resonances. The mean number of protons $\langle N_p \rangle$ is suppressed significantly by a presence of the excluded volume $v N_{\text{tot}}^{\text{prim}}$. However, as $\langle N_p \rangle$ is much smaller than $\langle N_{\text{tot}}^{\text{prim}} \rangle$, the fluctuations of $N_p$ have only a minor influence on the event-by-event values of the total excluded volume. For this reason the $N_p$ fluctuations do not deviate significantly from Poisson distribution due to the EV effects. This is not the case for the $N_\pm$ fluctuations, as $\langle N_\pm \rangle$ is comparable with $\langle N_{\text{tot}}^{\text{prim}} \rangle$. Note that the CE suppression effects for $\omega[N_p]$ survive in the thermodynamic limit $R \to \infty$, and they are not sensitive to the value of the hard-core radius $r$. The main source

of the CE suppression of $\omega[N_p]$ is the exact conservation of the net baryon number $B = 0$.

The role of EV effects on net proton fluctuations would be more pronounced if EV interactions were assumed to be present only between baryons. Such a study will be presented elsewhere.

### 4.4.4    Fit of hadron yields in $p + p$ collisions

The CE formulation of HRG can be used to describe the hadron yield data in collisions of small systems, such as (anti)proton-proton and $e^+ e^-$ collisions. Previously, only the non-interacting HRG was used in such studies [101, 102, 103, 104]. Here we will demonstrate the effect of the finite hadron eigenvolumes on chemical freeze-out parameters. For this purpose we analyze the hadron yield data of the NA61/SHINE Collaboration in inelastic proton-proton interactions at beam laboratory momentum $p_{\text{lab}}$ = 31, 40, 80, 158 GeV/$c$ [114, 115, 116]. The experimental data contains yields of $\pi^-$, $\pi^+$, $K^-$, $K^+$, and $\bar{p}$. These data were recently analyzed in Ref. [59] within the ideal HRG in the CE. It was found that the data can be reasonably well described with three chemical freeze-out parameters: temperature $T$, system radius (volume) $R$, and the strangeness undersaturation parameter $\gamma_S$.

To illustrate the effect of finite hadron eigenvolumes on chemical freeze-out parameters let us consider a simple case when all hadrons have the same hard-core radius $r$. Hadron densities become suppressed compared to the ideal gas. In the GCE, the suppression factor is the same for all hadron species. Thus, the extracted $T$ and $\gamma_S$ do not change. On the other hand, due to the suppression of the densities the total freeze-out volume will be larger compared to the ideal gas. It is also likely that eigenvolume corrections will not cancel out exactly within the CE formulation. Still, one expects the system volume to be affected most strongly. Thus, we fix $T$ and $\gamma_S$ to the values which were previously obtained within the ideal HRG model and only vary the system radius $R$. Three values of the hadron hard-core radius, $r = 0$, 0.3 fm, and 0.5 fm are considered in the MC calculations. The presence of the strangeness undersaturation is implemented by the substitution $z_i \to \gamma_S^{|s_i|} z_i$ in Eqs. (4.14) and (4.16), where $|s_i|$ is the sum
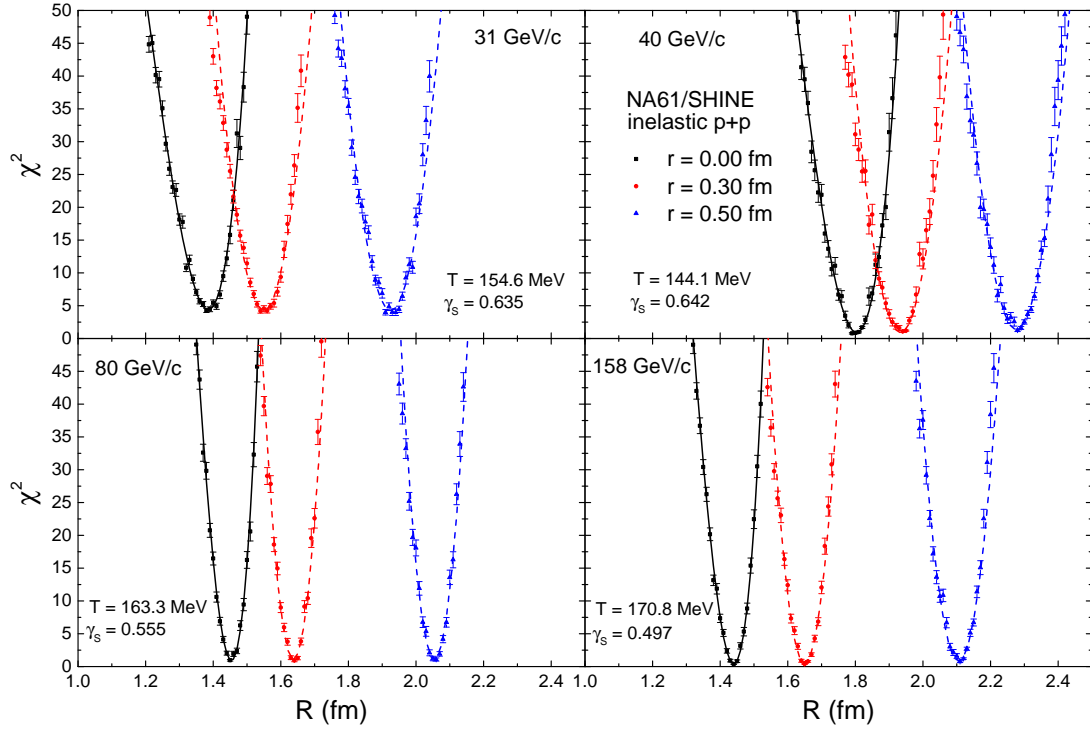
Figure 4.4: The dependence of the $\chi^2$ (4.28) of the HRG description of proton-proton hadron yield data of the NA61/SHINE Collaboration at $p_{\text{lab}} = 31, 40, 80$, and 158 GeV/$c$ [114, 115, 116] on the system radius $R$. The MC formulation of the eigenvolume HRG in CE is used. All hadrons are assumed to have the same hard-core radius of $r = 0$ (black symbols), 0.3 fm (red symbols), and 0.5 fm (blue symbols). The solid black lines show the results of the analytical calculation of the $\chi^2$ within the ideal HRG. The dashed lines depict the parabolic fits to the corresponding MC results in the vicinity of the $\chi^2$ minimum (see text). The parameters $T$ and $\gamma_S$ are fixed at each collision energy and are taken from the ideal HRG model fits performed in Ref. [59].

of strange quarks and antiquarks in hadron species $i$. Note that direct analytic calculation of the average hadron yields from the partition function is infeasible here due to a very large number of components in the full HRG. This is quite different from simple systems considered before.

The mean multiplicity $\langle N_i \rangle$ is calculated as the sum of the primordial mean multiplicity $\langle N_i^{\text{prim}} \rangle$ and resonance decay contributions as follows

$$\langle N_i \rangle = \langle N_i^{\text{prim}} \rangle + \sum_R \langle n_i \rangle_R \langle N_R^{\text{prim}} \rangle , \qquad (4.27)$$

Table 4.1: The values of $R$ and $\chi^2$ resulting from the parabolic fit of the Monte Carlo data in the vicinity of the minimum in the $R$-dependence of the $\chi^2$. The numbers in brackets correspond to the statistical uncertainty, determined in each case by the width of the parabola.

| $\sqrt{s}$ | R (fm) | | | $\chi^2$ | | |
|---|---|---|---|---|---|---|
| GeV | $r = 0$ fm | $r = 0.3$ fm | $r = 0.5$ fm | $r = 0$ fm | $r = 0.3$ fm | $r = 0.5$ fm |
| 7.7 | 1.38(1) | 1.55(1) | 1.93(1) | 4.75(30) | 4.27(22) | 4.23(36) |
| 8.8 | 1.80(1) | 1.93(1) | 2.28(1) | 0.88(11) | 0.79(14) | 1.36(16) |
| 12.3 | 1.45(1) | 1.64(1) | 2.05(1) | 1.06(12) | 1.01(26) | 1.00(24) |
| 17.3 | 1.44(1) | 1.65(1) | 2.11(1) | 0.34(6) | 0.41(9) | 0.73(15) |

which coincides with Eq. (3.2) used for analytic calculations in Chapter 3. In contrast to analytic calculations, however, the $\langle N_i^{\mathrm{prim}} \rangle$ and $\langle N_R^{\mathrm{prim}} \rangle$ are calculated by averaging over the sufficiently large number of the weighted events in the MC approach.

The quality of the data description is quantified by the $\chi^2$, defined as

$$\chi^2 = \sum_i \frac{(\langle N_i \rangle - N_i^{\mathrm{exp}})^2}{\sigma_i^{\mathrm{exp}}}, \tag{4.28}$$

where $i = \pi^+$, $\pi^-$, $K^+$, $K^-$, $\bar{p}$, the $\langle N_i^{\mathrm{exp}} \rangle$ and $\sigma_i^{\mathrm{exp}}$ are, respectively, the corresponding experimental yields and uncertainties, and $\langle N_i \rangle$ is the total yield of hadron species $i$ in the HRG model calculated with Eq. (4.27).

The MC results for the dependence of the $\chi^2$ on the total system radius (volume) $R$ are presented in Fig. 4.4. The results were obtained by generating $10^5$ weighted events for each configuration at each considered value of the system radius $R$. First, note that the MC results for ideal HRG ($r = 0$) are fully consistent with the corresponding analytic calculations depicted in Fig. 4.4 by solid black lines. The resulting values of the $\chi^2$ at the global minimum for ideal HRG case are close to those found in Ref. [59]. The MC results for the EV HRG model with $r = 0.3$ fm and 0.5 fm are depicted by red and blue symbols, respectively. The MC results for the $R$-dependence of the $\chi^2$ in the vicinity of the global minimum (defined as the region where $\chi^2 < 30$) are fitted by a parabolic function. This allows to estimate the value and position of the minimum. The fit results are depicted by dashed lines in Fig. 4.4.

The values of the $R$ and $\chi^2$ at the minima resulting from the MC analysis for the three considered cases are listed in Table 4.1. It is seen that the minimum values of $\chi^2$ for $r = 0.3$ and $r = 0.5$ fm are very similar to the ones at $r = 0$, i.e. no significant improvement or worsening of thermal fits is observed. The minima, however, are located at notably higher values of $R$ compared to the ideal HRG model. This looks very similar to GCE results where the EV corrections are canceled out in the ratios of yields. Note, however, that both the temperature $T$ and the $\gamma_S$ parameter were fixed and had the same values at all $R$. Thus, the $R$-dependencies of the $\chi^2$ shown in Fig. 4.4 should not be mistaken for the $\chi^2$ profiles of parameter $R$, as neither $T$ nor $\gamma_S$ were fitted at each distinct value of $R$. One should simultaneously fit all three parameters ($T$, $\gamma_S$, $R$) in order to make a stronger conclusion. Evidently, the $\chi^2$ profiles may show a wider minima. One can also try to check the EV models with different eigenvolumes for different hadron species. These extensions of the MC calculations will be considered elsewhere.

# Chapter 5

# Critical fluctuations in the classical van der Waals model

Event-by-event fluctuations in high energy nucleus-nucleus collisions are at present an actively used tool to study strongly interacting matter (see, e.g. Refs. [117, 118, 119]), especially for the search of the QCD critical point (CP) [120, 121]. In particular, the higher-order (non-Gaussian) fluctuation measures of conserved charges were suggested to be sensitive tools to investigate the QCD phase structure. Experimentally, the search for the CP is in progress: higher moments of net-proton and net-charge multiplicity were recently measured by the STAR collaboration in Au+Au collisions in the energy range $\sqrt{s_{\mathrm{NN}}} = 7.7 - 200$ GeV [122, 123, 124]. However, neither the existence nor the location of the QCD CP have been established.

In this chapter, critical fluctuations are studied in the simplest analytical model which contains a first-order phase transition with a critical point – the *van der Waals* equation. It is remarkable that no such study has been reported yet for this simple model. The content of this chapter follows the results published in Refs. [125, 126].

## 5.1   Classical van der Waals equation

The classical van der Waals (VDW) equation of state reads [51]

$$p(T, V, N) = \frac{TN}{V - bN} - a\left(\frac{N}{V}\right)^2, \tag{5.1}$$

where $a > 0$ and $b > 0$ are the VDW parameters which describe, respectively, the attractive and repulsive interactions between particles. The VDW equation (5.1) was formulated in 1873. van der Waals was awarded the 1910 Nobel Prize in Physics for this work. The first term in (5.1) describes the short-range repulsive interactions by means of the excluded-volume correction, whereby the system volume is substituted by the available volume, i.e. $V \to V - bN$. The second term describes the attractive interactions in the mean-field approximation, characterized by the attraction parameter $a$.

The VDW equation of state predicts a 1st order liquid-gas phase transition and exhibits a critical point. The thermodynamical quantities at the critical point are equal to [51]:

$$T_c = \frac{8a}{27b}, \qquad n_c = \frac{1}{3b}, \qquad p_c = \frac{a}{27b^2}. \tag{5.2}$$

The famous VDW isotherms and the corresponding phase diagram in the dimensionless reduced variables $\tilde{T} = T/T_c$, $\tilde{n} = n/n_c$, and $\tilde{p} = p/p_c$ are depicted in Fig. 5.1. To describe the phase coexistence region below the critical temperature the VDW isotherms should be corrected by the well-known Maxwell construction of equal areas. These corrected parts of the VDW isotherms are shown in Fig. 5.1a by the solid horizontal lines.

The canonical ensemble (CE) pressure in Eq. (5.1) is expressed as a function of temperature $T$, volume $V$, and particle number $N$. These variables, however, are *not* the natural variables for the pressure function, and, thus, Eq. (5.1) does *not* give the complete thermodynamic description of the system. The thermodynamical potential in the CE is the Helmholtz potential, dubbed the *free energy* $F(T, V, N)$. The function $F$ depends on its *natural variables*, temperature $T$, volume $V$, and number of particles $N$, and allows for a complete thermodynam-
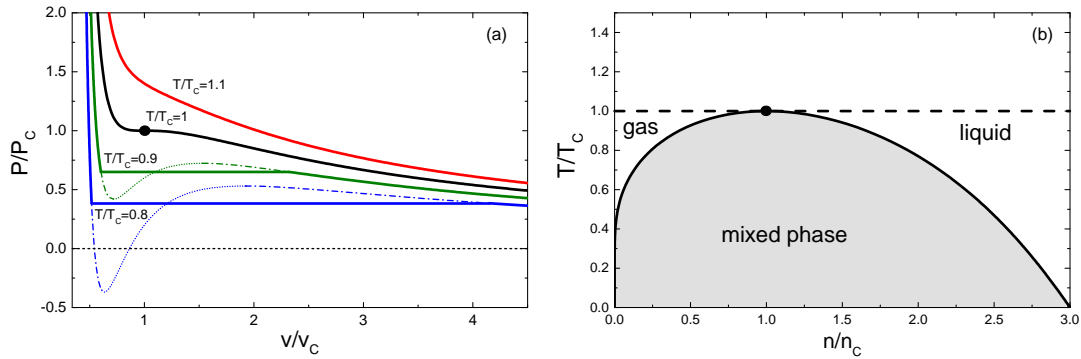
Figure 5.1: The pressure isotherms (a) and the temperature-density phase diagram (b) for the classical van der Waals equation depicted in the reduced variables.

ical description of all system properties. The free energy $F$ can be obtained by solving the following equation

$$\left(\frac{\partial F}{\partial V}\right)_{T,N} = -\,p(T, V, N) \,, \tag{5.3}$$

which for the classical van der Waals equation (5.1) yields (see [125] for details)

$$F(T, V, N) = F_{\mathrm{id}}(T, V - bN, N) \;-\; a\,\frac{N^2}{V} \,, \tag{5.4}$$

with $F_{\mathrm{id}}(T, V, N)$ being the free energy of the corresponding ideal Boltzmann gas:

$$F_{\mathrm{id}}(T, V, N) \;=\; -\,N\,T\left[1 \;+\; \ln\frac{d\,V\,m^2\,T\,K_2(m/T)}{2\pi^2\,N}\right] \,, \tag{5.5}$$

where $m$ is the mass of the particle, $d$ is its degeneracy factor (i.e., the number of internal states), and $K_2$ is the modified Bessel function of the second kind. Notably, the free energy (5.5) depends on parameters $m$ and $d$. These parameters are absent in the original VDW equation (5.1) for the CE pressure. This illustrates nicely the fact that the CE pressure $p(T, V, N)$ does not contain a complete information about the system, in contrast to the CE free energy $F(T, V, N)$ which does.

## 5.2   Grand canonical ensemble formulation

In this section, the GCE formulation of the classical VDW equation is described. Surprisingly, the GCE formulation appears to have been missing in the literature up to now, despite the almost 150 year old history of the VDW model. Does one really need the GCE formulation of the VDW model? There are at least three reasons for a positive answer to this question, particularly in regard to nuclear and hadronic physics applications.

First, the GCE pressure $p(T, \mu)$, as expressed in terms of its natural variables $T$ and $\mu$, gives a complete thermodynamic description of the systems, in contrast to the classical VDW equation (5.1) in the CE. Second, the number of hadrons of a given type is usually not conserved. For example, the number of pions cannot be considered as an independent variable and is a function of volume and temperature. The GCE formulation of the VDW equation is therefore an important step for inserting the repulsive and attractive VDW interactions into a fluid, i.e. into the HRG. Third, Eqs. (5.1) and (5.3) of the CE can not give answers with respect to the particle number fluctuations. Formally, the number of particles does not fluctuate in the CE: the total number of particles $N_0$ is constant in the full volume $V_0$. However, the number of particles $N$ starts to fluctuate if one considers a sub-system with $V < V_0$. If $V \ll V_0$, the $N$-fluctuations follow the GCE results.

The first step is to calculate the chemical potential

$$\mu \;=\; \left(\frac{\partial F}{\partial N}\right)_{V,T} \;=\; -T\,\ln\frac{(V-bN)\,\phi(T;d,m)}{N} \;+\; b\,\frac{NT}{V-bN} \;-\; 2a\,\frac{N}{V}\;. \quad (5.6)$$

From Eq. (5.6) one then obtains the following expression for the GCE particle number density $n(T, \mu)$:

$$\frac{N}{V} \;\equiv\; n(T,\mu) \;=\; \frac{n_{\mathrm{id}}(T,\mu^*)}{1\,+\,b\,n_{\mathrm{id}}(T,\mu^*)}\;, \qquad \mu^* \;=\; \mu \;-\; b\,\frac{n\,T}{1-b\,n} \;+\; 2an\;, \quad (5.7)$$

where $n_{\mathrm{id}}$ is the density of the ideal Maxwell-Boltzmann gas.

Equation (5.7) lies at the heart of the GCE formulation of the VDW equation. This is a transcendental equation for the particle density $n(T, \mu)$, which has to be

solved numerically for any given temperature $T$ and chemical potential $\mu$. The solution yields the GCE particle density $n(T, \mu)$ of the Maxwell-Boltzmann gas with VDW interactions.

The GCE pressure is calculated as

$$p(T, \mu) = \frac{T \, n(T, \mu)}{1 - b \, n(T, \mu)} - a[n(T, \mu)]^2. \tag{5.8}$$

The energy density of the VDW gas can be calculated within the GCE from the pressure function, $p(T, \mu)$,

$$\varepsilon(T, \mu) = T \left(\frac{\partial p}{\partial T}\right)_T + \mu \left(\frac{\partial p}{\partial \mu}\right)_\mu - p = \frac{\varepsilon_{\mathrm{id}}(T, \mu^*)}{1 + b \, n_{\mathrm{id}}(T, \mu^*)} - a \, n^2$$

$$= \Big[\bar{\epsilon}_{\mathrm{id}}(T; m) - a \, n\Big] n \,, \tag{5.9}$$

where $\mu^*$ is defined in Eq. (5.7) and where $\bar{\epsilon}_{\mathrm{id}}(T; m) = 3 \, T + m \frac{K_1(m/T)}{K_2(m/T)}$ is the average energy per particle in the ideal gas. A comparison of the right hand side of Eq. (5.9) with the corresponding ideal gas expression, $\varepsilon_{\mathrm{id}} = \bar{\epsilon}_{\mathrm{id}}(T; m) \, n_{\mathrm{id}}$, demonstrates the role of the parameters $a$ and $b$ for the system energy density. Both parameters $a$ and $b$ also influence the particle number density: $a > 0$ leads to an enhancement of the particle number density $n$ and $b > 0$ leads to its suppression. The parameter $b$ does not change the average energy per particle, whereas the mean field term $-a \, n$, proportional to the parameter $a$, is added to the average energy per particle, which changes it from $\bar{\epsilon}_{\mathrm{id}}$ to $\bar{\epsilon} = \bar{\epsilon}_{\mathrm{id}} - a \, n$.

## 5.3 Scaled variance of particle number fluctuations

### 5.3.1 Pure phases

The variance of the total particle number fluctuations in the GCE can be calculated as follows:

$$Var[N] \equiv \langle N^2 \rangle - \langle N \rangle^2 = T \left(\frac{\partial \langle N \rangle}{\partial \mu}\right)_{T,V} = T \, V \left(\frac{\partial n}{\partial \mu}\right)_T, \tag{5.10}$$
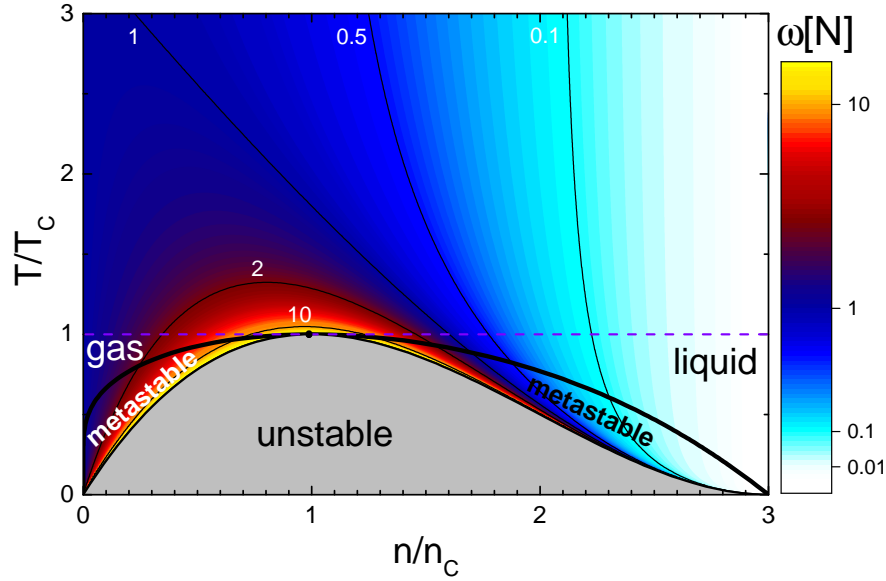
Figure 5.2: The scaled variance $\omega[N]$ (5.12) calculated from the VDW equation for the pure phases in the reduced $(T/T_c, n/n_c)$ coordinates.

where the symbol $\langle...\rangle$ denotes the GCE averaging, and $n(T, \mu)$ is the particle number density in the GCE. The scaled variance of the particle number fluctuations is then given by:

$$\omega[N] \equiv \frac{Var[N]}{\langle N \rangle} = \frac{T}{n}\left(\frac{\partial n}{\partial \mu}\right)_T . \tag{5.11}$$

The quantity $\left(\frac{\partial n}{\partial \mu}\right)_T$ can be obtained by taking the derivative of Eq. (5.7) with respect to $\mu$ and then solving the resulting equation for this quantity. The following simple expression for $\omega[N]$ is obtained

$$\omega[N] = \left[\frac{1}{(1 - bn)^2} - \frac{2an}{T}\right]^{-1} . \tag{5.12}$$

Formula (5.12) elucidates the different roles of the attractive and the repulsive interactions for particle number fluctuations: the repulsive interactions lead to the suppression of fluctuations, the attractive interactions lead to their enhancement, and the non-trivial interplay between these two leads to the divergence of fluctuations at the critical point.

The scaled variance $\omega[N]$ of the particle number fluctuations in pure phases

is shown in Fig. 5.2 in the reduced $(T/T_c, n/n_c)$ coordinates. At any fixed value of $T$, the particle number fluctuations (5.12) approach those of the ideal gas in the limit of small densities, i.e. $\omega[N] \cong 1$, at $n \to 0$. The fluctuations become small, $\omega[N] \ll 1$, in the opposite limit, at $n \to 1/b$. The scaled variance (5.12) is always positive for all possible values of $n$ and $T$ outside of the mixed phase region, as it should be. At the critical point ($T = T_c$, $n = n_c$) the scaled variance of the particle number fluctuations in GCE diverges.

Relation (5.12) is valid for all pure phases. This also includes the so-called metastable phases of super-heated liquid and super-cooled gas. These states are depicted by the dash-dotted lines on the VDW isotherms in Fig. 5.1a. In metastable phases the system is assumed to be uniform and, therefore, one can use Eq. (5.12) to calculate particle number fluctuations in these phases. It is seen from Fig. 5.2 that the scaled variance remains finite, and diverges only at the boundary between the metastable and unstable regions. We recall that at this boundary $\partial p/\partial n = 0$, where $p$ is the CE pressure (5.1). One can easily show using Eqs. (5.1) and (5.11) that $\omega[N] \to \infty$ when $\partial p/\partial n = 0$. Note that the thermodynamical relations are not fulfilled in the unstable region where $\partial p/\partial n < 0$. Nonphysical behavior with $\omega[N] < 0$ is found in this region.

## 5.3.2 Mixed phase

Relation (5.12) is valid for pure phases, but not for the mixed phase region. In the mixed phase the volume of the system as a whole is divided into two parts, one occupied by the gaseous phase and one by the liquid phase. Therefore, in this case one has to take into account also the corresponding fluctuations in the volume fractions.

Let us consider a point $(n, T)$ inside the mixed phase. The volume $V$ is then divided into the two parts, $V_g = \xi V$ occupied by the gaseous phase with particle number density $n_g$ and $V_l = (1 - \xi)V$ occupied by the liquid phase with particle number density $n_l$. The total number of particles $N$ equals to $N_g + N_l$. The

average value and scaled variance for the $N$-distribution are

$$\langle N \rangle = \langle N_g \rangle + \langle N_l \rangle = V \left[ \xi n_g + (1 - \xi) n_l \right] , \tag{5.13}$$

$$\omega[N] = \frac{\langle N^2 \rangle - \langle N \rangle^2}{\langle N \rangle}$$

$$= \frac{\langle N_g^2 \rangle - \langle N_g \rangle^2}{\langle N \rangle} + \frac{\langle N_l^2 \rangle - \langle N_l \rangle^2}{\langle N \rangle} + 2 \frac{\left[ \langle N_g N_l \rangle - \langle N_g \rangle \langle N_l \rangle \right]}{\langle N \rangle} . \tag{5.14}$$

In calculating the variations of $N_g$ and $N_l$ distributions inside the the mixed phase, one should take into account the fluctuations of the corresponding volumes $V_g = \xi V$ and $V_l = (1 - \xi) V$. In fact, these are the fluctuations of the parameter $\xi$. In the thermodynamic limit $V \to \infty$, one finds:

$$\frac{\langle N_g^2 \rangle - \langle N_g \rangle^2}{\langle N \rangle} = \frac{\langle N_g \rangle}{\langle N \rangle} \omega_\xi[N_g] + \frac{n_g^2}{n} V \left[ \langle \xi^2 \rangle - \langle \xi \rangle^2 \right] , \tag{5.15}$$

$$\frac{\langle N_l^2 \rangle - \langle N_l \rangle^2}{\langle N \rangle} = \frac{\langle N_g \rangle}{\langle N \rangle} \omega_\xi[N_l] + \frac{n_l^2}{n} V \left[ \langle \xi^2 \rangle - \langle \xi \rangle^2 \right] , \tag{5.16}$$

$$\frac{\langle N_g N_l \rangle - \langle N_g \rangle \langle N_l \rangle}{\langle N \rangle} = - 2 \frac{n_g n_l}{n} V \left[ \langle \xi^2 \rangle - \langle \xi \rangle^2 \right] , \tag{5.17}$$

where $\omega_\xi[N_g]$ and $\omega_\xi[N_l]$ in Eqs. (5.15) and (5.16) correspond to the fixed value of $\xi$, and can be calculated using Eqs. (5.10) and (5.11). One finds

$$\omega[N] = \frac{\xi_0 n_g}{n} \left[ \frac{1}{(1 - b n_g)^2} - \frac{2 a n_g}{T} \right]^{-1} + \frac{(1 - \xi_0) n_l}{n} \left[ \frac{1}{(1 - b n_l)^2} - \frac{2 a n_l}{T} \right]^{-1}$$

$$+ \frac{(n_g - n_l)^2 V}{n} \left[ \langle \xi^2 \rangle - \langle \xi \rangle^2 \right] , \tag{5.18}$$

where the equilibrium value $\langle \xi \rangle \equiv \xi_0$ is

$$\xi_0 = \frac{n_l - n}{n_l - n_g} . \tag{5.19}$$

To calculate the variance $\langle \xi^2 \rangle - \langle \xi \rangle^2$ in Eq. (5.18) we can return to the CE formulation. The free energy of the system can be presented as

$$F(V, T, N; \xi) = F(\xi V, T, N_g) + F[(1 - \xi) V, T, N_l] , \tag{5.20}$$

where the surface free energy is neglected in the thermodynamic limit $V \to \infty$. Note also that in the in the thermodynamic limit the particle number densities $n_g$ and $n_l$ in the GCE are identical to their CE values as a consequence of thermodynamic equivalence. The probability distribution $W(\xi)$ is proportional to $\exp[-F(V,T,N;\xi)/T]$. The function $F$ is given by Eq. (5.20). It can be presented as a power series expansion over $\xi - \xi_0$ in a vicinity of the equilibrium value $\xi_0$. This gives the normalized probability distribution ($C$ is a normalization factor) for $\xi$ in the form

$$W(\xi) = C \, \exp\left[-\frac{1}{2T}\left(\frac{\partial^2 F}{\partial \xi^2}\right)_{\xi=\xi_0}(\xi - \xi_0)^2\right] \equiv C \, \exp\left[-\frac{(\xi - \xi_0)^2}{2\sigma^2}\right],$$

(5.21)

where

$$\sigma^2 = T\left(\frac{\partial^2 F}{\partial \xi^2}\right)^{-1}_{\xi=\xi_0} = -\frac{T}{V^2}\left[\left(\frac{\partial p_g}{\partial V_g}\right) + \left(\frac{\partial p_l}{\partial V_l}\right)\right]^{-1}$$

$$= \frac{T}{V}\left[\frac{n_g T}{\xi_0 (1 - bn_g)^2} - \frac{2an_g^2}{\xi_0} + \frac{n_l T}{(1 - \xi_0)(1 - bn_l)^2} - \frac{2an_l^2}{1 - \xi_0}\right]^{-1}$$

(5.22)

Using the $\xi$-distribution (5.21) one finds

$$\langle \xi^2 \rangle - \langle \xi \rangle^2 = \sigma^2$$

(5.23)

and finally,

$$\omega[N] = \frac{\xi_0 n_g}{n}\left[\frac{1}{(1 - bn_g)^2} - \frac{2an_g}{T}\right]^{-1} + \frac{(1 - \xi_0)n_l}{n}\left[\frac{1}{(1 - bn_l)^2} - \frac{2an_l}{T}\right]^{-1}$$

$$+ \frac{(n_g - n_l)^2}{n}\left[\frac{n_g}{\xi_0(1 - bn_g)^2} - \frac{2an_g^2}{\xi_0 T} + \frac{n_l}{(1 - \xi_0)(1 - bn_l)^2} - \frac{2an_l^2}{(1 - \xi_0)T}\right]^{-1}.$$

(5.24)

The scaled variance $\omega[N]$ of the particle number fluctuations is shown in Fig. 5.3 in all regions of the phase diagram in the reduced $(T/T_c, n/n_c)$ coordinates, both inside and outside the mixed phase region. It is interesting to compare Eq. (5.24) for the scaled variance calculated inside the mixed phase
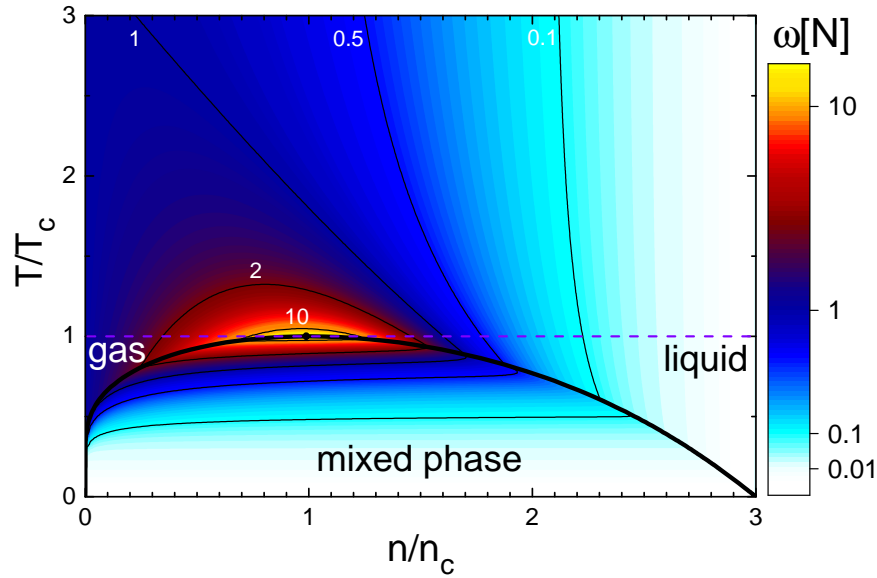
Figure 5.3:   The density plot of the scaled variance $\omega[N]$ of the particle number fluctuations shown in all regions on the phase diagram, both inside and outside the mixed phase region.

with Eq. (5.12) outside the mixed phase. These two equations do yield the same result at phase boundaries. At the boundary between the gaseous and mixed phase (i.e., $\xi_0 = 1$) both the second and third terms in the right hand side of Eq. (5.24) become equal to zero, and the first term in (5.24) coincides with Eq. (5.12). Similarly, at the boundary between the liquid and mixed phase (i.e., $\xi_0 = 0$) both the first and third terms in the right hand side of Eq. (5.24) become equal to zero, and the second term in (5.24) coincides with Eq. (5.12). It might seem from Fig. 5.3 that at small temperatures fluctuations have a discontinuity at the boundary between the liquid and mixed phase. This is, however, not the case: as mentioned above, when approaching the boundary from inside the mixed phase ($\xi_0 \to 0$), the third term in the r.h.s. of Eq. (5.24) vanishes, but at small temperatures it vanishes rapidly and only in the very vicinity of the phase boundary. As a consequence, this behavior is seen poorly on the scale used in Fig. 5.3.

## 5.4   Non-Gaussian fluctuations

The scaled variance $\omega[N]$ is the second-order measure of the particle number distribution. The $\omega[N]$ characterizes the width of the distribution. The higher-order non-Gaussian measures, such as the skewness $S\sigma$ and the kurtosis $\kappa\sigma^2$, can provide deeper information about the underlying particle number distribution. Recently, such measures for the conserved charges fluctuations have attracted much attention in the context of the search of the QCD critical point (see, e.g., Ref. [127] and [128]), and have been performed in various effective QCD models [129, 130, 131].

The skewness $S\sigma$ is defined as

$$ S\sigma \;=\; \frac{\langle (\Delta N)^3 \rangle}{\sigma^2} \;, \tag{5.25} $$

where $(\Delta N)^3$ is the third central moment about the mean of the $N$-distribution. The skewness is a measure of the degree of asymmetry of the distribution $\mathcal{P}(N)$ around its mean value $\langle N \rangle$. Positive skewness indicates a distribution with an asymmetric tail extending more to the *right*, i.e., toward $N$-values with $N > \langle N \rangle$. Negative skewness indicates a distribution with an asymmetric tail extending more to the *left*, i.e., toward $N$-values with $N < \langle N \rangle$. If the $\mathcal{P}(N)$ distribution is symmetric around its mean value, i.e., the *right* and *left* tails are equal, it has zero skewness. This is the case for the normal Gaussian distribution, whereas the Poisson distribution shows a positive value of the skewness, $S\sigma = 1$.

The (excess) kurtosis $\kappa\sigma^2$ is a measure of the "peakedness" of the probability distribution $\mathcal{P}(N)$,

$$ \kappa\sigma^2 \;=\; \frac{\langle (\Delta N)^4 \rangle \;-\; 3\,\langle (\Delta N)^2 \rangle^2}{\sigma^2} \;. \tag{5.26} $$

The kurtosis (5.26) measures the degree to which a distribution is more (or less) peaked than a normal Gaussian distribution. Positive kurtosis indicates a relatively peaked (leptokurtic) distribution. Negative kurtosis indicates a relatively flat (platykurtic) distribution. The Poisson distribution has a positive value of the kurtosis, $\kappa\sigma^2 = 1$.

The normal Gaussian distribution corresponds to the zero value of both the skewness (5.25) and the (excess) kurtosis (5.26). Therefore, (strong) deviations of $S\sigma$ and/or $\kappa\sigma^2$ from zero are signatures of a (highly) non-Gaussian shape of the particle number distribution.

The particle number fluctuations in the GCE can be characterized by the following dimensionless cumulants (susceptibilities),

$$\chi_n = \frac{\partial^n (p/T^4)}{\partial(\mu/T)^n} \, , \tag{5.27}$$

which are directly connected to the moments of the particle number distribution by

$$\chi_1 = \frac{\langle N \rangle}{VT^3} \, , \quad \chi_2 = \frac{\langle (\Delta N)^2 \rangle}{VT^3} \, , \quad \chi_3 = \frac{\langle (\Delta N)^3 \rangle}{VT^3} \, , \quad \chi_4 = \frac{\langle (\Delta N)^4 \rangle - 3\langle (\Delta N)^2 \rangle^2}{VT^3} \, . \tag{5.28}$$

The skewness (5.25) and the kurtosis (5.26) are intensive fluctuation measures which remain finite in the thermodynamic limit $V \to \infty$. They can be expressed in terms of the susceptibilities as

$$S\sigma = \chi_3/\chi_2 \qquad \text{and} \qquad \kappa\sigma^2 = \chi_4/\chi_2.$$

The calculation of the skewness in the VDW model yields

$$S\sigma = \frac{\chi_3}{\chi_2} = \omega[N] + \frac{T}{\omega[N]} \left( \frac{\partial \omega[N]}{\partial \mu} \right)_T = (\omega[N])^2 \left[ \frac{1 - 3bn}{(1 - bn)^3} \right] \, . \tag{5.29}$$

Non-Gaussian fluctuations for the VDW equation of state are considered here only in pure phases, for simplicity. The skewness $S\sigma$ is plotted in Fig. 5.4 as a function of the reduced temperature and density, for both stable and metastable pure phases. The skewness is positive at $n/n_c < 1$ (the gaseous phase), negative at $n/n_c > 1$ (the liquid phase), and $S\sigma = 0$ at $n = n_c$, as clearly seen from Eq. (5.29). Above relations are valid both for all temperatures, i.e. both above ($T > T_c$) and below ($T < T_c$) the critical temperature. At vanishing density, $n \to 0$, the skewness goes to unity, $S\sigma \to 1$. This small asymmetry of the particle number distribution corresponds to the Poisson distribution of the ideal
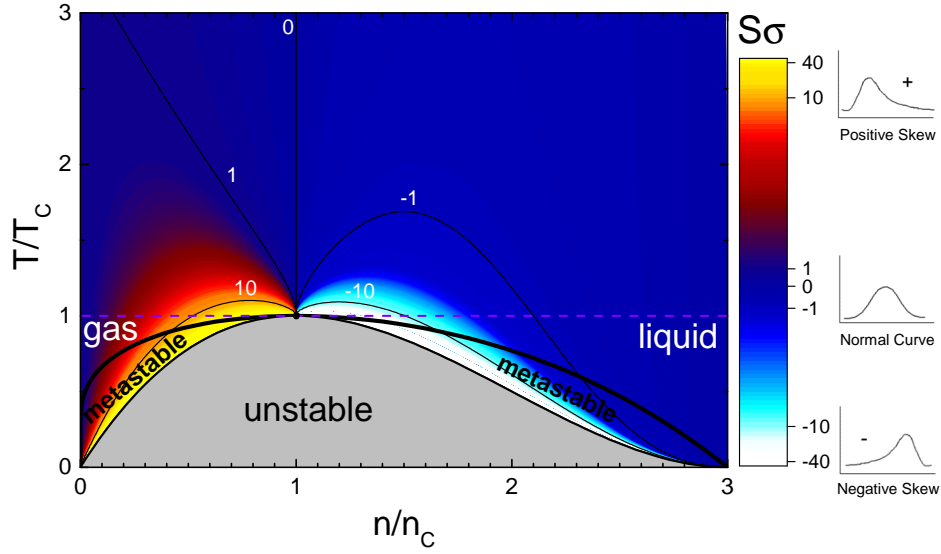
Figure 5.4: The skewness $S\sigma$ (5.29) calculated from the VDW equation for the pure phases in the reduced $(T/T_c, n/n_c)$ coordinates.

Boltzmann gas. On the other hand, the $S\sigma$ diverges at the critical point, and its sign depends on the path of approach to the CP.

The kurtosis $\kappa\sigma^2$ is:

$$\kappa\sigma^2 \ = \ \frac{\chi_4}{\chi_2} \ = \ (S\sigma)^2 + T\left(\frac{\partial[S\sigma]}{\partial\mu}\right)_T$$
$$= \ 3\,(S\sigma)^2 - 2\,\omega[N]\,S\sigma - 6\,(\omega[N])^3\,\frac{b^2 n^2}{(1-bn)^4} \ . \qquad (5.30)$$

The kurtosis $\kappa\sigma^2$ is plotted in Fig. 5.5 as a function of the reduced temperature and density, for both stable and metastable pure phases. The kurtosis is positive (leptokurtic) at at $T < T_c$ for both $n < n_c$ (the gaseous phase) and $n > n_c$ (the liquid phase). The kurtosis attains large negative values (platykurtic) at the critical density $n = n_c$ and temperatures just above the critical, $T > T_c$. This indicates that particle number distribution has a rather flat maximum in that region, much flatter than the corresponding Gaussian peak with the same width. This region can be identified with the crossover region, where a rather rapid, but smooth transition between gaseous and liquid phases takes place.

The dependencies of the skewness $S\sigma$ and of the kurtosis $\kappa\sigma^2$ on the reduced temperature and density are universal for any classical Maxwell-Boltzmann gas
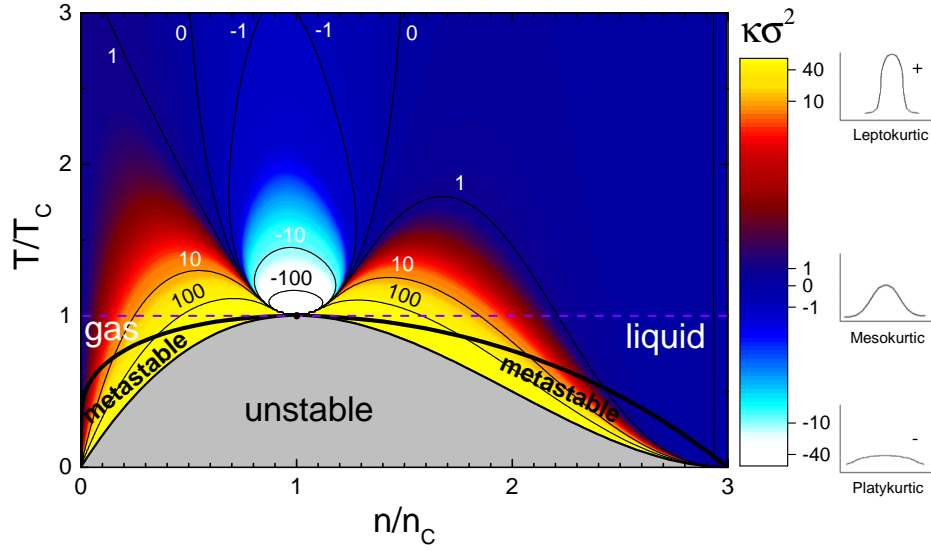
Figure 5.5:   The kurtosis $\kappa\sigma^2$ (5.30) calculated from the VDW equation for the pure phases in the reduced $(T/T_c, n/n_c)$ coordinates.

with VDW interactions. The same is true for the scaled variance $\omega[N]$. Thus, these results apply for any system described by the classical VDW equation: atoms, molecules, etc. However, this universality is lost if quantum statistical effects are non-negligible, as will be detailed in the next chapter.

## 5.5    Strongly intensive quantities

The obtained results demonstrate strong increase of the particle number fluctuations in vicinity of the CP. The fluctuations may become also very large for metastable states, i.e., super-cooled gas and/or super-heated liquid. These fluctuation signals from phase transitions in the nuclear matter can be observed in the event-by-event analysis of heavy ion collisions. However, in these processes there is one more source of particle number fluctuations: the event-by-event fluctuations of the system volume. These volume fluctuations are mainly of the geometrical origin, and they cannot be avoided in nucleus-nucleus reactions. Thus, one may observe large experimental fluctuations even in simplest scenarios, e.g., in the ideal gas scenario.

The strongly intensive measures of the fluctuations defined in terms of two

extensive quantities $A$ and $B$ were suggested in Ref. [132] to alleviate these problems. These measures are independent of the system volume and its fluctuations in GCE statistical systems which do not contain phase transitions. Note, however, that in systems with the CP (in general, for the 2nd order phase transitions) the critical behavior does depend on the system volume and shows the characteristic finite-size scaling. This implies that strongly intensive quantities are also volume-dependent near the CP. Thus, using the strongly intensive measures one excludes trivial volume fluctuations for normal statistical systems, and a presence of large fluctuations in terms of these measures can be considered as an indication of the critical behavior.

The strongly intensive measures are presently being used in the search for critical behavior of strongly interacting matter in heavy-ion collision experiments at the CERN Super Proton Synchrotron [121, 133, 134, 135, 136]. It is believed that they exhibit critical behavior and their measurement may provide evidence of the existence of the QCD CP. At the same time, no model calculation which would confirm the existence of such critical behavior has been performed to date.

In the present thesis the strongly intensive measures of total energy $E$ and particle number $N$ fluctuations for the VDW equation of state are considered. They are defined as

$$\Delta[E, N] \;=\; C_\Delta^{-1}\Big[\langle N\rangle \omega[E] - \langle E\rangle \omega[N]\Big] \,, \tag{5.31}$$

$$\Sigma[E, N] \;=\; C_\Sigma^{-1}\Big[\langle N\rangle \omega[E] + \langle E\rangle \omega[N] - 2\Big(\langle EN\rangle - \langle E\rangle \langle N\rangle\Big)\Big] \,, \tag{5.32}$$

where $C_\Delta^{-1}$ and $C_\Sigma^{-1}$ are the normalization factors that have been suggested in the following form [137]

$$C_\Delta \;=\; C_\Sigma \;=\; \langle N\rangle\, \omega[\varepsilon] \,, \tag{5.33}$$

with $\omega[\varepsilon]$ being the scaled variance of a single-particle energy distribution in the VDW system. It is necessary to calculate $\omega[\varepsilon]$, $\omega[E]$, and $\langle EN\rangle$ to proceed.

In the VDW gas the average single-particle energy $\overline{\epsilon}$ is independent of the

parameter $b$, but it is modified due to a presence of the attractive mean field:

$$\bar{\epsilon} = \bar{\epsilon}_{\text{id}}(T) - a\frac{N}{V} \;=\; 3\,T + m\frac{K_1(m/T)}{K_2(m/T)} \;-\; a\,n\;, \tag{5.34}$$

where $\bar{\epsilon}_{\text{id}}$ is the average single-particle energy in the relativistic ideal gas. The variance of the single-particle energy is insensitive to the presence of the VDW mean field, and one obtains

$$\omega[\epsilon] \;=\; \frac{\overline{\epsilon^2} - \bar{\epsilon}^2}{\bar{\epsilon}} \;=\; \frac{T^2}{\bar{\epsilon}}\,\frac{\partial\,\bar{\epsilon}_{\text{id}}}{\partial T}\;. \tag{5.35}$$

The mean total energy is

$$\langle E \rangle \;=\; \left\langle \left( \bar{\epsilon}_{\text{id}} - a\frac{N}{V} \right) N \right\rangle$$

$$=\; \bar{\epsilon}_{\text{id}}\,\langle N \rangle - \frac{a}{V}\,\langle N^2 \rangle = \bar{\epsilon}_{\text{id}}\,\langle N \rangle - \frac{a}{V}\,\langle N \rangle^2 - a\,\frac{\langle N^2 \rangle - \langle N \rangle^2}{V}\;. \tag{5.36}$$

The first and second terms in the right hand side of Eq. (5.36) are proportional to $\langle N \rangle$. On the other hand, the third term remains finite outside the critical point in the thermodynamic limit $V \to \infty$. Therefore, one obtains

$$\langle E \rangle \;\cong\; \left( \bar{\epsilon}_{\text{id}} - an \right) \langle N \rangle\;. \tag{5.37}$$

For $\omega[E]$ one then finds

$$\omega[E] \equiv \frac{\langle E^2 \rangle - \langle E \rangle^2}{\langle E \rangle} = \frac{1}{\langle E \rangle}\,T^2\left( \frac{\partial \langle E \rangle}{\partial T} \right)_{\mu/T} = \omega[\epsilon] + \frac{(\bar{\epsilon}_{\text{id}} - 2an)^2}{\bar{\epsilon}_{\text{id}} - an}\,\omega[N]\;. \tag{5.38}$$

Finally, the correlations between $E$ and $N$ can be calculated as the following

$$\langle EN \rangle - \langle E \rangle \langle N \rangle \;=\; T^2\left( \frac{\partial \langle N \rangle}{\partial T} \right)_{\mu/T} = \left( \bar{\epsilon}_{\text{id}} - 2an \right) \langle N \rangle\,\omega[N]\;. \tag{5.39}$$

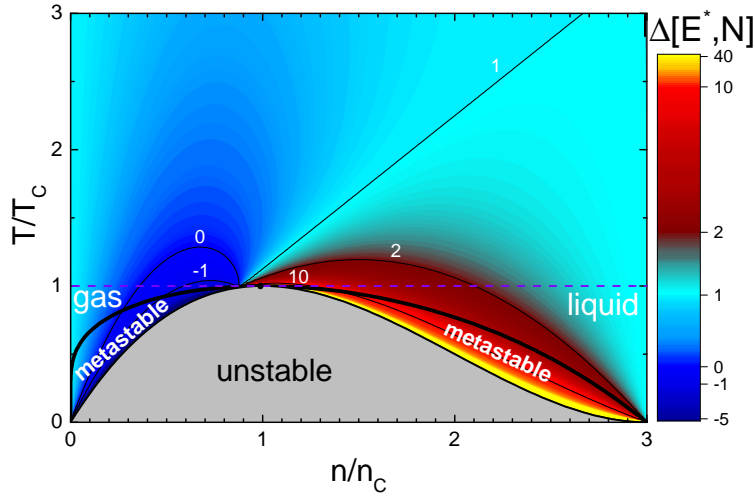Substituting the above relations into Eqs. (5.31) and (5.32) one finds the fol-

Figure 5.6: The strongly intensive measure $\Delta[E^*, N]$ (5.42) of excitation energy and particle number fluctuations calculated from the VDW equation in the nonrelativistic limit for the pure phases in the reduced $(T/T_c, n/n_c)$ coordinates. Several lines of constant values of $\Delta[E^*, N]$ are shown.

lowing expressions for the strongly intensive quantities:

$$\Delta[E, N] = 1 - \frac{an(2\bar{\epsilon}_{\rm id} - 3an)}{\overline{\epsilon_{\rm id}^2} - \bar{\epsilon}_{\rm id}^2} \, \omega[N], \tag{5.40}$$

$$\Sigma[E, N] = 1 + \frac{a^2 n^2}{\overline{\epsilon_{\rm id}^2} - \bar{\epsilon}_{\rm id}^2} \, \omega[N] \, . \tag{5.41}$$

In the absence of the attractive interactions (i.e., $a = 0$), one can readily see from Eqs. (5.40) and (5.41) that $\Delta[E, N] = \Sigma[E, N] = 1$, thus, in the EV model the strongly intensive quantities are the same as in the ideal Boltzmann gas.

The expressions (5.40) and (5.41) for $\Delta[E, N]$ and $\Sigma[E, N]$ become more transparent if one subtracts the rest energy $m$ from the total energy, i.e. $E \rightarrow E^* = E - m \, N$, and then considers the non-relativistic limit, $\bar{\epsilon}_{\rm id} = 3T/2$ and $\overline{\epsilon_{\rm id}^2} - \bar{\epsilon}_{\rm id}^2 = 3T^2/2$. In this case only the kinetic energy fluctuations contribute to $\overline{\epsilon_{\rm id}^2}$. In the context of heavy-ion collision experiments the $E^*$ can be identified
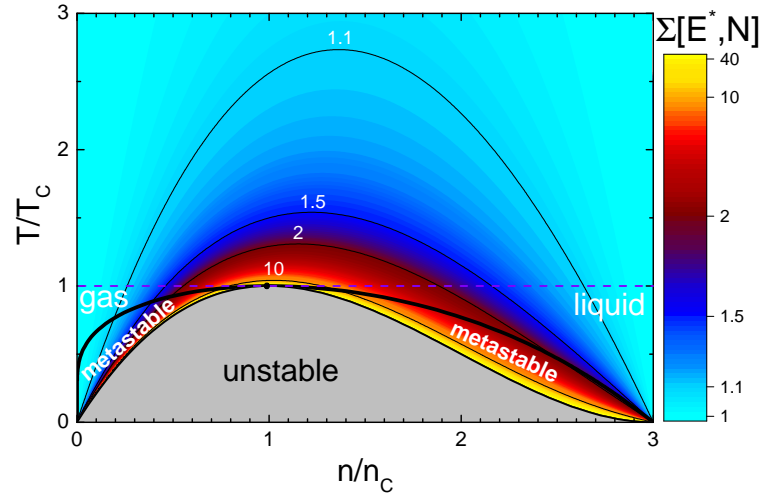
Figure 5.7:    The strongly intensive measure $\Sigma[E^*, N]$ (5.43) of excitation energy and particle number fluctuations calculated from the VDW equation in the nonrelativistic limit for the pure phases in the reduced $(T/T_c, n/n_c)$ coordinates. Several lines of constant values of $\Sigma[E^*, N]$ are shown.

with the total excitation energy. One obtains

$$\Delta[E^*, N] = 1 - \frac{2}{3} \frac{an(3T - 3an)}{T^2} \, \omega[N] \;=\; 1 \;-\; \frac{9\widetilde{n}}{4\widetilde{T}} \left[ 1 \;-\; \frac{9\widetilde{n}}{8\widetilde{T}} \right] \omega[N] \;, \quad (5.42)$$

$$\Sigma[E^*, N] = 1 + \frac{2}{3} \frac{a^2 n^2}{T^2} \, \omega[N] \;=\; 1 + \frac{27}{32} \frac{\widetilde{n}^2}{\widetilde{T}^2} \, \omega[N] \;. \quad (5.43)$$

The quantities $\Delta[E^*, N]$ and $\Sigma[E^*, N]$ are depicted in Figs. 5.6 and 5.7, respectively. Both the $\Sigma[E^*, N]$ and $\Delta[E^*, N]$ measures approach unity in both zero density, $n \to 0$, and packing, $n \to 1/b$, limits. They both diverge at the CP. The $\Sigma[E^*, N]$ measure is always positive and does not become smaller than unity, while the $\Delta[E^*, N]$ measure attains both positive and negative values.

These results, obtained within classical VDW equation, confirm that strongly intensive quantities do exhibit critical behavior. Thus, these measures are suitable in the search for the CP of strongly interacting matter in heavy-ion collision experiments.

# Chapter 6

# Quantum statistical van der Waals fluid

The Maxwell-Boltzmann VDW equation (5.1) is valid for classical systems, where the effects of quantum statistics are neglected. In this chapter a generalization of the VDW equation to include effects of the quantum statistics (Fermi-Dirac or Bose-Einstein) is described. We illustrate this new formalism by successfully treating the nuclear matter as a fermionic VDW system of nucleons. The content of this chapter follows Refs. [138, 139, 140]. Identical formulation derived with a different method was later obtained by other authors in Ref. [141].

## 6.1 van der Waals equation with quantum statistics

Proper treatment of quantum effects is crucially important for a description of statistical equilibrium at small temperatures and "non-small" densities. A good example is the nuclear matter. The ground state of nuclear matter is located at $T = 0$, and it cannot be described by the classical Maxwell-Boltzmann VDW fluid: Models which neglect the Fermi statistics exhibit clearly unphysical behavior in the zero temperature limit. For example, the entropy of the ideal Boltzmann gas becomes negative in this limit, contradicting the 3rd law of thermodynamics (see [138] for details). Thus, the classical VDW equation is inappropriate for

the nuclear matter description.

A quantum statistical generalization of the classical VDW model had not been developed previously. The same is true regarding the extension of the VDW theory to multi-component quantum statistical systems. These are important new steps, not only for applications in nuclear and hadronic physics, but also for numerous applications in condensed matter physics. Their impact on characterization of various properties of materials will be described elsewhere.

The free energy of the classical single-component VDW fluid is given by Eq. (5.4). It is *postulated* here to remain valid for quantum statistics, be it either Fermi-Dirac or Bose-Einstein distribution. This implies the following free energy of the quantum statistical VDW fluid:

$$F(T, V, N) = F_{\mathrm{id}}(T, V - bN, N) - a \frac{N^2}{V} \ , \qquad (6.1)$$

where $F_{\mathrm{id}}(T, V, N)$ is the free energy of the corresponding ideal *quantum* fluid. This modified VDW equation thus includes quantum statistics (see Ref. [140] for more details). The CE pressure reads

$$p(T, V, N) = -(\partial F/\partial V)_{T,N} = p_{\mathrm{id}}(T, V - bN, N) - a \frac{N^2}{V^2} \ , \qquad (6.2)$$

where $p_{\mathrm{id}}(T, V, N)$ is the CE pressure of the ideal *quantum* gas. For Maxwell-Boltzmann statistics $p_{\mathrm{id}}^{\mathrm{cl}}(T, V - bN, N) = NT/(V - bN)$, and in this case Eq. (6.2) coincides with the classical VDW equation (5.1). The total entropy $S = -(\partial F/\partial T)_{V,N}$ of the quantum statistical VDW fluid reads $S(T, V, N) = S_{\mathrm{id}}(T, V - bN, N)$. One can easily see that entropy is always positive and that $S \to 0$ with $T \to 0$, which respects the 3rd law of thermodynamics.

Equation (6.2) gives the pressure of the quantum statistical VDW model in the CE. To transform this quantum VDW equation to the GCE, the CE chemical potential is3 calculated as $\mu(T, V, N) = (\partial F/\partial N)_{T,V}$, and, denoting $\mu \equiv \mu(T, V, N)$ and $N/V \equiv n$, the resulting equation is solved to obtain the GCE particle density $n(T, \mu)$ [138]

$$n(T, \mu) = \frac{n_{\mathrm{id}}(T, \mu^*)}{1 + b \, n_{\mathrm{id}}(T, \mu^*)}, \qquad (6.3)$$

where $\mu^* = \mu - b\,p - a\,b\,n^2 + 2\,a\,n$. The GCE pressure reads

$$p(T, \mu) = p_{\text{id}}(T, \mu^*) - a\,[n(T, \mu)]^2 \ . \tag{6.4}$$

The following transcendental equation for $\mu^*$ is solved numerically at given $T$ and $\mu$ pair:

$$\mu^* = \mu - b\,p_{\text{id}}(T, \mu^*) + 2\,a\,\frac{n_{\text{id}}(T, \mu^*)}{1 + b\,n_{\text{id}}(T, \mu^*)}. \tag{6.5}$$

After $\mu^*$ is found, the calculation of all other quantities is straightforward. More than a single solution may occur at a given $T$ and $\mu$ pair. Then, the solution with the largest pressure should be chosen, in accordance with the Gibbs criterium (see [138] for details).

## 6.2 Nuclear matter as a fermionic van der Waals system of nucleons

Nuclear matter is a hypothetical homogeneous, stationary, and infinite system of strongly interacting uncharged nucleons. The thermodynamics of nuclear matter (and its droplets) and its applications to the production of fission fragments were studied from the 1930s, and extensions to the liquid drop statistical multifragmentation models for heavy ion collisions were considered from the 1970s (see Refs. [3, 142, 143] for a review of these early developments). Nowadays, nuclear matter is described in many different models, in particular by relativistic mean-field (RMF) theory [144, 145, 146, 147, 148]. Experimentally, the discovery of the liquid-gas phase transition in nuclear matter has been claimed in different experiments [149, 150, 151, 152, 153, 154].

The liquid-gas phase transition in nuclear matter originates from the interplay of short-range repulsive and intermediate-range attractive interactions between nucleons. These two dominant contributions to nuclear interactions are found in $NN$-scattering experiments and yield the well known nuclear saturation properties at normal nuclear density and zero temperature. The repulsive interactions generally are attributed in mesonic field theory to the vector $\omega$ meson exchange
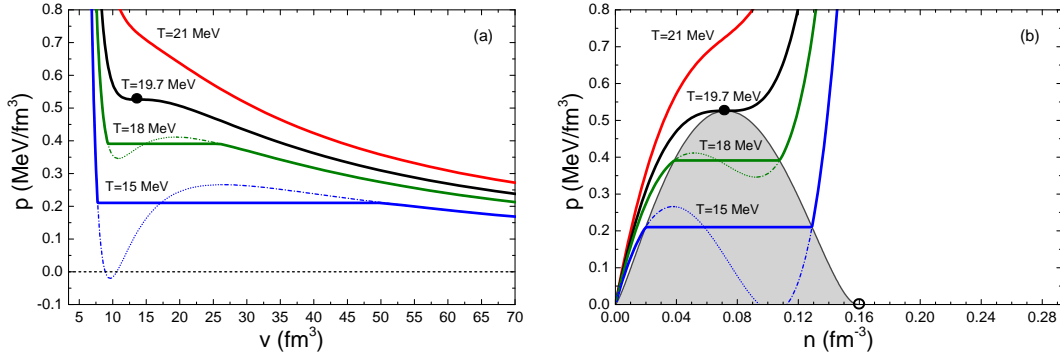
Figure 6.1: Pressure isotherms in (a) $(p, v)$ and (b) $(p, n)$ coordinates, calculated with the fermionic Van der Waals equation of state for nucleons with parameters $a \cong 329$ MeV·fm³ and $b \cong 3.42$ fm³ ($r \cong 0.59$ fm). The dashed-dotted lines present the metastable parts of the VDW isotherms at $T < T_c$, whereas the dotted lines correspond to unstable parts. The full circle on the $T = T_c$ isotherm corresponds to the critical point, while the open circle at $T = 0$ in (b) shows the ground state of nuclear matter.

while the attraction is taken to be mediated by the scalar mesons, $\sigma$ and $\pi$.

Here, nuclear matter is described by the fermionic VDW equation. Restricting the model to small temperatures, $T \leq 40$ MeV, pion production, as well the formation of baryonic resonances (like $N^*$ and $\Delta$), can be neglected. For simplicity, the formation of the nucleon clusters (i.e., $\alpha$, ordinary nuclei) is also neglected. Then, the number of nucleons $N$ is conserved and appears as an independent variable in the CE. The chemical potential $\mu$ in the GCE regulates the nucleon number density. We consider the symmetric nuclear matter, which consists of an equal number of protons and neutrons[1].

The VDW equation for nucleons then has two parameters, $a$ and $b$, which characterize the interactions between nucleons. These parameters are fixed by reproducing the known properties of the nuclear ground state: $p = 0$ and $\varepsilon/n = m + E/A \cong 922$ MeV at $T = 0$ and $n = n_0 \cong 0.16$ fm$^{-3}$. Here $E/A \cong -16$ MeV is the binding energy per nucleon. Then $a \cong 329$ MeV fm³ and $b \cong 3.42$ fm³. Note that the parameter $b$ of the proper particle volume can be expressed in terms of a corresponding classical hard-core radius $r$ as $b = 16\pi r^3/3$. This gives $r \cong 0.59$ fm for the effective hard-core nucleon radius in the nuclear ground state.

---

[1]The asymmetric nuclear matter can readily be modeled by employing the two-component fermionic VDW equation for protons and neutrons. This extension is considered in Chapter 8.

The corresponding Fermi-Dirac VDW pressure isotherms for nuclear matter are depicted in Fig. 6.1 (a) and (b), respectively for the $(T, v)$ and $(T, n)$ coordinates, where $v \equiv 1/n$ is the specific volume per nucleon. They are calculated within the quantum statistical Fermi-Dirac VDW equation of state using Eq. (6.2) with interaction parameters $a$ and $b$ adjusted to the nuclear matter ground state, as described above. The critical parameters are a prediction of the model: The critical temperature is found as $T_c \cong 19.7$ MeV, while the critical density is $n_c \cong 0.07$ fm$^{-3} \cong 0.4 \, n_0$, less then one-half of the normal nuclear density[2]. The predicted $T_c$ value in the model is close to experimental estimates [153, 154, 155]. At $T < T_c$ two phases are predicted: the gas and liquid phases, which are separated by a first-order phase transition. The mixed phase region is obtained from the Maxwell construction of equal areas for the $p(v)$ isotherms. The ground state of cold nuclear matter with $n = n_0 \cong 0.16$ fm$^{-3}$ and $T = 0$ has zero pressure and is located exactly on the boundary between the mixed phase and liquid phase at zero temperature. Note also that the maximum value of the nucleon number density in the VDW model is $n_{\max} = 1/b$, which equals $n_{\max} \cong 0.29$ fm$^{-3}$ for the obtained value of the parameter $b$.

## 6.3  Baryon number susceptibilities near the critical point of nuclear matter

The phase structure of nuclear matter in the $T$-$\mu$ plane is studied in this section. The nucleon number fluctuations, previously studied in Chapter 5 for the classical VDW fluid, are considered here for the fermionic VDW fluid. The number of nucleons in nuclear matter is a conserved quantity. Therefore, the $\chi_i$ can be identified with the net-baryon number susceptibilities. Such a calculation provides a useful qualitative guidance regarding the structure of the conserved charge fluctuations in the $(T, \mu)$ plane in the vicinity of the critical point. Thus, it is a useful tool for the ongoing search for the chiral CP in QCD matter.

---

[2]The Boltzmann approximation leads to $n_c = 1/3b \cong 0.10$ fm$^{-3}$ and $T_c = 8a/(27b) \cong$ 28.5 MeV.

The nucleon number density $n = \chi_1 T^3$ and the scaled variance

$$\omega[N] = \frac{\chi_2}{\chi_1} = \frac{T}{n}\left(\frac{\partial n}{\partial \mu}\right)_T = \omega_{\mathrm{id}}(T, \mu^*)\left[\frac{1}{(1 - bn)^2} - \frac{2an}{T}\,\omega_{\mathrm{id}}(T, \mu^*)\right]^{-1}, \quad (6.6)$$

are depicted in the upper panels of Fig. 6.2. The quantity $\omega_{\mathrm{id}}(T, \mu^*)$ is the scaled variance of the particle number fluctuations in the ideal Fermi gas.

The phase transition line, $\mu = \mu_{\mathrm{mix}}(T)$, shown in Fig. 6.2, starts from the nuclear matter ground state with $T = 0$ and $\mu_0 \cong 922$ MeV, and ends at the CP at $T_c \cong 19.7$ MeV and $\mu_c \cong 908$ MeV. At each point of the phase transition line, two solutions with different particle densities (the liquid and the gas states), but equal pressures co-exist, i.e., this is the line of the first-order phase transition. At $T > T_c$ only a single fluid solution, $n(T, \mu)$, exists.

A rapid, although continuous, change of particle number density is seen in a narrow $T$-$\mu$ band (the so-called crossover region), at $T > T_c$ is seen in the Fig. 6.2a.

The skewness

$$S\sigma = \frac{\chi_3}{\chi_2} = \omega[N] + \frac{T}{\omega[N]}\left(\frac{\partial \omega[N]}{\partial \mu}\right)_T, \quad (6.7)$$

and the kurtosis

$$\kappa\sigma^2 = \frac{\chi_4}{\chi_2} = (S\sigma)^2 + T\left(\frac{\partial[S\sigma]}{\partial \mu}\right)_T, \quad (6.8)$$

exhibited, respectively, in Fig. 6.2c and Fig. 6.2d, show a rich structure in this crossover region, characterized by multiple rapid sign changes of $S\sigma$ and $\kappa\sigma^2$ even far away from the CP.

The fluctuation patterns shown in Fig. 6.2 are qualitatively consistent with the predictions of the classical VDW equation shown in the previous Chapter 5. The presented findings are also consistent with results based on effective QCD-inspired models (see, e.g., Refs. [131, 156, 157]), and follow model-independent universality arguments with regards to critical behavior in the vicinity of the QCD critical point [127, 128].
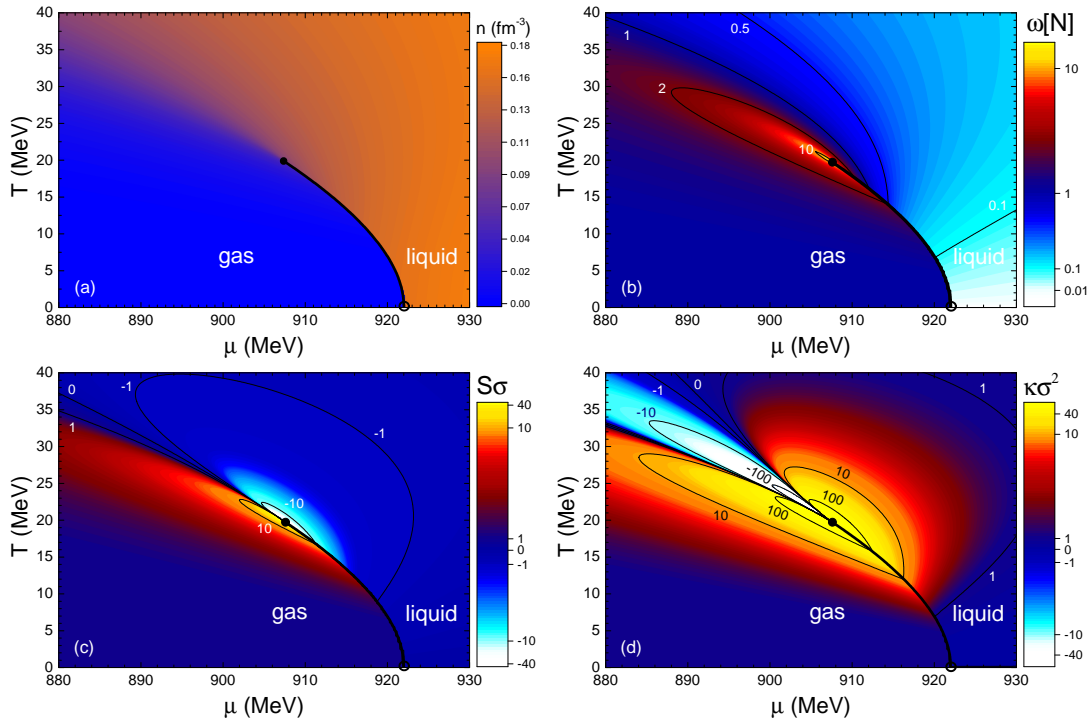
Figure 6.2: Contours of the (a) particle number density $n(T, \mu)$, (b) scaled variance $\omega[N]$ (6.6), (c) skewness $S\sigma$ (6.7), and (d) kurtosis $\kappa\sigma^2$ (6.8), as calculated for symmetric nuclear matter in $(T, \mu)$ coordinates within VDW equation of state for fermions. The open circle at $T = 0$ denotes the ground state of nuclear matter, the solid circle at $T = T_c$ corresponds to the CP, and the phase transition curve $\mu = \mu_{\mathrm{mix}}(T)$ is depicted by the solid line.

## 6.4   Beyond van der Waals model

Over the years, many modifications to the original VDW equation (5.1) were developed for chemistry-related applications. These modifications concern both the attractive and repulsive terms, and yield a class of the VDW-like equations of state for real gases. The procedure to include quantum statistics into the VDW model can be generalized for these real gas models. More specifically, one assumes that the free energy $F(T, V, N)$ of the quantum statistical real gas model has more general form compared to the standard VDW model (6.1), namely [140]

$$F(T, V, N) = F_{\mathrm{id}}(T, V f(n), N) + N u(n). \tag{6.9}$$

Here the function $f(n)$ quantifies the fraction of the total volume which is available for particles to move in at the given value of the particle density $n$. It has to take values in the range $0 \leq f(n) \leq 1$ and, compared to the standard EV model, it corresponds to a more general EV procedure. The quantity $u(n)$ in (6.9) is the self-consistent density-dependent *mean field*, corresponding to intermediate-range attractive interactions. All other quantities are calculated from free energy via standard thermodynamic identities (see [140] for details).

The VDW model follows as a partial case of Eq. (6.9) with $f_{\mathrm{VDW}}(n) = 1 - b\,n$ and $u_{\mathrm{VDW}}(n) = -a\,n$. Many other options are possible. To illustrate this, we consider a set of different fermionic VDW-like models for symmetric nuclear matter. Only two-parameter models are considered, where function $f(n)$ depends only on the VDW-like eigenvolume parameter $b$, and where mean field $u(n)$ depends only on the VDW-like attraction parameter $a$. The repulsive term is based on either VDW or Carnahan-Starling [158] EV models:

1. VDW excluded volume

$$f(n) = 1 - bn.$$

2. CS excluded volume

$$f(n) = \exp\left(-\frac{(4 - 3\eta)\eta}{(1 - \eta)^2}\right), \qquad \eta = bn/4.$$

The attractive term is based on VDW, Redlich-Kwong-Soave [159, 160], Peng-Robinson [161], and Clausius based equations:

1. VDW

$$u(n) = -a\,n.$$

2. Redlich-Kwong-Soave

$$u(n) = -\frac{a}{b}\,\log(1 + bn).$$

3. Peng-Robinson

$$u(n) = -\frac{a}{2\sqrt{2}b}\,\log\left(\frac{1 + bn + \sqrt{2}bn}{1 + bn - \sqrt{2}bn}\right).$$
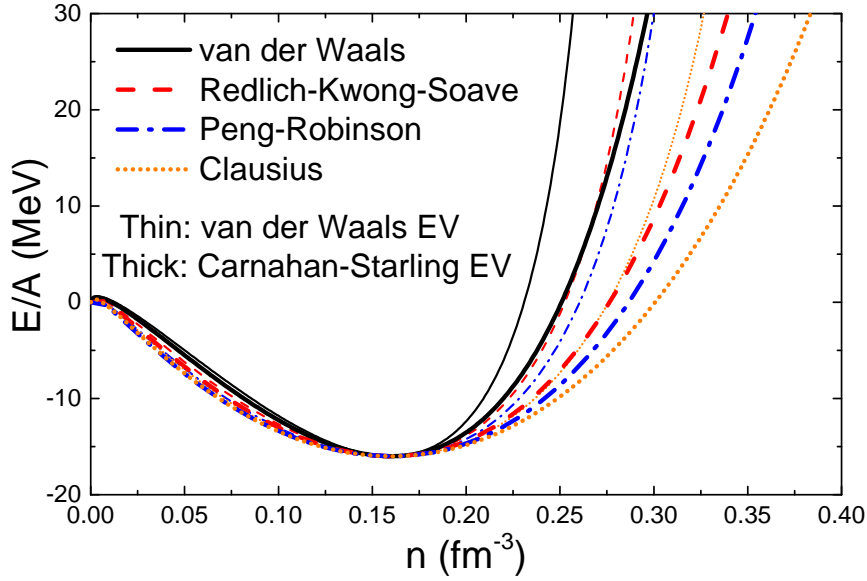
Figure 6.3: The nucleon number density dependence of the binding energy per nucleon $E/A$ in symmetric nuclear matter calculated within eight different real gas models at $T = 0$. The thin lines denote calculations within four models with the VDW EV term, i.e. they correspond to VDW (solid black line), Redlich-Kwong-Soave (dashed red line), Peng-Robinson (dash-dotted blue line), and Clausius (dotted orange line) models. The thick lines correspond to models with the Carnahan-Starling EV term.

4. Clausius

$$u(n) = -\frac{an}{1 + cn}.$$

All combinations give a total of eight different models. The values of $a$ and $b$ are fixed by the ground state of nuclear matter separately for each model, in the same way it was done for the VDW model[3].

All considered models provide qualitatively similar description of nuclear matter, in particular regarding the critical parameters and critical fluctuations (see all of the details in [140]). Differences between models are more pronounced if one compares stiffness between the resulting equations of state. This is illustrated by the density dependence of the binding energy per nucleon $E/A$ at $T = 0$ shown in Fig. 6.3: The behavior of $E/A$ is changes significantly between different real gas models at densities above the saturation density $n_0$. The VDW

---

[3]In general, Clausius equation permits variation of three parameters: $a$, $b$, and $c$. In the present work $c \equiv b$ is assumed.

model yields the stiffest equation of state, with the nuclear "incompressibility" factor $K_0 = 9\,(\partial P/\partial n)_T \cong 763$ MeV in the ground state. This is well above the empirical range $250 - 315$ MeV [162]. On the other hand, the model with Carnahan-Starling EV term and Clausius attraction term yields $K_0 \cong 333$ MeV, much closer to empirical estimates, and better than the $K_0 \cong 550$ MeV value obtained in the standard Walecka model [163]. The present formalism permits variation of the third parameter $c$ in the Clausius model. The parameter $c$ can be varied to obtain the needed value of $K_0$. Thus, the Clausius model leaves room for further improvement in the description of nuclear matter.

This new class of quantum statistical real gas models opens many potential applications, both in nuclear/hadronic physics and, hopefully, in other fields as well. These will be explored further elsewhere.

# Chapter 7

# From nuclear matter to lattice QCD

Frequently, the hadronic equation of state is modeled in the context of high-temperature QCD with the aforementioned ideal hadron resonance gas (Id-HRG) model. In theory, the Id-HRG takes into account attractive interactions mediated by narrow resonances[1]. The Id-HRG, however, fails to describe the basic qualitative features of the baryon-baryon interactions. In particular, the nucleon-nucleon interactions are strongly repulsive at small distances, and attractive at intermediate distances, and both without any resonance structure in the scattering phase shifts. These important features of the nucleon-nucleon interaction are manifested in a straightforward manner in the framework of the van der Waals model, as seen in previous Chapter 6. This ansatz is generalized here to include the baryon-baryon interactions in the full HRG, mainly following the results of Ref. [166].

## 7.1 The VDW-HRG model

Within the newly developed quantum statistical VDW formalism for spin 1/2 nucleons we are now ready to add further baryon-baryon interactions into the HRG model. One may wonder whether such a generalization is necessary, in

---

[1]Note, however, that this approximation may not be appropriate for wide resonances [164, 165]

particular for the high-temperature region of the phase diagram away from the nuclear matter ground state. After all, doesn't the ideal HRG model describe so successfully many lattice QCD observables in temperature range $T \sim 100 - 150$ MeV, where, as one believes, confinement is at work? However, the agreement between Id-HRG and lattice QCD deteriorates drastically in the crossover region. The complete breakdown of the Id-HRG model is so dramatic for both, higher order fluctuations and correlations of conserved charges [167], that statements like that this behavior proves that hadrons melt quickly with increasing temperature and virtually disappear at $T > 160$ MeV [168] form a virtual paradigm for the "standard scenario" in the relativistic heavy ion community. Is this paradigm actually supported by a critical and objective analysis? The effect that baryon-baryon VDW interactions have on these observables suggests that this may not be the case.

A minimal extension of the Id-HRG model is described below. It includes the VDW interactions between (anti)baryons. This model is referred to as the VDW-HRG. It is based on the following assumptions:

1. VDW interactions are taken to exist between all pairs of baryons and between all pairs of antibaryons. The VDW parameters $a$ and $b$ for all (anti)baryons are taken to be equal to those of nucleons, as obtained from the fit to the ground state of nuclear matter.

2. The baryon-antibaryon, meson-meson, and meson-(anti)baryon VDW interactions are set to zero.

The present VDW-HRG model is a "minimal-interaction" extension of the Id-HRG model, which describes the basic properties of nuclear matter. Whether significant VDW interactions exist between hadron pairs other than (anti)baryons is not clearly established. It has been argued that short-range interactions between baryons and antibaryons are dominated by annihilation processes and not by repulsion [93], and this is the motivation to exclude VDW terms for them in this study. Presence of significant mesonic eigenvolumes, comparable to those of baryons, leads to significant suppression of thermodynamic functions in the crossover region at $\mu_B = 0$, which is at odds with lattice data (see Refs. [56, 93]). The attractive interactions involving mesons, on the other hand, normally lead to resonance formation [169], which are already included in HRG by construc-

tion. For these reasons the meson-related VDW interactions are neglected in this study. The VDW-HRG consists of three distinct sub-systems: VDW baryons, VDW antibaryons, and non-interacting mesons. The total pressure reads

$$p(T, \boldsymbol{\mu}) = P_B(T, \boldsymbol{\mu}) + P_{\bar{B}}(T, \boldsymbol{\mu}) + P_M(T, \boldsymbol{\mu}), \tag{7.1}$$

with

$$P_B(T, \boldsymbol{\mu}) = \sum_{j \in B} p_j^{\text{id}}(T, \mu_j^{B*}) - a\, n_B^2, \tag{7.2}$$

$$P_{\bar{B}}(T, \boldsymbol{\mu}) = \sum_{j \in \bar{B}} p_j^{\text{id}}(T, \mu_j^{\bar{B}*}) - a\, n_{\bar{B}}^2, \tag{7.3}$$

$$P_M(T, \boldsymbol{\mu}) = \sum_{j \in M} p_j^{\text{id}}(T, \mu_j), \tag{7.4}$$

where $M$ stands for mesons, $B$ for baryons, and $\bar{B}$ for antibaryons, $p_j^{\text{id}}$ are the Fermi-Dirac and Bose-Einstein ideal gas pressures, $\boldsymbol{\mu} = (\mu_B, \mu_S, \mu_Q)$ are the chemical potentials which regulate the average values of total baryonic number $B$, strangeness $S$, and electric charge $Q$, and $\mu_j^{B(\bar{B})*} = \mu_j - b\, P_{B(\bar{B})} - a\, b\, n_{B(\bar{B})}^2 + 2\, a\, n_{B(\bar{B})}$. $n_B$ and $n_{\bar{B}}$ are the total densities of baryons and antibaryons, respectively. They are calculated as the derivatives of $P_{B(\bar{B})}$ with respect to the baryochemical potential, i.e.

$$n_{B(\bar{B})} = (1 - b\, n_{B(\bar{B})}) \sum_{j \in B(\bar{B})} n_j^{\text{id}}(T, \mu_j^{B(\bar{B})*}) . \tag{7.5}$$

The calculation of the mesonic pressure $P_M(T, \boldsymbol{\mu})$ is straightforward. The calculations of the baryon or antibaryon pressures, and other related observables proceed essentially analogous to the single-component cases. The shift $\Delta\mu_B$ in the chemical potential due to VDW interactions is

$$\Delta\mu_B = \mu_i^{B*} - \mu_i = -b\, P_{B(\bar{B})} - a\, b\, n_{B(\bar{B})}^2 + 2\, a\, n_{B(\bar{B})} \tag{7.6}$$

i.e. it is identical for all (anti)baryons. It is determined by the numerical solution of the transcendental equation (7.6) for this quantity.
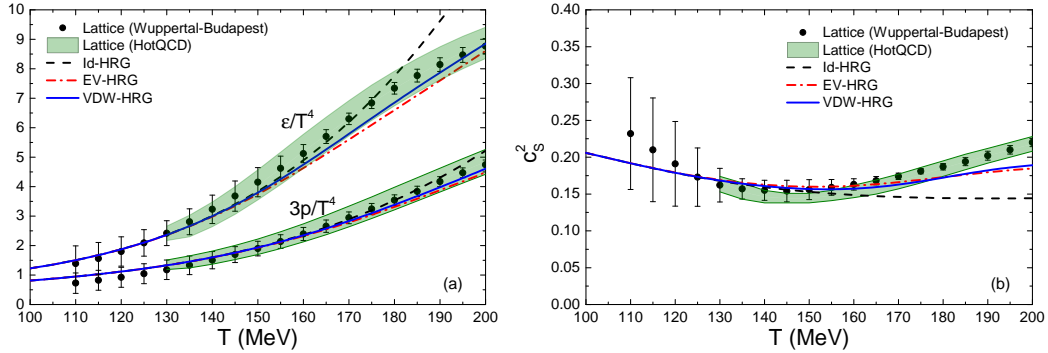
Figure 7.1: The temperature dependence of (a) scaled pressure and energy density, and of (b) the square of the speed of sound at zero chemical potential, as calculated within Id-HRG (dashed black lines), EV-HRG (dash-dotted red lines), and VDW-HRG (solid blue lines). Lattice QCD results of Wuppertal-Budapest [12] and HotQCD [13] collaborations are shown, respectively, by symbols and green bands.

## 7.2  Comparison to lattice QCD data

The temperature dependence of the scaled pressure $p/T^4$, energy density $\varepsilon/T^4$, and the speed of sound squared $c_s^2 = dp/d\varepsilon$ is compared to lattice QCD data at $\mu = 0$ for the Id-HRG and the VDW-HRG scenarios in Fig. 7.1. For additional clarity, the calculations where attractive VDW interactions are "switched off" ($a = 0$) are denoted as EV-HRG.

There is important difference between the present approach and earlier studies involving hadronic interactions [56, 93], namely, only the EV interactions between (anti)baryons are included, but no interactions involving any other hadron pairs. As the matter at $\mu_B = 0$ is meson dominated and the mesons are modeled as point-like non-interacting particles, no significant suppression of thermodynamic functions is seen below $T = 160$ MeV. The temperature dependence of the speed of sound squared, $c_s^2$, is consistent with lattice data and shows a minimum at $T \sim 155 - 160$ MeV, in contrast to the Id-HRG where $c_s^2$ decreases slowly and monotonically.

In addition to the GCE thermodynamical functions, the VDW-HRG model
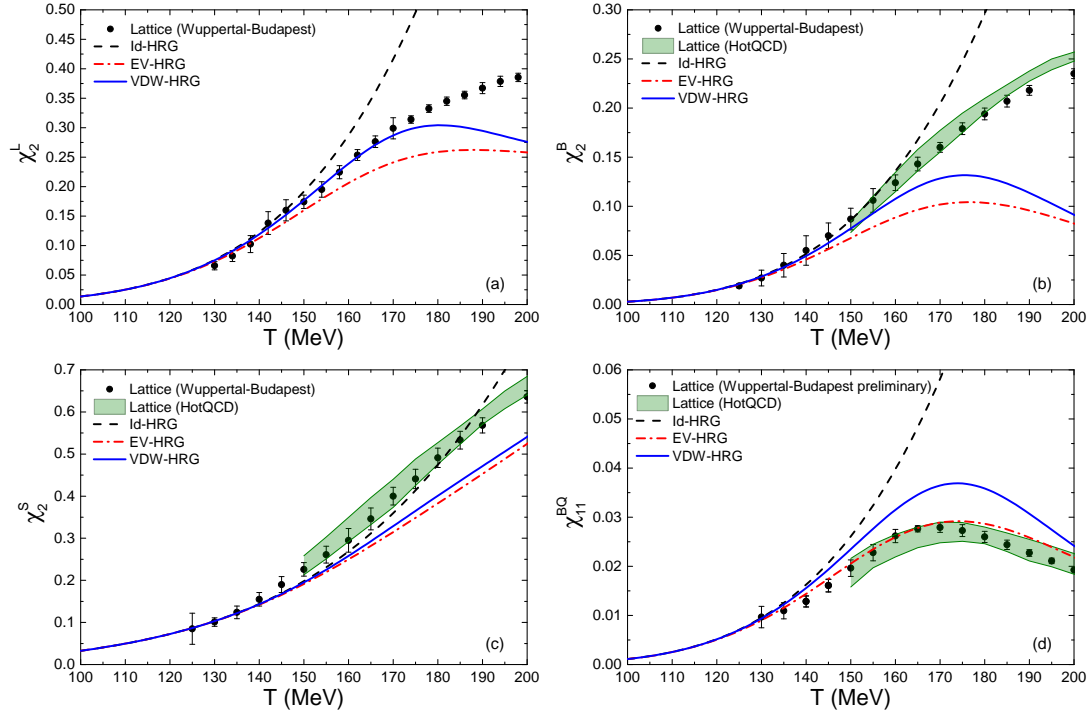
Figure 7.2: The 2nd order susceptibilities of conserved charges are plotted as function of the temperature dependence of These include (a) the net number of light quarks $\chi_2^L$, (b) the net baryon number $\chi_2^B$, (c) the net strangeness $\chi_2^S$, and (d) the baryon-electric charge correlator $\chi_{11}^{BQ}$. Calculations are done within Id-HRG (dashed black lines), EV-HRG (dash-dotted red lines), and VDW-HRG (solid blue lines). Lattice QCD results of the Wuppertal-Budapest [41, 44] (for $\chi_{11}^{BQ}$ preliminary results [170, 171] are used) and HotQCD [42] collaborations are shown, respectively, by symbols and green bands.

does also allow to calculate the fluctuations of conserved charges:

$$\chi_{lmn}^{BSQ} = \frac{\partial^{l+m+n} p/T^4}{\partial(\mu_B/T)^l \, \partial(\mu_S/T)^m \, \partial(\mu_Q/T)^n} \; . \qquad (7.7)$$

The fluctuations of the net number of light quarks $L = (u+d)/2 = (3B+S)/2$ are also calculated.

The 2nd order susceptibilities are shown as function of the temperature in Fig. 7.2 for (a) the net number of light quarks $\chi_2^L$, (b) the net baryon number $\chi_2^B$, (c) the net strangeness $\chi_2^S$, and (d) the baryon-electric charge correlator $\chi_{11}^{BQ}$. The $\chi_2^L$ calculated within the VDW-HRG model shows a very different

behavior compared to Id-HRG at $T > 160$ MeV, and agrees well with the lattice data obtained from Ref. [41] up to $T = 180$ MeV. A qualitatively similar picture is obtained for $\chi_2^B$. The qualitative difference between Id-HRG and VDW-HRG appears to be driven by the eigenvolume interaction terms between (anti)baryons, while the inclusion of VDW attraction leads to an improved agreement with the lattice data. This is illustrated by the EV-HRG calculations, shown by dash-dotted red lines in Fig. 7.2. The strangeness susceptibility $\chi_2^S$ is described fairly well by Id-HRG model while it is strongly underestimated by the VDW-HRG model.

The correlator $\chi_{11}^{BQ}$ between the net baryon number and net electric charge has a very different temperature dependence in Id-HRG and VDW-HRG. The $\chi_{11}^{BQ}$ increases rapidly above $T > 150$ MeV in Id-HRG, in stark contrast to the lattice data. On the other hand, this correlator exhibits a broad bump with a maximum at $T \sim 160 - 190$ MeV in the VDW-HRG. This agrees qualitatively with the correlator obtained by the lattice QCD.

Higher order fluctuations are analyzed in Fig. 7.3: All observables show very different behavior between the Id-HRG and the VDW-HRG models. The net-light quark number $\chi_4^L/\chi_2^L$ increases monotonically in the Id-HRG. This overshoots the lattice data at $T \sim 140$ MeV. The VDW-HRG model, in contrast, exhibits a non-monotonic behavior, with a wide peak at $T \sim 120 - 145$ MeV. Thus, the VDW-HRG model resembles the lattice data [44]. The bump in the lattice data seems to appear at slightly higher temperatures. Also the peak in the $T$-dependence of the net strangeness $\chi_4^S/\chi_2^S$ is rather well reproduced within the VDW-HRG. In contrast, the Id-HRG model shows no maximum at all, at odds with lattice QCD.

It is remarkable that the VDW-HRG model shows flavor hierarchy: the peak for the net-light quark number $\chi_4/\chi_2$ is located at lower temperatures as compared to the peak in the net-strangeness. This is also the lattice QCD result! Scientists argued that this observation is related to flavor separation in the conjectured deconfinement "transition" of QCD [44]. The VDW-HRG model is based on hadronic degrees of freedom. Hence, an interpretation of the observed flavor dependence in $\chi_4/\chi_2$ as indication of complete deconfinement at $\sim 155$ MeV is doubtful. Also, the presence of the peaks themselves does not exclude a large
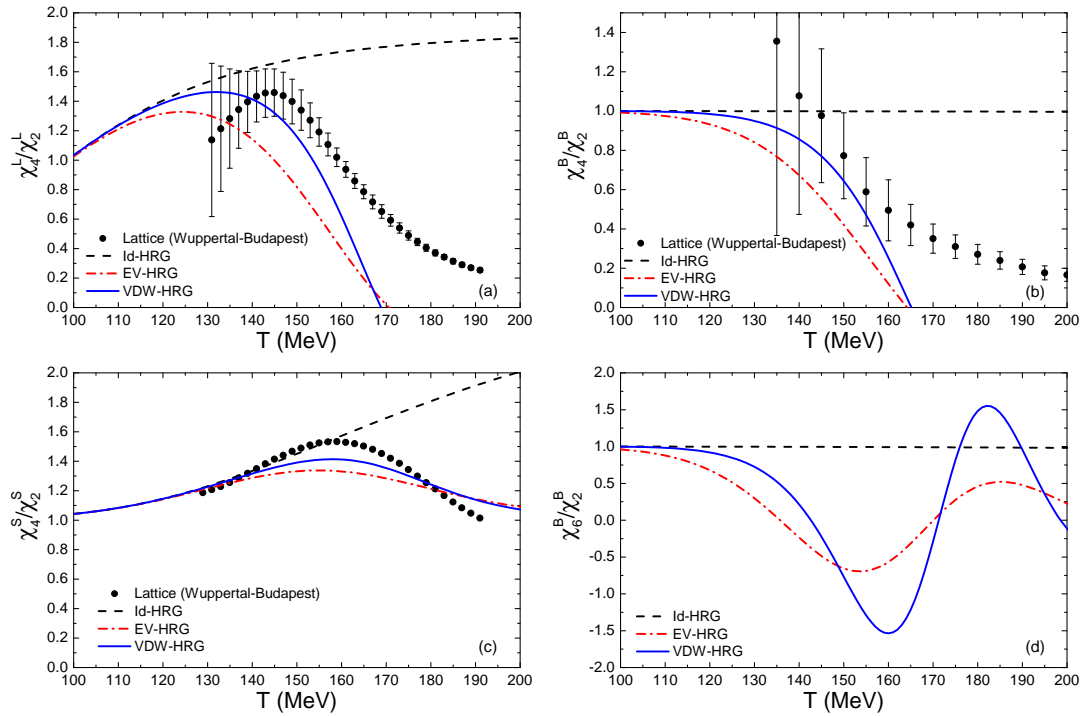
Figure 7.3: The temperature dependence of the $\chi_4/\chi_2$ cumulant ratio for (a) the net number of light quarks, (b) the net baryon number, (c) the net strangeness, and for (d) the $\chi_6/\chi_2$ cumulant ratio for net baryon number. Calculations are done within Id-HRG (dashed lines), EV-HRG (dash-dotted lines), and VDW-HRG (solid lines). The lattice QCD results of the Wuppertal-Budapest collaboration [44, 43] are shown by symbols.

contribution of confined baryons and mesons to the EoS at $T \sim 160 - 200$ MeV.

Let us turn to higher-order fluctuations of the net-baryon number: The net-baryon kurtosis, $\chi_4^B/\chi_2^B$, shows the expected Skellam behavior for the Id-HRG model with values very close to unity. The VDW-HRG model, on the other hand, shows a strong decrease at $T = 130 - 165$ MeV, i.e. even below the so-called "crossover region", even though the VDW-HRG model does not involve a deconfinement transition to quark-gluon degrees of freedom. The $\chi_4^B/\chi_2^B$ values turn negative at $T > 165$ MeV. This strong decrease of $\chi_4^B/\chi_2^B$ is also seen in the lattice data [43], starting at $T = 145$ MeV, although the $\chi_4^B/\chi_2^B$ does not drop below zero on the lattice.

The temperature dependence of the sixth order cumulant ratio $\chi_6^B/\chi_2^B$ is *pre-*

*dicted* by the VDW-HRG model: It exhibits very strong variations and a non-monotonous behavior in the "crossover region". Will a similarly dramatic $T$-dependent behavior be observed in the corresponding lattice simulations once they become available?

For many observables, the *qualitative* agreement of the VDW-HRG calculations with the lattice data in the "crossover region" as presented here is quite astounding. The fact that quantitatively it is far from perfect is hardly surprising. Indeed, we have modeled the VDW interactions between baryons in the simplest way possible: The VDW interactions between all baryons are taken to be the same as those between nucleons, which are obtained from nuclear matter properties at $T = 0$. Conceptually, the VDW-HRG model is quite different from an underlying fundamental QCD theory. However, the analysis presented here is essentially parameter-free: no new parameters are adjusted to lattice data. Indeed, the two VDW parameters, fixed by reproducing the saturation properties of nuclear matter [138, 141], are independent of any lattice data! While there is other model input, e.g., the list of hadrons and their decay properties, they are known and fixed experimentally. It is feasible that VDW parameters could be different for different baryon pairs, and along with other input parameters like mass, width, etc. may be temperature and density dependent. The agreement of the VDW-HRG model with the lattice data can be improved considerably by allowing for a decrease of the nucleon/baryon eigenvolumes, $b \simeq 2 - 3$ fm$^3$. Such modifications do not necessarily diminish the agreement of the VDW-HRG model with the properties of nuclear matter: as suggested in Ref. [172], the heavier and/or strange baryons may have smaller eigenvolumes, thus reducing effectively the average $b$. Alternative ways of generalizing the attractive part of the VDW interactions from nucleons to the full HRG may be considered. The VDW-HRG model presented here leaves plenty of room for improvement. However, major qualitative changes to the results presented here are not expected.

## 7.3   Finite net baryon density

The VDW-HRG model is not restricted to the vanishing net-baryon density. It can easily be applied at finite $\mu_B$, in contrast to lattice QCD where direct
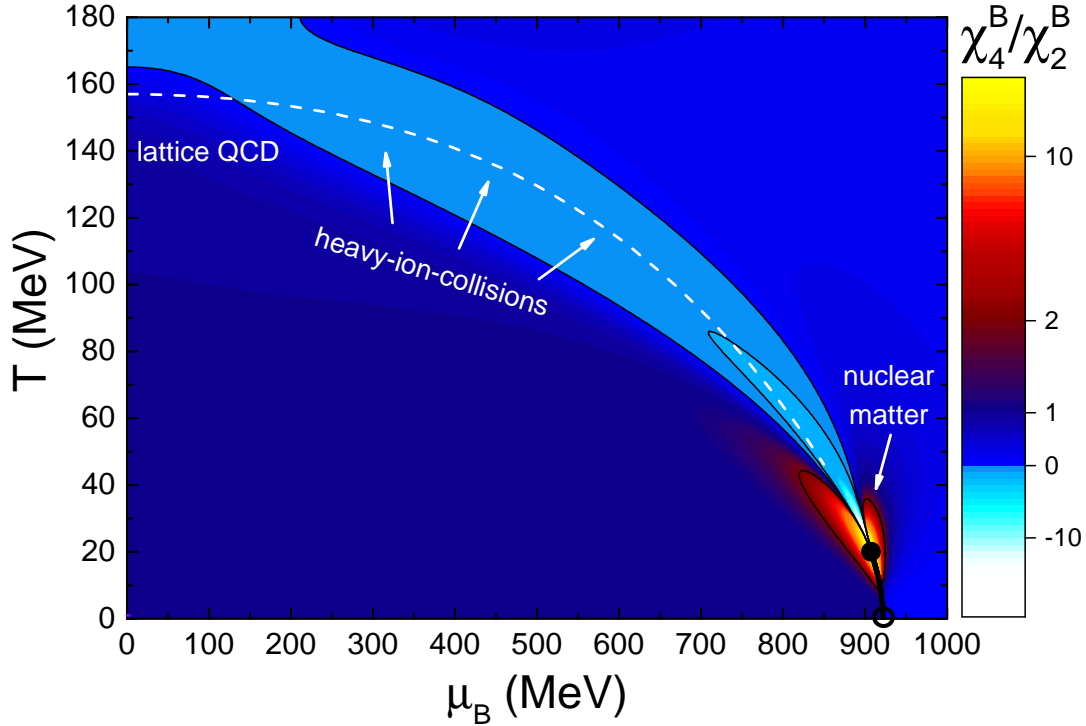
Figure 7.4: The $\chi_4^B/\chi_2^B$ kurtosis ratio for the net baryon number fluctuations calculated in the VDW-HRG model is exhibited in the $T$-$\mu_B$ plane. The possible chemical freeze-out line in heavy-ion collisions obtained in Section 3.2 is sketched by the dashed line.

calculations at finite baryochemical potential are hindered by the sign problem. The $T$-$\mu_B$ dependence of the kurtosis ratio $\chi_4^B/\chi_2^B$ of the net-baryon fluctuations is exhibited in Fig. 7.4 as an illustration. It is assumed that $\mu_S = \mu_Q = 0$ for simplicity. The region of negative $\chi_4^B/\chi_2^B$ at small $\mu_B$ is smoothly connected to the region of the liquid-gas phase transition in nuclear matter. Obviously, the nuclear liquid-gas transition is relevant for the $\chi_4^B/\chi_2^B$ values all the way up to $T \sim 200$ MeV, including the prescribed region of "chemical freeze-out" in heavy-ion collisions (see dashed line in Fig. 7.4). The VDW-HRG model predicts a non-monotonic behavior of $\chi_4/\chi_2$ with respect to the collision energy, in stark contrast to the ideal HRG [173]. This implies that non-trivial fluctuations of net-baryon number in heavy-ion collisions manifest traces of the nuclear liquid-gas phase transition (see also [174] and [175]).

This result is directly relevant for the ongoing and future fluctuation mea-

surements performed in heavy-ion collision experiments. Proper understanding of the role played by the nuclear matter physics is crucial for interpretation of the fluctuation measurements. First such measurements were recently published by STAR collaboration [122, 123, 176] within the Beam Energy Scan program at RHIC. There is also an ongoing analysis within the GSI-HADES experiment, at lower collision energies and closer to the nuclear matter region. The study of higher-order moments of event-by-event fluctuations is a major part of the future CBM experiment at FAIR [177].

## 7.4   Imaginary chemical potential

The dependence of the net-baryon density on temperature $T$ and (baryo)chemical potential $\mu_B{}^2$ in QCD can be considered as the following series expansion:

$$\frac{\rho_B(T,\mu_B)}{T^3} = \sum_{k=1}^{\infty} b_k(T)\,\sinh(k\mu_B/T), \qquad (7.8)$$

with the hitherto unknown temperature-dependent coefficients $b_k(T)$. Analytic continuation to imaginary $\mu_B = i\widetilde{\mu}_B$ yields

$$\frac{\rho_B(T,\widetilde{\mu}_B)}{T^3} = i\sum_{k=1}^{\infty} b_k(T)\,\sin(k\widetilde{\mu}_B/T). \qquad (7.9)$$

The net-baryon density at imaginary chemical potential becomes an imaginary complex number itself. The coefficients $b_k(T)$ turn out to be nothing else but the Fourier coefficients of the trigonometric series expansion of the $\rho_B(T,\widetilde{\mu}_B)$.

The form (7.9) is particularly useful for lattice QCD. Lattice simulations are not hindered by the sign problem at imaginary chemical potential. Thus, lattice simulations at imaginary $\mu$ shed information on the QCD equation of state at real $\mu$, provided that analytic continuation works (see, e.g., Refs. [178, 179], or more recent [180, 181]).

The preliminary results of the Wuppertal-Budapest collaboration for coefficients $b_k(T)$ of the imaginary $\mu_B$ expansion (7.9) were recently reported in [182].

---

[2]We assume here $\mu_S = \mu_Q = 0$ for simplicity.

They are exhibited in Fig. 7.5, and show a peculiar hierarchy: the higher coefficient order $k$ corresponds to the higher temperature values where $b_k$ starts to deviate from zero. Moreover, one clearly observes the alternating sign hierarchy: odd order coefficients, $b_1$ and $b_3$, are positive while the even order coefficients, $b_2$ and $b_4$, are negative.

The lattice results can be compared to the predictions of the (non)interacting HRG model. To keep things simple, we neglect the quantum statistical effects. This is a good approximation for the baryon-related observables of interest.

Only the first coefficient, $b_1(T)$, is non-zero in the ideal HRG model. Its behavior in the Id-HRG model is consistent with lattice data at $T \lesssim 190$ MeV. The Id-HRG description clearly breaks down at $T > 160$ MeV, where the $b_2(T)$ deviates from zero on the lattice. Let us now turn to the VDW-HRG model: the coefficients $b_k(T)$ can be calculated analytically in this model. First, it follows from Eq. (7.5) that, in the Boltzmann approximation, the cumulative density of all baryons $n_B$ is the solution of the following equation

$$n_B = (1 - b\,n_B)\,e^{\frac{\mu_B}{T}}\,\phi_B(T)\,\exp\left(-\frac{b\,n_B}{1 - b\,n_B}\right)\exp\left(\frac{2\,a\,n_B}{T}\right), \qquad (7.10)$$

where

$$\phi_B(T) = \sum_{i \in B} \int dm\,\rho_i(m)\,\frac{d_i\,m_i^2\,T}{2\pi^2}\,K_2\left(\frac{m_i}{T}\right), \qquad (7.11)$$

with $\rho_i$ being a properly normalized mass distribution for hadron type $i$, taking into account non-zero resonance width, and where sum goes over all baryons in the system (but *not* antibaryons). Due to the baryon-antibaryon symmetry the total density of antibaryons $n_{\bar{B}}$ satisfies an identical equation with a change $\mu_B \to -\mu_B$. By plugging in the following fugacity expansion

$$\frac{n_{B(\bar{B})}}{T^3} = \frac{1}{2}\sum_{k=1}^{\infty} b_k(T)\,\exp\left(\pm\frac{k\,\mu_B}{T}\right) \qquad (7.12)$$
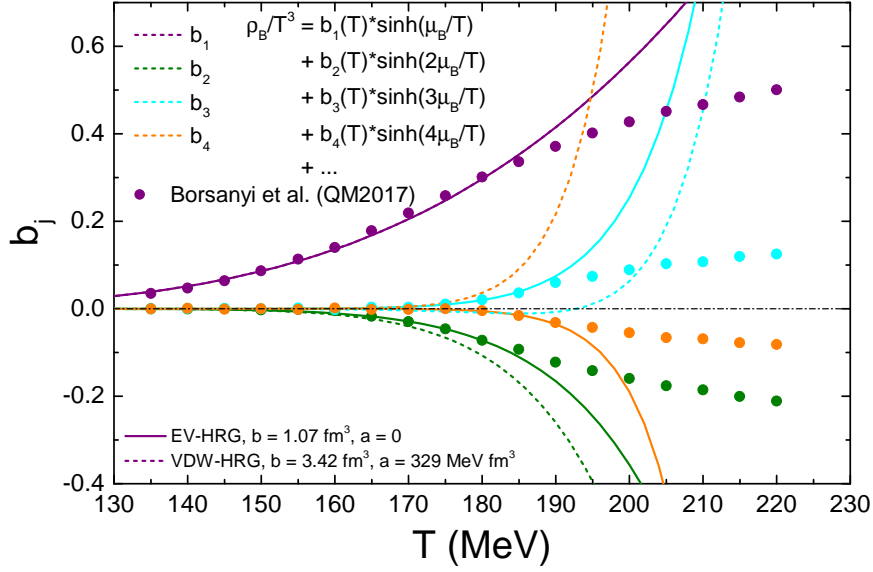
Figure 7.5:    The temperature dependence of the Fourier coefficients $b_k(T)$ in Eq. (7.9) calculated in the VDW-HRG model (dashed lines), and the EV-HRG model with $b = 1.07$ fm$^3$ (solid lines). The preliminary lattice data of the Wuppertal-Budapest collaboration [182] are shown by symbols.

of the total (anti)baryon density into the Eq. (7.10) one obtains

$$b_1(T) = 2\,\frac{\phi_B(T)}{T^3}, \tag{7.13}$$

$$b_2(T) = -4\left(b - \frac{a}{T}\right)\phi_B(T)\,\frac{\phi_B(T)}{T^3}, \tag{7.14}$$

$$b_3(T) = 9\left(b^2 - \frac{8}{3}\frac{a\,b}{T} + \frac{4}{3}\frac{a^2}{T^2}\right)[\phi_B(T)]^2\,\frac{\phi_B(T)}{T^3}, \tag{7.15}$$

$$b_4(T) = -\frac{64}{3}\left(b^3 - \frac{39}{8}\frac{a\,b^2}{T} + 6\frac{a^2\,b}{T^2} - 2\frac{a^3}{T^3}\right)[\phi_B(T)]^3\,\frac{\phi_B(T)}{T^3}. \tag{7.16}$$

The baryon-baryon VDW interactions do not affect the first coefficient $b_1(T)$, which coincides with the Id-HRG result. On the other hand, the higher-order terms are affected non-trivially. The VDW-HRG model calculation results are exhibited in Fig. 7.5 by the dashed lines. As before, the VDW parameters $a$ and $b$ are fixed by the nuclear matter ground state, The VDW-HRG model describes the drop of $b_2(T)$ fairly well up to $T \simeq 170 - 180$ MeV. At higher temperatures the model misses both the $b_2$ and the higher order terms. This behavior is rather similar to the previously shown comparison regarding lattice data at $\mu_B = 0$ .

The analysis can be further simplified by "switching off" the attraction term, i.e. letting $a = 0$. In this EV-HRG model one has

$$b_1(T) = 2\,\frac{\phi_B(T)}{T^3}, \qquad\qquad b_2(T) = -4\,[b\phi_B(T)]\,\frac{\phi_B(T)}{T^3}, \qquad (7.17)$$

$$b_3(T) = 9\,[b\,\phi_B(T)]^2\,\frac{\phi_B(T)}{T^3}, \qquad b_4(T) = -\frac{64}{3}\,[b\,\phi_B(T)]^3\,\frac{\phi_B(T)}{T^3}, \qquad (7.18)$$

i.e. the alternating sign structure seen in lattice data is obtained analytically! By adjusting the baryon-baryon EV parameter to a smaller value, $b \simeq 1.07$ fm³ $(r_B = 0.40$ fm$)$, the lattice data is well reproduced up to $T \simeq 185 - 190$ MeV, simultaneously for all four coefficients. This preliminary study clearly illustrates the potential of lattice QCD observables at imaginary chemical potential to constrain properties of the hadron-hadron interactions in high-temperature QCD.

# Chapter 8

# Multi-component quantum statistical van der Waals equation

Useful applications of the quantum statistical VDW equation were illustrated in previous two chapters. At the same time, all these applications have been limited to a single-component case: the VDW parameters $a$ and $b$ for all particle pairs in a (sub)system must be identical. A multi-component generalization opens up more applications. One example is asymmetric nuclear matter, which could be described as a two-component VDW mixture of protons and neutrons. The multi-component formulation will also allow to take into account the formation and interaction of nucleonic clusters (light nuclei) in the nuclear matter. Finally, the flavor-dependent VDW interactions discussed in the previous chapter, can naturally be modeled in such a framework.

In this chapter a general formalism of the VDW model, with both repulsive and attractive interactions, for the multi-component system of particles is introduced. This new formalism includes the quantum statistical effects. It is developed in a similar fashion to the single-component VDW fluid in Chapter 6. At the same time, it allows to specify arbitrary attraction and repulsion parameters for each pair of particle species. Thus, all previously considered EV/VDW models follow as different partial cases of this formalism.

## 8.1  Canonical ensemble formulation

The classical multi-component system with VDW interactions can be defined within the CE in terms of the following pressure function:

$$p(T, n_1, \ldots, n_f) = \sum_i \frac{T \, n_i}{1 - \sum_j \tilde{b}_{ji} \, n_j} - \sum_{i,j} a_{ij} \, n_i \, n_j \, , \qquad (8.1)$$

where $n_i$ is the particle density for $i$th species $(i = 1, \ldots, h)$ and $T$ is the system temperature. Parameters $a_{ij}$ and $\tilde{b}_{ji}$ in Eq. (8.1) correspond to the VDW attractive and repulsive interactions, respectively. The first term in Eq. (8.1) coincides with the pressure of the "Crossterms" EV model, that is Eq. (2.16) in Chapter 2. The second term in Eq. (8.1) gives the negative contribution to the CE pressure due to attractive interactions between all pairs of particles.

A starting point for further steps is a construction of the free energy $F(T, V, \{N_i\})$. Solving the differential equation $p = -(\partial F / \partial V)_{T, \{N_i\}}$ for $F$ one obtains

$$F(T, V, \{N_i\}) = \sum_i F_i^{\text{id}}(T, V - \sum_j \tilde{b}_{ji} N_j, N_i) - \sum_{i,j} a_{ij} \frac{N_i \, N_j}{V} \, . \qquad (8.2)$$

A function $F_i^{\text{id}}(T, V, N_i)$ is the free energy of a classical (Boltzmann) ideal gas for particle species $i$. It is given by Eq. (5.5).

Expressions (8.1) and (8.2) do not include the effects of quantum statistics. To include these effects it is assumed that free energies $F_i^{\text{id}}$ in Eq. (8.2) correspond to the ideal *quantum* gas expressions (Fermi or Bose). This is done in a clear analogy to the single-component quantum statistical VDW fluid in Chapter 6. Such a procedure satisfies the following properties. It leads to a mixture of the ideal quantum gases if all $\tilde{b}_{ij} = 0$ and $a_{ij} = 0$. It gives the classical model (8.1) in the regions of the thermodynamical parameters where quantum statistics can be neglected. Finally, the entropy obtained for the quantum VDW gases is non-negative and it goes to zero at $T \to 0$.

Using the free energy, one can calculate all other thermodynamical functions in the CE. Pressure $p$, total system entropy $S$ and energy $E$, and chemical potential

$\mu_i$ for $i$th particle species are obtained:

$$p(T, \{n_k\}) \equiv -\left(\frac{\partial F}{\partial V}\right)_{T,\{N_j\}} = \sum_i p_i^{\text{id}}\left(T, \frac{n_i}{f_i}\right) - \sum_{i,j} a_{ij}\, n_i\, n_j \ , \quad (8.3)$$

$$S(T, V, \{N_k\}) \equiv -\left(\frac{\partial F}{\partial T}\right)_{V,\{N_j\}} = V \sum_i f_i\, s_i^{\text{id}}\left(T, \frac{n_i}{f_i}\right) \ , \quad (8.4)$$

$$E(T, V, \{N_k\}) \equiv F + TS = V \sum_i f_i\, \varepsilon_i^{\text{id}}\left(T, \frac{n_i}{f_i}\right) - V \sum_{i,j} a_{ij}\, n_i\, n_j \ , \quad (8.5)$$

$$\mu_i(T, \{n_k\}) \equiv \left(\frac{\partial F}{\partial N_i}\right)_{T,V,\{N_{j\neq i}\}} = \mu_i^{\text{id}}\left(T, \frac{n_i}{f_i}\right) + \sum_j \tilde{b}_{ij}\, p_j^{\text{id}}\left(T, \frac{n_j}{f_j}\right)$$

$$- \sum_j (a_{ij} + a_{ji})\, n_j \ , \quad (8.6)$$

where

$$f_i \equiv 1 - \sum_j \tilde{b}_{ji} n_j, \quad (8.7)$$

and where $p_i^{\text{id}}$, $s_i^{\text{id}}$, $\varepsilon_i^{\text{id}}$, and $\mu_i^{\text{id}}$ are the ideal quantum gas expressions for the CE pressure, entropy density, energy density, and chemical potential for $i$th particle species, respectively. They are given as functions of temperature and particle number density.

## 8.2 Grand canonical ensemble formulation

Let us introduce the notations

$$p_i^* \equiv p_i^{\text{id}}\left(T, \frac{n_i}{f_i}\right), \quad n_i^* \equiv n_i^{\text{id}}\left(T, \frac{n_i}{f_i}\right), \quad s_i^* \equiv s_i^{\text{id}}\left(T, \frac{n_i}{f_i}\right), \quad \mu_i^* \equiv \mu_i^{\text{id}}\left(T, \frac{n_i}{f_i}\right).$$
$$(8.8)$$

The following equation follows from the last relation in (8.8) due to the thermodynamical equivalence of the CE and GCE in the thermodynamical limit:

$$\frac{n_i}{f_i} = n_i^{\text{id}}(T, \mu_i^*) \ , \qquad i = 1, \ldots, h \ , \quad (8.9)$$

where $n_i^{\text{id}}(T, \mu_i^*)$ is the GCE ideal gas density at temperature $T$ and chemical potential $\mu_i^*$. Equation (8.9) can be rewritten as the system of linear equations for particle densities $n_i$:

$$\sum_j (\delta_{ij} \;+\; \tilde{b}_{ji}\, n_i^*)\, n_j \;=\; n_i^* \,, \qquad i = 1, \ldots, h \,. \tag{8.10}$$

Equations (8.9) and (8.10) imply that $n_i \equiv n_i(T, \{\mu_i\})$. From above equations one also finds:

$$p_i^* = p_i^{\text{id}}\,(T, \mu_i^*) \;, \quad n_i^* = n_i^{\text{id}}\,(T, \mu_i^*) \;, \quad s_i^* = s_i^{\text{id}}\,(T, \mu_i^*) \;. \tag{8.11}$$

Therefore, the GCE pressure reads

$$p(T, \{\mu_i\}) \;=\; \sum_i p_i^* \;-\; \sum_{i,j} a_{ij}\, n_i\, n_j \,. \tag{8.12}$$

The GCE pressure $p(T, \{\mu_i\})$ can be calculated once all $\mu_i^*$ have been determined. Indeed, the calculations of $p_i^*$ and $n_i^*$ are straightforward, while $n_i$ can be recovered by solving the system of linear equations (8.10). Finally, substituting $p_i^*$ and $n_i$ into (8.12) one obtains the pressure. All other thermodynamical functions in the GCE are obtained from $p(T, \{\mu_i\})$ and its partial derivatives.

The system of equations for $\mu_i^*$ reads

$$\mu_i^* + \sum_j \tilde{b}_{ij}\, p_j^* - \sum_j (a_{ij} + a_{ji})\, n_j = \mu_i \,, \qquad i = 1, \ldots, h \,. \tag{8.13}$$

In general, this system of equations has to be solved numerically. In the present work this system is solved using the Broyden's method. If multiple solutions of equations (8.13) are found then the solution with the largest pressure should be taken according to the Gibbs criterium.

The GCE entropy and energy densities are calculated from the corresponding

partial derivatives of the pressure:

$$s(T, \{\mu_i\}) \equiv \frac{\partial p}{\partial T} = \sum_i f_i \, s_i^* \,, \tag{8.14}$$

$$\varepsilon(T, \{\mu_i\}) \equiv T \left(\frac{\partial p}{\partial T}\right)_{\{\mu_j\}} + \sum_i \mu_i \left(\frac{\partial p}{\partial \mu_i}\right)_{T, \{\mu_{j \neq i}\}} - p = \sum_i f_i \, \varepsilon_i^* - \sum_{ij} a_{ij} \, n_i \, n_j \,, \tag{8.15}$$

where $\varepsilon_i^* = \varepsilon_i^{\mathrm{id}}(T, \mu_i^*)$.

Three applications are considered in order to illustrate the above formalism for the multi-component VDW system.

## 8.3   Asymmetric nuclear matter as a VDW mixture of protons and neutrons

Symmetric nuclear matter was considered in Chapter 6 within the single-component Fermi-Dirac VDW equation for nucleons. Let us consider here a more general case of an asymmetric nuclear matter. The thermodynamic equilibrium in such system can be specified by the temperature, $T$, the proton density, $n_p$, and the neutron density, $n_n$. The two-component Fermi-Dirac VDW equation for protons and neutrons then reads

$$p(T, n_p, n_n) = p_p^{\mathrm{id}}\left(T, \frac{n_p}{f_p}\right) + p_n^{\mathrm{id}}\left(T, \frac{n_n}{f_n}\right)$$
$$- a_{pp} \, n_p^2 - a_{pn} \, n_p \, n_n - a_{np} \, n_n \, n_p - a_{nn} \, n_n^2, \tag{8.16}$$

where $f_p = 1 - \tilde{b}_{pp} \, n_p - \tilde{b}_{np} \, n_n$ and $f_n = 1 - \tilde{b}_{pn} \, n_p - \tilde{b}_{nn} \, n_n$. $p_{p(n)}^{\mathrm{id}}$ is the ideal gas pressure function for protons (neutrons), which includes the spin degeneracy factors $d_p = d_n = 2$. Isospin symmetry is assumed. This implies $m_p = m_n \equiv m_N \simeq 938$ MeV/$c^2$ and $\tilde{b}_{pp} = \tilde{b}_{nn}$, $\tilde{b}_{pn} = \tilde{b}_{np}$, $a_{pp} = a_{nn}$, and $a_{pn} = a_{np}$. The model is determined by four interactions parameters: $\tilde{b}_{pp}$, $\tilde{b}_{pn}$, $a_{pp}$, and $a_{pn}$. These correspond to the isospin-dependent nucleon-nucleon interactions.

It is useful to characterize the asymmetry of the nuclear matter by the proton fraction $y = n_p/(n_p + n_n)$, and the total nucleon density by $n_N = n_p + n_n$.

The $y$ takes values between 0 and 1. The value $y = 1/2$ corresponds to the symmetric nuclear matter, i.e. $n_p = n_n$. In this case the Eq. (8.16) reduces to a single-component VDW equation for nucleons,

$$p(T, n_N, y = 1/2) = p_N^{\text{id}} \left( T, \frac{n_N}{1 - \tilde{b}_{NN} n_N} \right) - a_{NN} n_N^2, \qquad (8.17)$$

where the nucleon ideal gas pressure $p_N^{\text{id}}$ now contains the spin-isospin nucleon degeneracy factor $d_N = 4$, and where

$$a_{NN} = \frac{a_{pp} + a_{pn}}{2} \quad \text{and} \quad \tilde{b}_{NN} = \frac{\tilde{b}_{pp} + \tilde{b}_{pn}}{2}. \qquad (8.18)$$

Equation (8.17) coincides with Eq. (6.2) used in Chapter 6 to describe symmetric nuclear matter. The parameters $a_{NN}$ and $\tilde{b}_{NN}$ are fixed by the properties of the nuclear ground state: $a_{NN} \simeq 329$ MeV fm$^3$ and $\tilde{b}_{NN} \simeq 3.42$ fm$^3$ (see Section 6.2 for details). In this section these $a_{NN}$ and $\tilde{b}_{NN}$ values are preserved. At the same time, the $a_{pn}/a_{pp}$ and $\tilde{b}_{pn}/\tilde{b}_{pp}$ ratios are treated as free parameters. Variations in these ratios correspond to different scenarios for the isospin dependence of the nucleon-nucleon potential.

The nuclear symmetry energy $S(n)$ is an observable sensitive to the isospin part of nucleon-nucleon interactions. It characterizes the dependence of the energy per nucleon $E/A \equiv \varepsilon/n_N - m_N$ on the proton fraction $y$. In the widely used parabolic approximation the $E/A$ is

$$E/A\,(n, y) \approx E/A\,(n, y = 1/2) + 4\,S(n)\,(y - 1/2)^2. \qquad (8.19)$$

The symmetry energy at saturation density is defined as

$$J \equiv S(n_0) = \frac{1}{8} \left. \frac{\partial^2 (E/A)}{\partial y^2} \right|_{n_N = n_0,\, y = 1/2}, \qquad (8.20)$$

and it roughly corresponds to the difference in energy per nucleon at $n_N = n_0 \simeq 0.16$ fm$^{-3}$ between pure neutron matter ($y = 0$) and symmetric nuclear matter ($y = 1/2$).

Dependence of $J$ on different values of the $a_{pn}/a_{pp}$ and $\tilde{b}_{pn}/\tilde{b}_{pp}$ ratios is shown
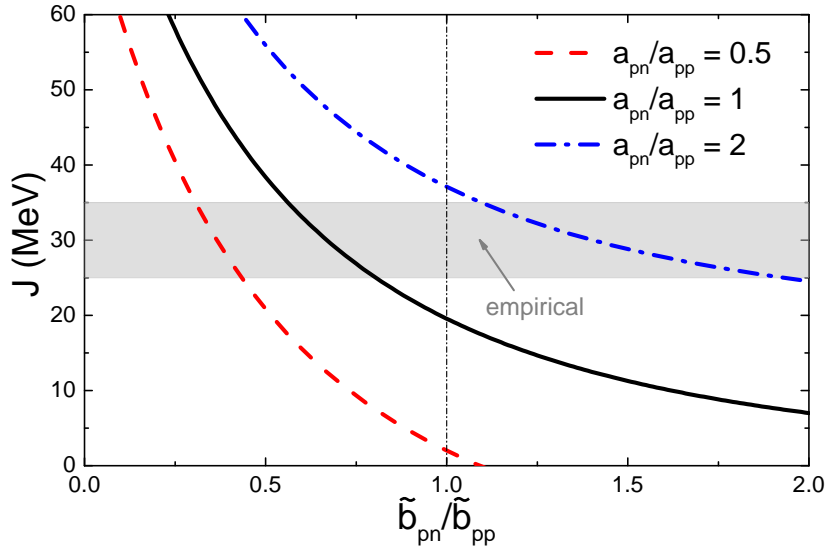
Figure 8.1: Dependence of the symmetry energy $J$ on the ratio $\tilde{b}_{pn}/\tilde{b}_{pp}$ of the repulsive VDW parameters for three different values of the ratio $a_{pn}/a_{pp}$ of the attractive VDW parameters. Both ratios characterize the difference in VDW interactions between the proton-neutron and proton-proton channels.

in Fig. 8.1. A conservative empirical range $J \simeq 25 - 35$ MeV suggested in Ref. [163] is depicted by the shaded area. In the fully symmetric scenario, i.e. for $a_{pp} = a_{pn} = a_{NN}$ and $\tilde{b}_{pp} = \tilde{b}_{pn} = \tilde{b}_{NN}$, the value of symmetry energy $J \simeq 18$ MeV underestimates significantly the empirical estimates. In this case the total symmetry energy value is attributed solely to the decrease of the spin-isospin degeneracy factor, from 4 in symmetric nuclear matter to 2 in pure neutron matter. This mechanism is not sufficient to describe the empirical data. On the other hand, either the increase in $a_{pn}$ or a reduction in $\tilde{b}_{pn}$ leads to an improved agreement with the data.

More stringent restrictions on the values of parameters $a_{pn}$ and $\tilde{b}_{pn}$ can be obtained by analyzing additional observables. These may include the density dependence of the symmetry energy, or the higher order terms of expansion of the $E/A$ (8.19) in terms of the proton fraction $y$. Such studies will be considered elsewhere.

## 8.4    Mixture of interacting nucleons and $\alpha$ particles

Modeling of the nuclear matter should be extended by the inclusion of light nuclei. As a simplest example let us consider a mixture of nucleons and $\alpha$ particles for the case of symmetric nuclear matter, i.e. $n_p = n_n$. Assuming chemical equilibrium, the only conserved quantity is the baryon number $B = N_N + 4N_\alpha$. Thus, the numbers of nucleons, $N_N$, and the number of $\alpha$'s, $N_\alpha$, are not separately conserved. The $N$-$\alpha$ mixture has one independent baryonic chemical potential $\mu$ which regulates the baryonic density $n \equiv n_N + 4n_\alpha$. The chemical potentials of nucleons and alphas are, respectively, $\mu_N = \mu$ and $\mu_\alpha = 4\mu$.

The pressure of the system reads

$$p = p_N^{\mathrm{id}}(T,\mu_N^*) + p_\alpha^{\mathrm{id}}(T,\mu_\alpha^*) - a_{NN}\, n_N^2 - a_{N\alpha}\, n_N n_\alpha - a_{\alpha N}\, n_\alpha n_N - a_{\alpha\alpha}\, n_\alpha^2 \,, \tag{8.21}$$

where

$$p_N^{\mathrm{id}}(T,\mu_N^*) = \frac{g_N}{6\pi^2}\int_0^\infty \frac{dk\,k^4}{\sqrt{m_N^2+k^2}}\left[\exp\left(\frac{\sqrt{m_N^2+k^2}-\mu_N^*}{T}\right)+1\right]^{-1}, \tag{8.22}$$

$$p_\alpha^{\mathrm{id}}(T,\mu_\alpha^*) = \frac{g_\alpha}{6\pi^2}\int_0^\infty \frac{dk\,k^4}{\sqrt{m_\alpha^2+k^2}}\left[\exp\left(\frac{\sqrt{m_\alpha^2+k^2}-\mu_\alpha^*}{T}\right)-1\right]^{-1}, \tag{8.23}$$

with $m_N \cong 938$ MeV and $g_N = 4$, and $m_\alpha \cong 4m_N - 28.3$ MeV and $g_\alpha = 1$. The $\alpha$-particle mass explicitly incorporates the empirically known binding energy of the $\alpha$-particle, equal to about 28.3 MeV.

The system of equations (8.13) for $\mu_N^*$ and $\mu_\alpha^*$ at given $T$ and $\mu$ reads

$$\mu_N^* = \mu - \widetilde{b}_{NN}\, p_N^* - \widetilde{b}_{N\alpha}\, p_\alpha^* + 2\, a_{NN}\, n_N + (a_{N\alpha} + a_{\alpha N})\, n_\alpha \,, \tag{8.24}$$

$$\mu_\alpha^* = 4\mu - \widetilde{b}_{\alpha N}\, p_N^* - \widetilde{b}_{\alpha\alpha}\, p_\alpha^* + 2\, a_{\alpha\alpha}\, n_\alpha + (a_{\alpha N} + a_{N\alpha})\, n_N \,, \tag{8.25}$$

and it is solved numerically.

The VDW parameters which reproduce properties of the nuclear ground state

are employed for nucleons (see Chapter 6):

$$a_{NN} = 329 \text{ MeV fm}^3 \qquad \text{and} \qquad \widetilde{b}_{NN} = 3.42 \text{ fm}^3. \qquad (8.26)$$

In this illustrative study we neglect attractive VDW interactions involving $\alpha$-particles, i.e

$$a_{\alpha\alpha} = a_{\alpha N} = a_{N\alpha} = 0, \qquad (8.27)$$

but we do include repulsive eigenvolume interactions between $\alpha$-$\alpha$ and $\alpha$-$N$ pairs. The eigenvolume parameter of the $\alpha$-particle is taken to be

$$\widetilde{b}_{\alpha\alpha} = 16 \text{ fm}^3, \qquad (8.28)$$

which corresponds to an effective hard-core radius of $r_\alpha \simeq 0.98$ fm. The cross terms are calculated according to (2.15) and (2.17). This gives

$$\widetilde{b}_{\alpha N} \simeq 13.45 \text{ fm}^3 \qquad \text{and} \qquad \widetilde{b}_{N\alpha} \simeq 2.87 \text{ fm}^3. \qquad (8.29)$$

The addition of $\alpha$ particles to the model does not lead to significant changes in the phase diagram of nuclear matter. The phase diagram is very similar to the one obtained previously for the purely nucleonic system (see Figure 6.2 in Chapter 6). There is a slight change in the location of the CP of nuclear matter: the critical temperature $T_c$ increases from 19.68 MeV to 19.89 MeV, and the critical baryon density $n_c$ increases from 0.0723 fm$^{-3}$ to 0.0734 fm$^{-3}$ (see Table 8.1). The mass fraction of $\alpha$-particles, $X_\alpha = 4n_\alpha/(n_N + 4n_\alpha)$, is approximately 1.4% at the CP.

| | $T_c$ (MeV) | $\mu_c$ (MeV) | $n_c$ (fm$^{-3}$) | $p_c$ (MeV $\cdot$ fm$^{-3}$) | $X_\alpha$ |
|---|---|---|---|---|---|
| pure N | 19.68 | 907.67 | 0.0723 | 0.525 | 0 |
| N+$\alpha$ mixture | 19.89 | 907.57 | 0.0734 | 0.562 | 0.014 |

Table 8.1: Thermodynamical properties of the mixture of interacting nucleons and $\alpha$-particles at the critical point (CP). The comparison with the purely nucleonic matter (Chapter 6) is shown.

The behavior of $\alpha$ mass fraction $X_\alpha$ is not trivial. To illustrate this, we show the dependence of $X_\alpha$ on the baryon chemical potential $\mu$ for three different
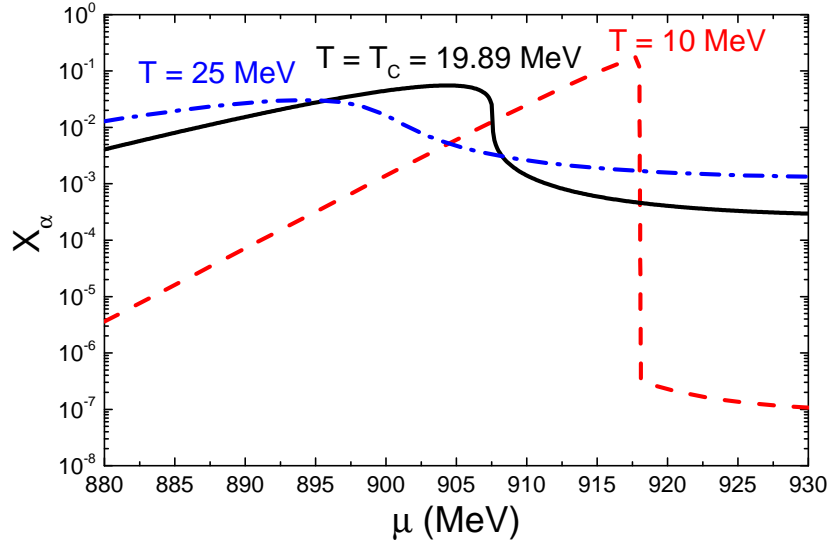
Figure 8.2: Dependence of the $\alpha$ mass fraction $X_\alpha$ on the baryon chemical potential $\mu$ for three different isotherms. The dashed red line corresponds to $T = 10$ MeV, below the critical temperature. The solid black line corresponds to the critical isotherm $T = T_c \simeq 19.89$ MeV. The dash-dotted blue line corresponds to $T = 25$ MeV, above the critical temperature.

isotherms (Figure 8.2).

The dashed red line depicts the isotherm $T = 10$ MeV below the critical temperature. The $X_\alpha$ increases smoothly with chemical potential until reaching the $\mu = \mu_{\mathrm{mix}}$ point of the liquid-gas coexistence curve. At this point, nuclear matter undergoes the first-order phase transition from a relatively dilute gas of nucleons and $\alpha$ particles into a dense liquid composed mainly of nucleons. The $\alpha$ mass fraction drops orders of magnitude at this point. This is caused by the repulsive EV interactions between nucleons and $\alpha$ particles, which suppress the bigger $\alpha$ particles in dense nuclear matter. Note that metastable parts of the $T = 10$ MeV isotherm, which also exist, are not shown in Fig. 8.2.

The behavior of $X_\alpha$ at the critical isotherm $T = T_c$ (solid black line in Fig. 8.2) is qualitatively similar. The $X_\alpha$ undergoes a rapid but continuous drop in the vicinity of the CP. This correlates with a rapid increase of the baryon density with $\mu$ near CP.

Finally, the isotherm $T = 25$ MeV above the critical temperature is shown in Fig. 8.2 by the dash-dotted blue line. The $\mu$-dependence of $X_\alpha$ shows a broad

maximum. This maximum approximately corresponds to the crossover region of the phase diagram (see 6.2), where a rapid but smooth increase of the baryon density with $\mu$ takes place.

The example presented in this subsection elucidates the repulsive VDW interactions as a mechanism for cluster dissolution at high baryon densities. This conclusion is not new: the EV interactions had previously been used in the RMF models of nuclear matter for this purpose [183, 184, 185]. More realistic studies of nuclear matter should take into account the attractive interactions involving the $\alpha$ particles. The effects related to the Bose-Einstein condensation of $\alpha$ particles could play a significant role [186]. Other nuclear clusters such as $d$, $t$, etc. should be included as well. These extensions will be considered elsewhere.

## 8.5 Flavor-dependent VDW interactions in HRG and lattice data at $\mu_B = 0$

As a final example, we consider flavor-dependent VDW interactions in HRG model in the context of the lattice QCD data. The major influence of the baryon-baryon VDW interactions on lattice QCD observables was shown in Chapter 7. Previously we assumed identical VDW interactions for all (anti)baryon pairs. It was possible to model this simplest scenario within essentially a single-component quantum statistical VDW model. At the same time, it is evident that different baryon pairs can have different VDW parameters. In particular, it can be argued that heavier strange hadrons may have a smaller size, owing to smaller cross sections involving these particles [187]. Thermal analysis of the hadron yield data [172] also suggests such a possibility.

In this section we include VDW interactions only for (anti)baryon pairs, similarly to Chapter 7. We extend the VDW-HRG model of Chapter 7 by considering different VDW parameters for non-strange and strange baryons. The VDW parameters obtained in Chapter 6 from a fit to nuclear ground state are employed for pairs of non-strange baryons, i.e.

$$a_{\text{NS}} = 329 \text{ MeV fm}^3 \qquad \text{and} \qquad \widetilde{b}_{\text{NS}} = 3.42 \text{ fm}^3. \qquad (8.30)$$
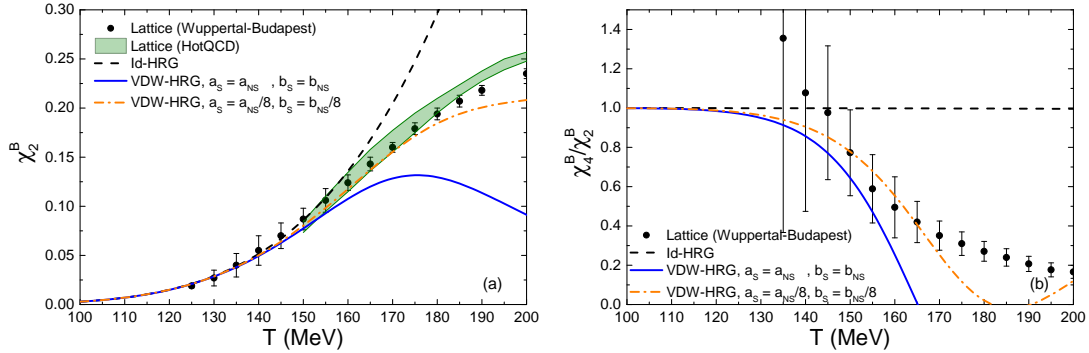
Figure 8.3: The temperature dependence of (a) $\chi_2^B$ and (b) $\chi_4^B/\chi_2^B$ net baryon number susceptibilities, as calculated within Id-HRG (dashed black lines), VDW-HRG with $a_S = a_{NS}$ and $\widetilde{b}_S = \widetilde{b}_{NS}$ (solid blue lines), and VDW-HRG with $a_S = a_{NS}/8$ and $\widetilde{b}_S = \widetilde{b}_{NS}/8$ (dash-dotted orange lines), at zero chemical potential. Lattice QCD results of Wuppertal-Budapest [41, 43] and HotQCD [42] collaborations are shown, respectively, by symbols and green bands.

At the same time, it is assumed that an effective hard-core radius of strange baryons is twice smaller than the one for non-strange baryons. This means that the eigenvolume $b_S$ of a strange baryon is 8 times smaller than eigenvolume $b_{NS}$ of a non-strange baryon. The attractive VDW parameters $a_{NS}$ are also assumed to be smaller compared to the non-strange ones by a common factor of 8:

$$a_S = a_{NS}/8 \simeq 41 \text{ MeV fm}^3 \qquad \text{and} \qquad \widetilde{b}_S = \widetilde{b}_{NS}/8 \simeq 0.43 \text{ fm}^3. \qquad (8.31)$$

Such a parametrization ensures that the difference in VDW parameters between strange and non-strange baryons is significant. Thus, it provides a nice illustration for the multi-component VDW formalism. The repulsive cross term coefficients, characterizing the EV interactions between strange and non-strange baryons, are calculated according to Eqs. (2.15) and (2.17). The attractive cross term coefficients are calculated as a geometric mean, i.e.

$$a_{ij} = \sqrt{a_i\, a_j}. \qquad (8.32)$$

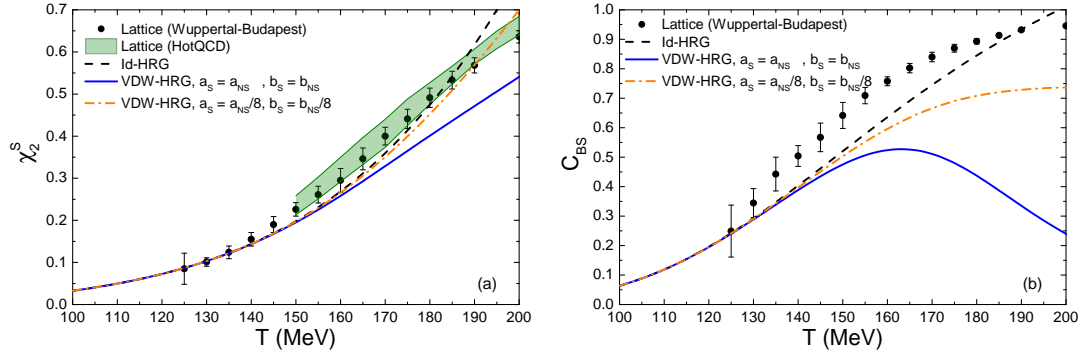This particular mixing rule is motivated by its common use in chemistry [188, 189].

Figure 8.4: The temperature dependence of (a) net-strangeness susceptibility $\chi_2^S$ and (b) baryon-strangeness correlator ratio $C_{BS} = -3\,\chi_{11}^{BS}/\chi_2^S$, as calculated within Id-HRG (dashed black lines), VDW-HRG with $a_S = a_{NS}$ and $\widetilde{b}_S = \widetilde{b}_{NS}$ (solid blue lines), and VDW-HRG with $a_S = a_{NS}/8$ and $\widetilde{b}_S = \widetilde{b}_{NS}/8$ (dash-dotted orange lines), at zero chemical potential. Lattice QCD results of Wuppertal-Budapest [41, 43] and HotQCD [42] collaborations are shown, respectively, by symbols and green bands.

The temperature dependencies of the net baryon susceptibilities $\chi_2^B$ and $\chi_4^B/\chi_2^B$ are calculated within ideal HRG (Id-HRG), VDW-HRG with $a_S = a_{NS}$ and $\widetilde{b}_S = \widetilde{b}_{NS}$, and VDW-HRG with $a_S = a_{NS}/8$ and $\widetilde{b}_S = \widetilde{b}_{NS}/8$, at $\mu = 0$. These dependencies are compared to the lattice QCD data of Wuppertal-Budapest [41] and HotQCD [42] collaborations in Fig. 8.3. The scenario with weaker VDW interactions involving strange baryons yields an improved agreement with the lattice data. This is primarily caused by the decreased overall effect of the repulsive EV interactions.

The strangeness related observables are expected to be more sensitive to modifications involving VDW interactions of strange baryons. We consider the net-strangeness susceptibility $\chi_2^S$ and the baryon-strangeness correlator ratio $C_{BS} = -3\,\chi_{11}^{BS}/\chi_2^S$ to demonstrate this. The latter observable was suggested in Ref. [190] as being particularly sensitive and useful diagnostic for the QCD matter. The calculation results for these two observables are shown in Fig. 8.4. They are compared with corresponding lattice results of Wuppertal-Budapest [41] and HotQCD [42] collaborations.

The standard VDW-HRG model, one with identical VDW parameters for non-strange and strange baryons, does not improve the agreement with the lattice

data compared to the Id-HRG, as already discussed in Chapter 7. In fact, the agreement becomes significantly worse at high temperatures. In the scenario with smaller VDW interactions for strangeness, on the other hand, the existing agreement of Id-HRG is preserved, as seen from Fig. 8.4a.

None of the considered scenarios describe well the lattice data for $C_{BS}$ (Fig. 8.4b): The lattice data are underestimated by all three models. The two VDW-HRG models do show a characteristic inflection point in temperature dependence of the $C_{BS}$, which seems to be present in the lattice data as well. The reduction of VDW interactions for strange baryons yields improved agreement with lattice data. The underestimation of $C_{BS}$ in HRG models may indicate the hitherto undiscovered strange hadrons. Supplementing the conventional HRG with additional, experimentally uncharted strange hadrons predicted by quark model calculations and observed in lattice QCD spectrum calculations was shown to improve agreement between lattice and Id-HRG model for $C_{BS}$ [191]. Similar effect can be expected for the VDW-HRG based models.

# Chapter 9

# Pure glue initial state scenario

This chapter deals with the search for new exotic states of strongly interacting matter, and is loosely connected to other parts of this work. Thus, this part can be read on its own. It describes signatures of the purely gluonic initial state of matter created in high-energy hadron and heavy-ion collisions. Such a scenario was recently proposed in Refs. [31, 32]. Here the results of Refs. [192, 193, 194] are summarized.

## 9.1    Pure glue scenario

The high-energy proton-proton, proton-nucleus, and nucleus-nucleus collisions create extremely excited QCD matter. Proper understanding of the early stage dynamics of these collisions is of great importance in deducing the QCD matter properties from the corresponding experiments. One of the central questions is how the initially highly non-equilibrium system evolves to a state of apparent partial thermodynamic equilibrium at later stages of nuclear collisions. Presently, the community favors a paradigm of an extremely rapid ($t_{\rm eq}$ less than 0.3 fm/c) thermalization and chemical saturation of soft gluons and light quarks, their masses and momenta emerging from the decay of coherent massive color flux tubes of strings, which are formed in the primary hadron-hadron collisions. There exist several models which describe the initial state in terms of non-equilibrium parton cascades [23, 195], minijets [196], color glass condensate [197], coherent chromofields [198, 199] etc.

The large gluon-gluon cross sections lead to the idea [200] that the gluonic components of colliding nucleons interact more strongly than the quark-antiquark ones. As demonstrated in Ref. [201], strong non-equilibrium effects in the gluonic sector persist only for a short time $\sim 1/Q_s$, where $Q_s \simeq 1 - 2$ GeV is the so-called saturation scale [202], but at later times the system reaches a state of a partial thermodynamic equilibrium. The two-step equilibration scenario of the quark-gluon plasma (QGP) was proposed in [203, 204, 205]. It was assumed that the gluon thermalization takes place at the proper time $\tau_g < 1$ fm/$c$ and the (anti)quarks equilibration occurs at $\tau_{\rm th} > \tau_g$. The estimates of Ref. [23] show that $\tau_{\rm th}$ can be of the order of 5 fm/$c$. Later, such a scenario for heavy-ion collisions was considered by several authors, see e.g. [33, 206, 207, 208, 209, 210, 211, 212, 213, 214].

Recently the *pure glue* scenario for the initial state of Pb+Pb collisions at Relativistic Heavy Ion Collider (RHIC) and Large Hadron Collider (LHC) energies was proposed in [31, 32]. Following this idea, let us describe qualitatively the evolution of the idealized purely gluonic matter created in relativistic nuclear collisions.

According to the lattice QCD calculations [215], the quarkless purely gluonic matter should undergo a first-order phase transition at the critical temperature $T_c \simeq 270$ MeV. At this temperature the deconfined pure glue matter transforms into the confined state of the pure Yang-Mills theory, namely into a glueball fluid. Let us assume now that a hot thermalized gluon fluid, containing no (anti)quarks, is created in the initial stage of nuclear collision. As the system cools and expands, it will reach a mixed phase region at $T = T_c$. Only after the initial glue plasma has completely transformed into the glueball fluid will the system cool down further. The heavy glueballs produced during the hadronization process of a pure glue plasma form a glueball gas. It was shown recently that lattice data below $T_c$ is described well by a Hagedorn-Glueball gas with mass-dependent EV interactions [216]. The heavy glueballs will later evolve into the lighter states, presumably via a chain of two-body decays, and finally decay into hadronic resonances and light hadrons. The evolution of the temperature of the system in such a scenario is sketched in the left panel of Fig. 9.1.

Of course, in a more realistic scenario one should take into account that some
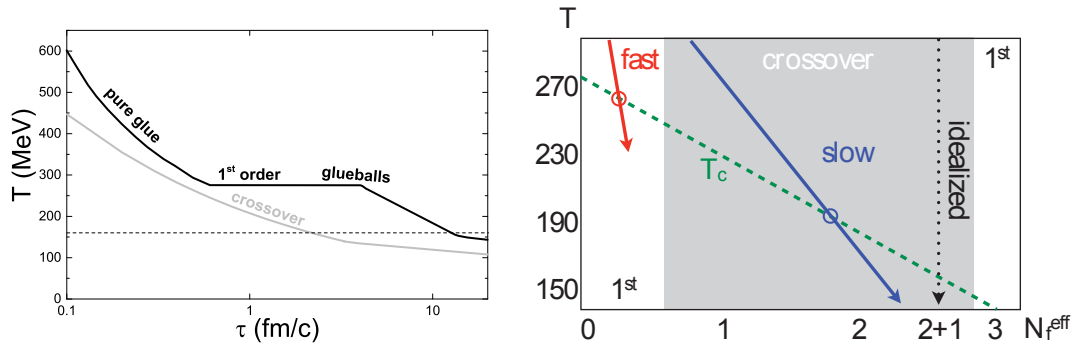
Figure 9.1: *Left panel:* Schematic picture of the temperature evolution in a high-energy collision in the pure glue scenario with Yang-Mills first-order phase transition from gluons to glueballs. The picture is contrasted with evolution within conventional scenario of (2+1)-flavor fully equilibrated QCD. *Right panel:* Transition temperature in the net-baryon free QCD matter versus the effective number of quark flavors. The figure is adapted from Ref. [32].

quarks will be produced already before and during the first-order phase transition. The dynamics of quark production will actually influence the nature of the transition: with increasing number of quark degrees of freedom the temperature of transition will decrease, and at some point the first-order phase transition will instead become a crossover. This is schematically shown in the right panel of Fig. 9.1. The realization of particular scenario certainly depends on the energy and size of the colliding objects. Technically, this scenario can be modeled by introducing the time-dependent effective numbers of quark degrees of freedom, and such a framework is employed in this work to study signatures of the pure glue initial state.

## 9.2 Entropy production in chemically non-equilibrium QGP

In this subsection the evolution of the initially pure glue matter is considered in a framework of the simplest analytical dynamical model: the ideal one-dimensional scaling (Bjorken) hydrodynamics [217].

It is assumed that a thermally (but not necessarily chemically) equilibrated

QGP is formed initially in a nuclear collision. Model parameters typical for central Pb+Pb collisions at the LHC energy of $\sqrt{s_{\text{NN}}} = 2.76$ TeV are used, where the Bjorken-type longitudinally boost-invariant model is expected to provide reasonable description of the early stage dynamics. The equation of state is assumed to be the one of an ideal gas of massless quarks and gluons at zero chemical potential. The deviations from chemical equilibrium for quarks and antiquarks are described by introducing the corresponding (anti)quark fugacity factor $\lambda_q$. At the same time, the deviations from chemical equilibrium for gluons are neglected, assuming that their fugacity is equal to unity during the whole process of the hydro evolution.

This present setup is the simplest possible dynamical description of a pure glue initial scenario which nevertheless allows to obtain analytically some qualitative features which are expected to hold within a more realistic framework. The equation of state in the model reads

$$\varepsilon = 3P = \sigma T^4, \qquad \sigma = \frac{\pi^2}{30}\left(16 + \lambda_q \frac{21}{2} N_f\right), \tag{9.1}$$

where $T$ is the temperature and $N_f = 3$ is the number of quark flavors. The first and second terms in the last equation describe, respectively, the contributions of gluons and quark-antiquark pairs to the energy density. The parameter $\lambda_q$ changes from zero for the pure gluonic system to unity for chemically equilibrated QGP. The solution of the Bjorken hydrodynamical equation reads

$$\varepsilon = \varepsilon(\tau_0)\left(\frac{\tau_0}{\tau}\right)^{4/3}, \tag{9.2}$$

where the parameter $\tau_0$ corresponds to the initial proper time of the hydrodynamic expansion. The solution (9.2) is not new and is identical to the standard chemically equilibrated QGP case. The crucial new element, however, is the explicit *time dependence* of the equation of state, characterized by the time-dependent fugacity factor $\lambda_q(\tau)$. In principle, the $\tau$-dependence of the $\lambda_q$ can be determined by solving additional rate equations [33, 208, 213]. The qualitative

analysis, however, is made simpler by introducing the analytic parametrization

$$\lambda(\tau) \;=\; 1 \;-\; \exp\left(\frac{\tau_0 - \tau}{\tau_*}\right) , \qquad (9.3)$$

where $\tau_*$ is the model parameter characterizing the quark chemical equilibration time. Calculations from different authors give different estimates for $\tau_*$ ranging from $\tau_* \sim 1$ fm$/c$ [214] to $\tau_* \sim 5$ fm$/c$ [23]. One should have in mind, however, that this parameter may depend on the combination of nuclei and the bombarding energy. In the present work the values of $\tau_*$ are varied between 0 (instant equilibration), 1 fm$/c$ (fast equilibration), 5 fm$/c$ (moderate equilibration), and 10 fm$/c$ (slow equilibration).

Introducing the (absolute) quark chemical potential, $\mu_q = T \ln \lambda_q$, and using thermodynamic relations, one can write down the following expression for the entropy density of the chemically undersaturated QGP

$$s \simeq \frac{32\pi^2}{45} T^3 \left[ 1 + \lambda_q \left( \frac{21}{32} - 0.16 \ln \lambda_q \right) N_f \right] . \qquad (9.4)$$

Within the Bjorken model the total entropy per unit space-time rapidity $\eta = \tanh^{-1}(z/t)$ can be expressed as

$$\frac{dS(\tau)}{d\eta} = \pi R_A^2 s(\tau)\tau, \qquad (9.5)$$

where $R_A$ is the geometrical radius of the colliding nuclei. Utilizing the Bjorken solution (9.2) and the time-dependent equation of state one can show that, for a monotonically increasing $\lambda_q(\tau)$, the $s\tau$ is also an increasing function of $\tau$, i.e. $s\tau \geq s_0\tau_0$, where the equality holds only in the equilibrium limit, $\lambda_q = 1$. This fact entails a non-trivial conclusion: the total entropy per unit space-time rapidity is not conserved. Rather, it is gradually increasing during the system expansion from the pure glue initial state. This increase occurs within the ideal hydrodynamics, in absence of viscosity effects, and it is only attributed to an increasing number of degrees of freedom.

In order to illustrate this effect, the calculation results for central Pb+Pb collisions at LHC are performed. The initial energy density at $\tau_0 = 0.1$ fm$/c$ is
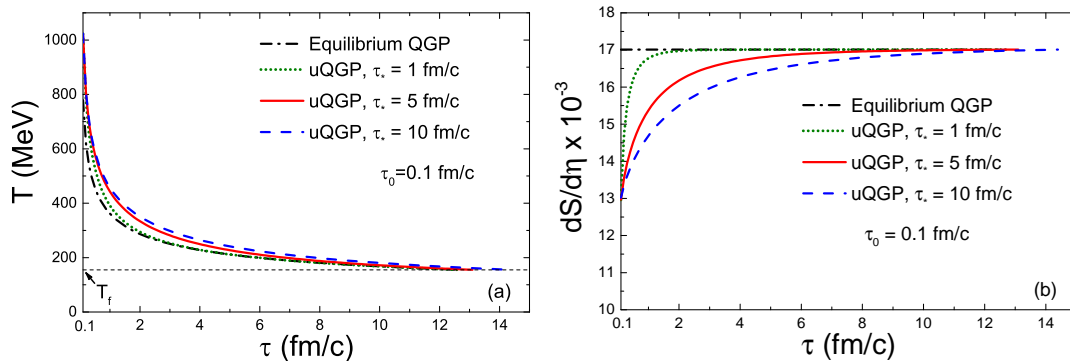
Figure 9.2: The $\tau$-dependence of (a) the temperature and (b) the entropy per unit space-time rapidity of the chemically undersaturated QGP (uQGP) produced in central Pb+Pb collisions ($\sqrt{s_{\mathrm{NN}}} = 2.76$ TeV). The different curves correspond to different values of the quark chemical equilibration time $\tau_*$.

fixed such that final $\frac{dS(\tau)}{d\eta}$ at $T_f \simeq 155$ MeV corresponds to the measured pion yield [85] (see Ref. [192] for more details). The temporal evolution of the temperature and the entropy per unit space-time rapidity is exhibited in Fig. 9.2 for different values of $\tau_*$. One can see that temperature of the chemically undersaturated QGP is noticeably higher than in the equilibrium scenario, especially at $\tau \lesssim \tau_*$. The total entropy per unit space-time rapidity gradually increases and reaches the freeze-out value during the time interval $\Delta\tau \sim \tau_*$. Results show that about 25% of the total entropy is generated during the hydrodynamic expansion. The total entropy increase in insensitive to the value of $\tau_*$ while the characteristic time of this increase process is of the order of $\tau_*$.

It should be stressed that this effect of entropy production is present in ideal hydrodynamics and it is attributed to increasing number of degrees of freedom. This is different from the case of entropy production via dissipative processes which are determined by transport coefficients and usually modeled by the viscous hydrodynamics. The inclusion of chemically nonequilibrium effects may require modification of the viscosity coefficients extracted from the fit of collective flow observables [218, 219].

# 9.3 Electromagnetic probes of a pure glue initial state at LHC

A crucial test of the pure glue initial scenario may be provided by the electromagnetic probes, i.e., by emission of thermal photons and dileptons.

A proper comparison with the experimental data at LHC will require a more realistic setup. For this reason we will now use the longitudinally boost-invariant (2+1)-dimensional hydrodynamics. Its equations are written as

$$\frac{\partial T^{\mu\nu}}{\partial x^\nu} = 0 \,, \tag{9.6}$$

where

$$T^{\mu\nu} = (\varepsilon + P)u^\mu u^\nu - Pg^{\mu\nu} \tag{9.7}$$

is the energy-momentum tensor, $u^\mu$ is the four-velocity, $\varepsilon$ and $P$ are the local rest-frame energy density and pressure, respectively, and $g^{\mu\nu}$ is the metric tensor with $g^{00} = 1$ in Cartesian coordinates $(t, x, y, z)$, with $z$ oriented along the beam axis.

We use the the curvilinear light-cone coordinates $(\tau, x, y, \eta)$[1]. Then, the fluid's four-velocity takes the form $u^\mu = \gamma_\perp(\cosh\eta, \boldsymbol{v}_\perp, \sinh\eta)$, where $\boldsymbol{v}_\perp$ is the transverse velocity in the symmetry plane $z = 0$ and $\gamma_\perp = (1 - v_\perp^2)^{-1/2}$ stands for the transverse Lorentz factor.

A more realistic lattice-based equation of state for chemically non-equilibrium QCD matter is also employed. More specifically, the pressure $P(T, \lambda_q)$ is taken as linear interpolation between the limiting pure glue ($\lambda_q = 0$) and full QCD ($\lambda_q = 1$) cases, i.e.

$$\begin{aligned} P(T, \lambda_q) &= \lambda_q\, P_{\text{QCD}}(T) + (1 - \lambda_q)\, P_{\text{YM}}(T) \\ &= P_{\text{YM}}(T) + \lambda_q\left[P_{\text{QCD}}(T) - P_{\text{YM}}(T)\right], \end{aligned} \tag{9.8}$$

where $P_{\text{QCD}}(T)$ and $P_{\text{YM}}(T)$ are, correspondingly, the lattice QCD equations of

---

[1]The $\tau = \sqrt{t^2 - z^2}$ is the proper time and $\eta = \frac{1}{2}\ln\frac{t+z}{t-z}$ is the space-time rapidity
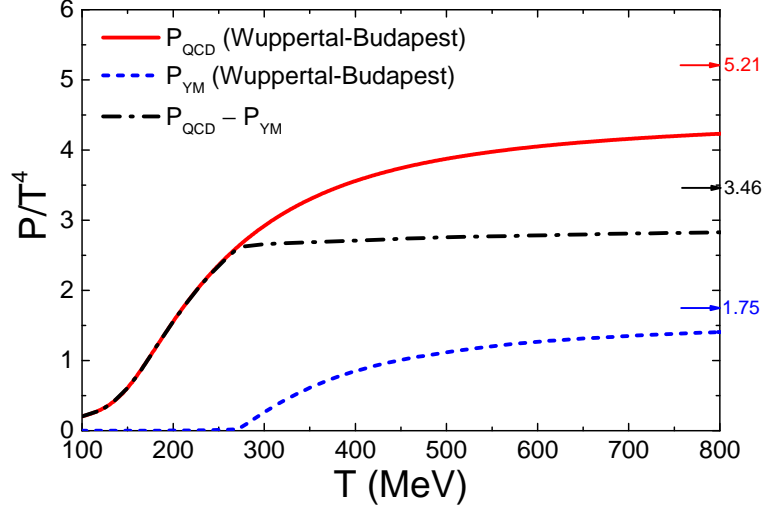
Figure 9.3:    Temperature dependence of the scaled pressure $p/T^4$ obtained in lattice QCD calculations of the Wuppertal-Budapest collaboration for the (2+1)-flavor QCD [12] (red line) and for the Yang-Mills matter [215] (blue line). The black dash-dotted line depicts the difference between the pressure in full QCD and in Yang-Mills theory.

state for (2+1)-flavor full QCD [12] and purely gluonic Yang-Mills (YM) theory [215]. These quantities are depicted in Fig. 9.3. It follows from (9.8) that $P_{\mathrm{YM}}(T)$ plays the role of a partial pressure of gluons in full QCD within this model. Also shown in Fig. 9.3 is the difference $P_{\mathrm{QCD}}(T) - P_{\mathrm{YM}}(T)$, which is present in Eq. (9.8) as a term proportional to $\lambda_q$. By construction, the EoS contains a first-order phase transition at $T = 270$ MeV for all $\lambda_q < 1$. This phase transition gets weaker and weaker as $\lambda_q$ approaches unity.

The parametrization (9.3) for the time dependence of the (anti)quark fugacity $\lambda_q$ is preserved, however, it is now assumed that the temporal argument in (9.3) now corresponds to the local proper time $\tau_P$ of a fluid cell element, which is determined dynamically as the solution to the equation

$$u^\mu \partial_\mu \tau_P(\tau, x, y, \eta) \; = \; 1 \;, \qquad \tau_P(\tau_0, x, y, \eta) \; = \; \tau_0 \;, \tag{9.9}$$

where the parameter $\tau_0$ corresponds to initial longitudinal proper time of the hydrodynamic expansion. This equation is solved simultaneously with the hydrodynamical equations of motion. In general, the $\tau_P$ values are found to be
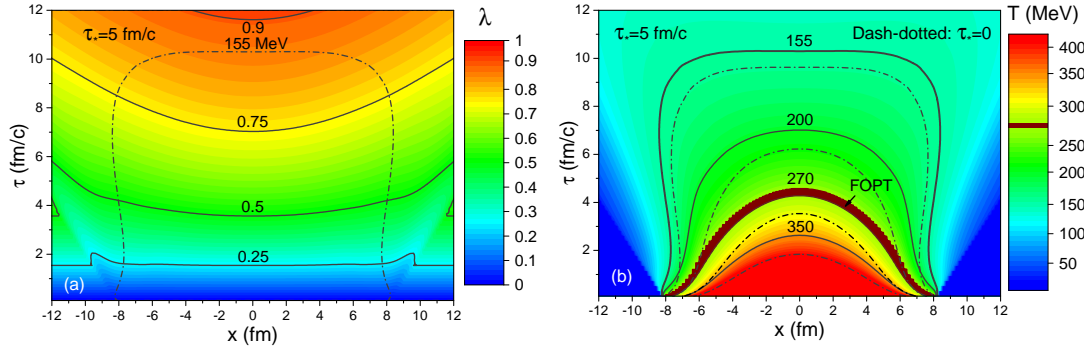
Figure 9.4: The contour plots of the quark fugacity (a) and the temperature (b) in the $x-\tau$ plane for the 0–20% most central Pb+Pb collisions at $\sqrt{s_{NN}} = 2.76$ TeV. The solid curves show contours of $\lambda_q$ and $T$. The dark red region labeled by FOPT corresponds to the mixed-phase region of the first-order phase transition at $T = T_c \simeq 270$ MeV. The dash-dotted curves in (b) depict isotherms calculated for equilibrium QCD matter with $\lambda_q = 1$.

smaller than the 'global' time $\tau$ due to the presence of non-zero transverse flow.

The numerical solution to the hydro equations is obtained with the help of the vHLLE hydrodynamic code [28], modified in order to include the effects of chemical non-equilibrium as described above (see Ref. [193] for more details). The initial conditions are fixed within the event-averaged Glauber Monte Carlo model as described in Refs. [220] and [193].

The contour plot of the quark fugacity $\lambda_q$ in the $x-\tau$ plane is given in Fig. 9.4a. The dashed line shows the isotherm $T = 155$ MeV which presumably corresponds to the hadronization hypersurface. One can see that typical lifetimes of the deconfined phase in the considered reaction do not exceed 10 fm/$c$. One also observes that deviations from chemical equilibrium ($\lambda_q \lesssim 0.9$) may survive up to the hadronization stage. The contour plot of the temperature in the plane $(x, \tau)$ is shown in the right panel of Fig. 9.4. The chemically undersaturated matter has fewer effective degrees of freedom, hence it is much hotter as compared to the equilibrium case, especially at the earlier times.

### 9.3.1 Photons

The emission of direct[2] photons from expanding matter created in relativistic A+A collisions has several components [221, 222]: a) 'prompt' photons from binary collisions of initial nucleons, b) 'thermal' photons from the high-temperature deconfined phase, c) direct photons from the low-temperature hadronic phase. The contribution of prompt photons becomes dominant at large transverse momenta. Unfortunately, this greatly reduces the sensitivity of photon $p_T$-spectra to chemical nonequilibrium effects.

Within the leading order approximation in the strong coupling constant, the following sources of thermal photon production in the deconfined matter are dominant [223]:

1) QCD Compton scattering ($A + g \rightarrow A + \gamma$, where $A = q, \bar{q}$),

2) quark-antiquark annihilation ($q + \bar{q} \rightarrow g + \gamma$),

3) bremsstrahlung reactions ($A + B \rightarrow A + B + \gamma$, where $A = q, \bar{q}$ and $B = q, \bar{q}, g$),

4) 'off-shell' $q\bar{q}$–annihilation with rescatterings of (anti)quark on another parton in the initial state[3]. It is clear that photons can not be produced in a pure glue matter without charged (anti)quark partons.

We denote the invariant photon production rate in the chemically undersaturated QGP as $\Gamma(\widetilde{E}, T, \lambda)$, where $\widetilde{E}$ is the photon energy in the rest frame of the fluid element. In our case of a boost invariant (2+1)–dimensional expansion the invariant yield of thermal photons is calculated as

$$\frac{dN_\gamma^{\text{th}}}{d^2 p_T dY} = \int d^2 x_T \int\limits_{\tau_0}^{+\infty} d\tau\, \tau \int\limits_{-\infty}^{+\infty} d\eta\, \Gamma(\widetilde{E}, T, \lambda)\, \theta(T - T_f)\,, \qquad (9.10)$$

where $p_T$ is the transverse momentum of the photon, $Y$ is its longitudinal rapidity, $\widetilde{E} = \gamma_\perp p_T \big[\cosh(Y - \eta) - v_x \cos\varphi - v_y \sin\varphi\big]$ where $\varphi$ is the angle between $\mathbf{p_T}$ and the reaction plane, and $T_f$ is the minimum (cutoff) temperature, i.e. radiation from fluid cells with $T > T_f$ is considered only.

---

[2]Direct photons are the 'non-cocktail' photons, i.e. those which are not produced in decays of $\pi^0, \eta, \rho, \eta'$, and $\phi$ mesons in the final stage of the reaction.

[3]According to Ref. [224], the next-to-leading order corrections to the rate of photon production in equilibrium QGP do not exceed 20%.
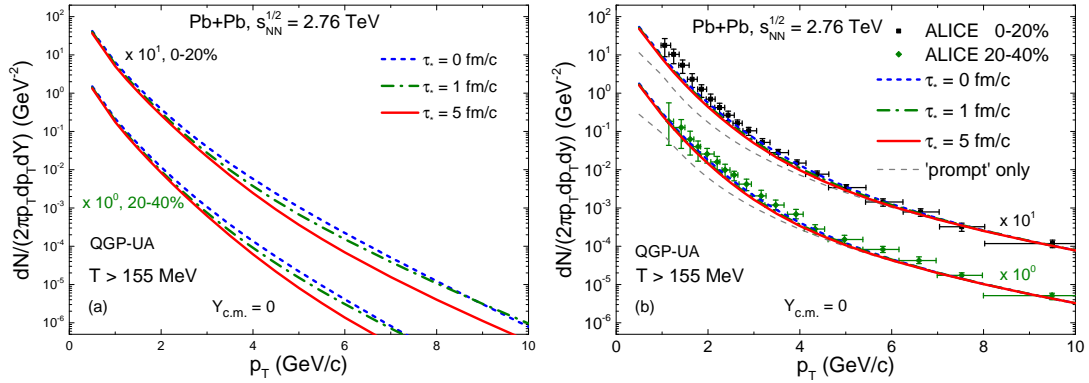
Figure 9.5:    Spectra of (a) thermal and (b) direct photons in the 0–20% and 20-40% central Pb+Pb collisions at $\sqrt{s_{\mathrm{NN}}} = 2.76$ TeV calculated with the cutoff temperature of 155 MeV. The dashed, dash-dotted, and solid curves correspond to $\tau_* = 0, 1$, and 5 fm/$c$, respectively. Dots with error bars show the experimental data [225].

For $\Gamma(\widetilde{E}, T, \lambda)$ the parametrization QGP-UA [193] (based on [223]) of the photon production rate in a chemically nonequilibrium QGP is applied. This parametrization takes into account the suppression of the thermal photon emission rates in undersaturated QGP via the multiplication of the equilibrium rates with the corresponding (anti)quark fugacity factors.

The left panel of Figure 9.5 shows the results for the thermal photon spectrum in the 0–20% and 20–40% central Pb+Pb collisions at $\sqrt{s_{\mathrm{NN}}} = 2.76$ TeV calculated with the cut-off temperature of $T_f = 155$ MeV. The low-$p_T$ spectrum looks very similar in all scenarios, while there is a sizable difference at high $p_T$. The spectra of direct photons, i.e. those that additionally include the prompt photons, is depicted in the right panel of Fig. 9.5. The inclusion of prompt photons makes the difference between different scenarios at high $p_T$ rather small.

The direct photon production in Pb+Pb collisions at LHC has been considered in various theoretical models ([221, 226, 227, 228]. As noted in Ref. [225], the present uncertainties in the heavy-ion photon data at LHC do not allow to conclusively discriminate between the various scenarios.
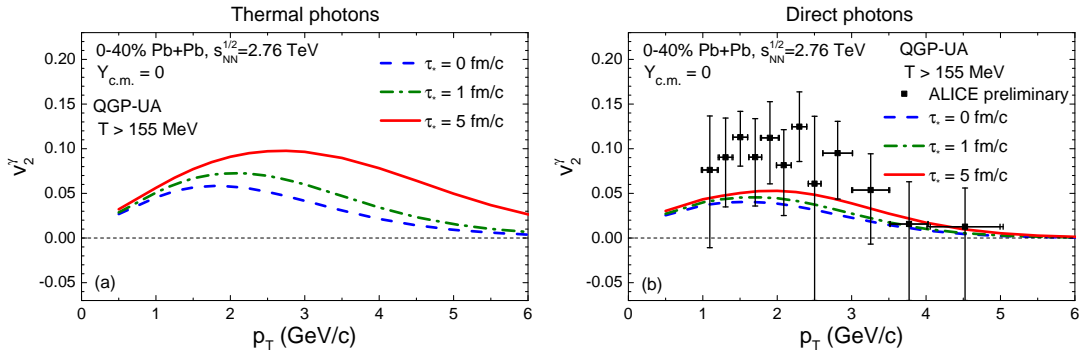
Figure 9.6: Elliptic flow $v_2^\gamma$ of (a) thermal and (b) direct photons as a function of transverse momentum $p_T$ in the $0 - 40\%$ central Pb+Pb collisions at $\sqrt{s_{\mathrm{NN}}} = 2.76$ TeV calculated with the cutoff temperature of 155 MeV. The dashed, dash-dotted, and solid curves correspond to $\tau_* = 0, 1$, and 5 fm/$c$, respectively. Experimental data are taken from Ref. [229].

The photon elliptic flow $v_2^\gamma(p_T)$ is calculated by

$$v_2^\gamma(p_T) = \frac{\int_0^{2\pi} d\varphi \, \frac{dN_\gamma}{d^2 p_T dY} \cos(2\varphi)}{\int_0^{2\pi} d\varphi \, \frac{dN_\gamma}{d^2 p_T dY}} \, . \tag{9.11}$$

The photon spectrum, entering this equation includes both thermal and prompt components. We assume that prompt photons are azimuthally symmetric. Therefore, they contribute only to the denominator of (9.11) reducing $v_2^\gamma$ at large $p_T$. The results of the calculations of the photon elliptic flow are shown in Fig. 9.6. In the pure-glue scenario the momentum anisotropy is significantly enhanced for the high-$p_T$ thermal photons. As seen from Fig. 9.6, the inclusion of prompt photons notably decreases the effect.

## 9.3.2 Dileptons

We also analyze spectra of thermal dileptons produced in nuclear collisions at the LHC energies. It is assumed that dileptons are produced in the $q\bar{q} \to e^+e^-$ processes. The additional factor $\lambda_q^2$ is introduced into the dilepton production rate which takes into account the quark suppression in a chemically nonequilibrium QGP. Thus, the rate of thermal dilepton production in the net baryon-free
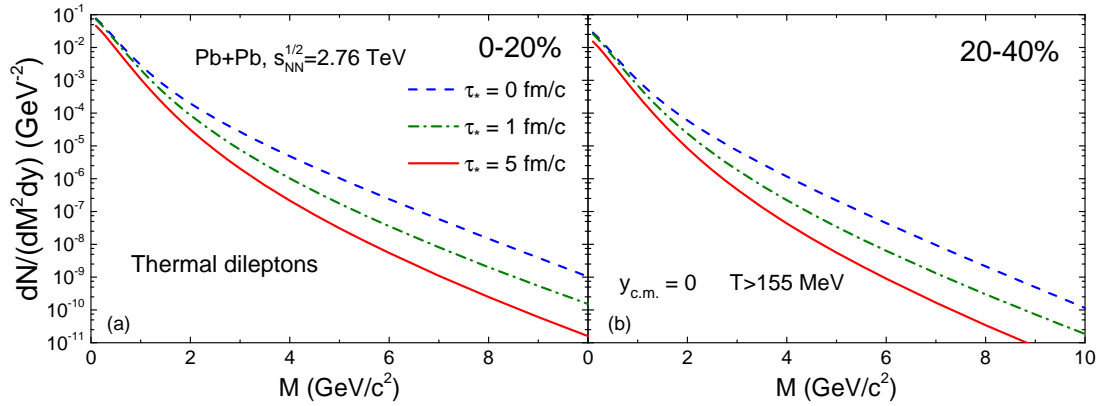
Figure 9.7: Invariant mass distribution of thermal dileptons in (a) 0–20% and (b) 20–40% central Pb+Pb collisions at $\sqrt{s_{\mathrm{NN}}} = 2.76$ TeV calculated for $\tau_* = 0, 1$ and 5 fm/$c$. All results correspond to the cut-off temperature $T_f = 155$ MeV.

undersaturated QGP is (see details in Ref. [193])

$$\frac{dN}{d^4x\, d^4Q} = C_q\, \lambda_q^2\, \exp\left(-\frac{Q\, u}{T}\right), \tag{9.12}$$

where $Q = p_+ + p_-$ is the dilepton total four-momentum, and $T$ and $u$ are, respectively, the local values of temperature and four-velocity of the medium. The rate (9.12) is obtained in the Boltzmann approximation for the (anti)quark phase-space distributions and neglects the quark and lepton masses.

The results of calculating the dilepton mass spectrum in $0-20\%$ and $20-40\%$ central Pb+Pb collisions at $\sqrt{s_{\mathrm{NN}}} = 2.76$ TeV are shown in Fig. 9.7 for the cut-off temperature $T_f = 155$ MeV. One can see that the initial quark suppression leads to a strong reduction of the dilepton yield at $M \gtrsim 2$ GeV. Note that we do not include contributions of hard (Drell-Yan) dileptons [222] produced in binary collisions of initial nucleons.

The elliptic flows of thermal dileptons in the same reaction are shown in Fig. 9.8 for several values of $\tau_*$. Similar to direct photons we predict a strong enhancement of the dilepton elliptic flow as compared to the equilibrium scenario ($\tau_* = 0$).
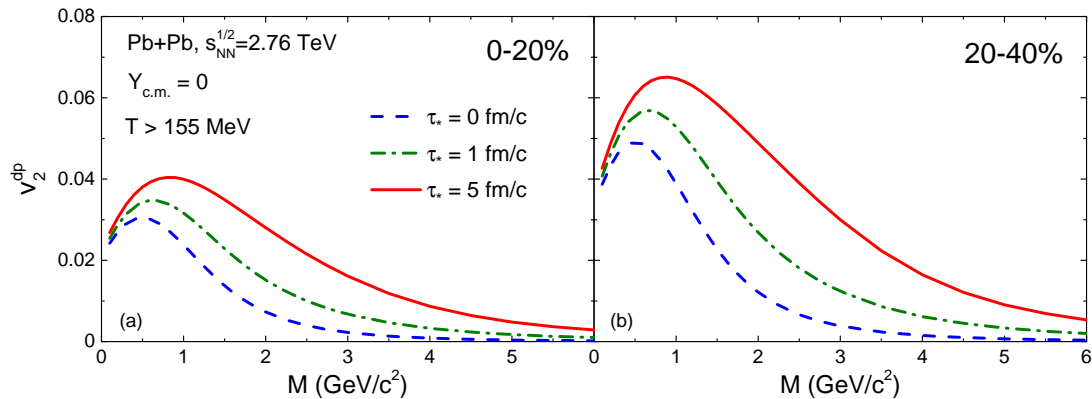
Figure 9.8:   Same as Fig. 9.7 but for elliptic flow of thermal dileptons $v_2^{\mathrm{dp}}$.

## 9.4   Collision energy and system-size scan

The presented calculations, as well as their comparison to experimental data,
show that the pure glue initial scenario does not spoil the existing agreement
of hydro simulations with the data at LHC energies.  On the other hand, the
effect of initial pure gluodynamic evolution, in particular the first-order phase
transition at $T \simeq 270$ MeV, is almost completely washed out in most observables
at LHC energies due to the very long timespan spent in quark production phase.
It is evident that the gluodynamical effects must be more pronounced at lower
collision energies where the initial temperatures are much closer to the critical
temperature $T_c = 270$ MeV of the deconfinement phase transition in the Yang-
Mills theory.

The optimal experimental laboratory conditions to observe the strong effects of
this first-order phase transition can be simply estimated with the one-dimensional
Bjorken model. We consider at first the two limiting cases: the fully equilibrated
(2+1)-flavor evolution and the pure gluodynamic evolution. The corresponding
equations of state, as before, are taken from the lattice QCD simulations.  We
also consider both the heavy-ion ($A + A$) and the smaller $p + p$ systems. Unlike
for LHC energy above, we adopt $\tau_0 = 0.5$ fm/$c$ in the present analysis. The initial
entropy density $s_0$ at a given collision energy is estimated by using the available
experimental data on pion multiplicity. The uncertainties of the obtained results
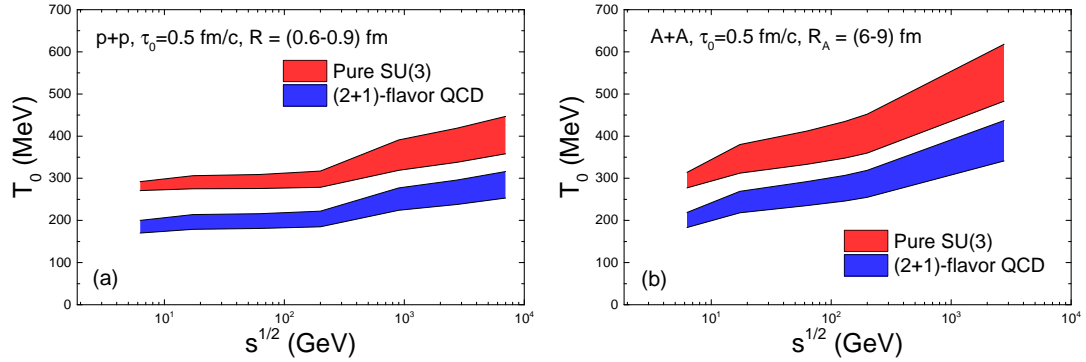are estimated by varying the transverse radius $R$, namely from $R = (6 - 9)$ fm

Figure 9.9: Dependence of the initial temperature $T_0$ at $\tau_0 = 0.5$ fm/$c$ on the collision energy for (2+1)-flavor QCD and pure SU(3) scenarios in (a) $p + p$ and (b) $A+A$ collisions. The uncertainty bands result from variation of the transverse radius.

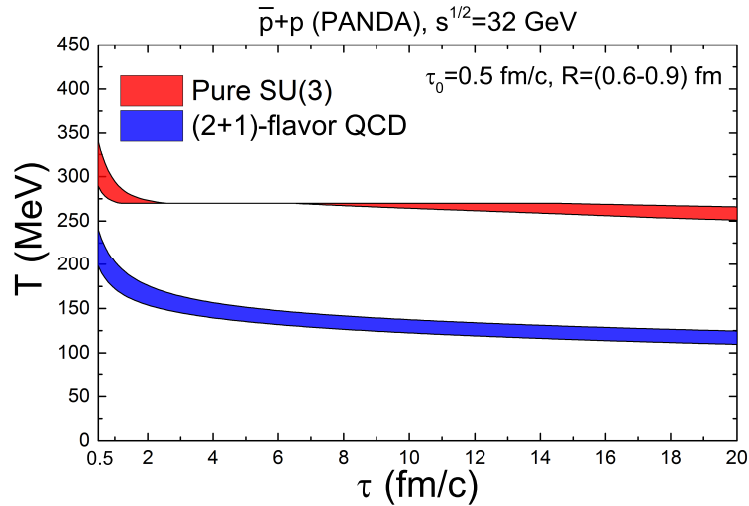for $A + A$ collisions and from $R = (0.6 - 0.9)$ fm for p+p collisions.



Figure 9.10: The $\tau$-dependence of the temperature for (2+1)-flavor QCD and pure SU(3) scenarios in $\bar{p}+p$ collisions at $\sqrt{s_{\mathrm{NN}}} = 32$ GeV. The uncertainty bands result from variation of the transverse radius.

The values of the extracted initial temperature for $p + p$ and $A + A$ are shown in Fig. 9.9. The resulting initial temperature in pure SU(3) case at collision energies $\sqrt{s_{\mathrm{NN}}} \lesssim 100$ GeV is only slightly above the phase transition temperature of $T_c \simeq 270$ MeV. This especially concerns the p+p collisions. Thus, these energies look promising for observing the effects of the phase transition in the pure glue scenario.
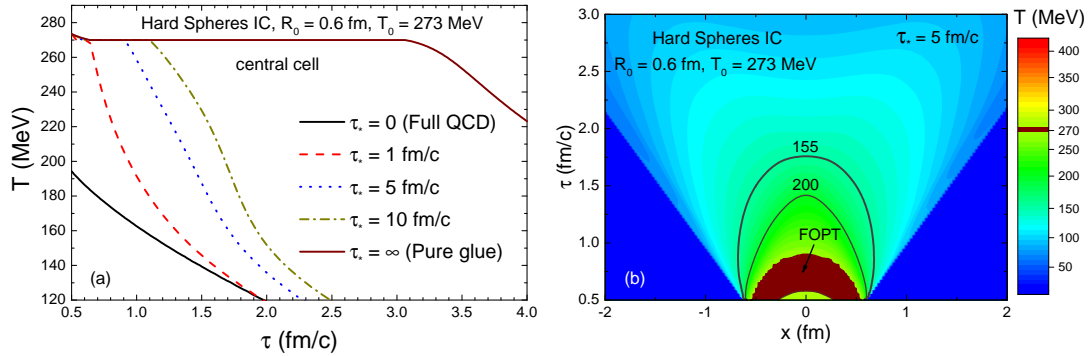
Figure 9.11:   The temperature profile of the longitudinally boost invariant (2+1)-dimensional hydro evolution for $p\bar{p}$ collisions in the pure glue initial state scenario. The hard spheres overlap transverse density profile with radius $R = 0.6$ fm is used as initial condition. The normalization is fixed in order to yield the initial temperature of 273 MeV in the central cell. (a) The $\tau$-dependence of the temperature in the central cell for different quark equilibration times: $\tau_* = 0$ (instant equilibration), 1 fm/$c$ (fast equilibration), 5 fm/$c$ (moderate equilibration), 10 fm/$c$ (slow equilibration), and $\tau_* \to \infty$ (pure gluodynamic evolution). (b) The temperature profile in the $x - \tau$ plane for $\tau_* = 5$ fm/$c$.

This conclusion is supported by more realistic (2+1)-dimensional simulations, which employ time-dependent fugacity factors and use the interpolated lattice QCD equation of state, as described earlier. For these simulations we assume a hard-sphere initial energy density profile with radius $R = 0.6$ fm. The normalization is fixed in order to yield the initial temperature of 273 MeV in the central cell, which is slightly above the critical temperature of 270 MeV. Figure 9.11a shows the $\tau$-dependence of the temperature in the central cell for different quark equilibration times: $\tau_* = 0$ (instant equilibration), 1 fm/$c$ (fast equilibration), 5 fm/$c$ (moderate equilibration), 10 fm/$c$ (slow equilibration), and $\tau_* \to \infty$ (pure gluodynamic evolution). In the pure gluodynamic scenario, $\tau_* \to \infty$, the system spends a very long time in the mixed phase region. A fast quark equilibration shortens the time period spend in the mixed phase significantly. Nevertheless, a significant fraction of system evolution takes place in the mixed phase of the gluon-glueball deconfinement phase transition even with a presence of a moderately fast quark equilibration ($\tau_* = 5$ fm/$c$), as illustrated by Fig. 9.11b. Thus, significant effects of the initial pure glue state on electromagnetic and hadronic observables are expected for this collision setup.

These results illuminate the future HESR-collider option with the central PANDA experiment [230] detector as an exciting upgrade for FAIR: it looks potentially promising in the search of even heavier hadrons and glueballs than previously envisioned, and for new exotic states of matter.

# Chapter 10

# Summary

In this thesis the role of hadronic interactions in the hadronic equation of state, modeled on the basis of the famous van der Waals equation, is studied comprehensively. While the VDW equation is not the most conventional choice for nuclear/hadronic physics applications, the simplicity of the VDW approach makes it extremely useful. This framework allows to include the two most basic ingredients of hadron-hadron interaction: the short-range repulsion, modeled by excluded-volume corrections, and the intermediate range attractions taken in mean-field approximation.

The EV aspect of the HRG model has been explored in the literature before, but rather sparingly. Here a systematic investigation of EV effects on the equation of state and especially on the thermal fits to hadron yield data was presented. A hitherto little known, and surprisingly strong sensitivity of the thermal fits to heavy-ion hadron yield data to the choice of hadron eigenvolumes is uncovered. It is rooted in the little-explored possibility that different hadron species have different eigenvolumes. Obtained results challenge the robustness of the chemical freeze-out temperature and baryochemical potential determination from the thermal fits. At the same time, the extracted values of the entropy per baryon $S/A$ ratio are found to be robust with regards to this systematic uncertainty of the HRG model: extracted $S/A$ values are virtually independent of the details of the modeling of the EV interactions. The Monte Carlo approach to EV interactions which was introduced in this thesis has allowed to study the simultaneous effects of EV and of exact charge conservation in HRG for the first time.

Surprisingly many new aspects and generalizations of the full VDW equation, containing both attractive and repulsive interactions, were uncovered throughout this work. These include the GCE formulation, the generalization to quantum Fermi-Dirac and Bose-Einstein statistics, and extensions to multi-component relativistic systems with fluctuating numbers of particles. In spite of the great phenomenological value of the VDW model, in particular regarding its applications in QCD, these textbook level extensions were never discussed before.

The GCE formulation of the VDW equation allows to obtain the structure of critical fluctuations analytically. The volume-independent ratios of cumulants, namely the scaled variance, skewness, and kurtosis of particle number fluctuations, are calculated and analyzed. These quantities show rich structures around the CP. These results are universal for any classical VDW fluid, and they are also qualitatively consistent with numerical results of various effective QCD theories containing a CP.

The quantum statistical Fermi-Dirac VDW equation for nucleons is applied to describe basic properties of symmetric nuclear matter. The VDW parameters $a$ and $b$ are fixed by reproducing the known properties of the nuclear ground state. The values $a \cong 329 \, \text{MeV} \, \text{fm}^3$ and $b \cong 3.42 \, \text{fm}^3$ are obtained. The resulting model contains the nuclear liquid-gas phase transition and describes basic nuclear matter properties. Further improvement in description of nuclear matter properties can be achieved by considering more involved VDW-like models. This possibility is also illustrated in the present work. The quantum statistical generalization of the VDW equation developed in this thesis is quite general, and can be applied for any fluid. Thus, its applications are not restricted to QCD physics, but may also find themselves in chemistry and/or industry. These are the next future steps.

A particularly interesting result obtained in this work is a strong connection between two seemingly disconnected regions of the QCD phase diagram: the low-temperature, high net baryon density region of nuclear matter, and the high temperature, zero net baryon density region probed by lattice QCD simulations. The inclusion of VDW interactions between baryons into HRG leads to qualitatively different behavior of many lattice observables in the crossover region compared to the widely used ideal HRG. In many cases this behavior resembles closely the lattice data. For instance, the model predicts the drop of the $\chi_4^B / \chi_2^B$

cumulant ratio for the net baryon number fluctuations in the crossover region, which is also seen on the lattice. These results suggest that hadrons do not melt quickly with increasing temperature, as one could conclude on the basis of the commonly performed ideal HRG model analysis. The VDW-HRG model calculations at finite chemical potential also imply that the nuclear liquid-gas phase transition manifests itself into non-trivial fluctuations of the net baryon number in heavy-ion collisions.

Part of the work was devoted to the search of new exotic states of matter. The signatures of the purely gluonic state of matter created in heavy-ion collisions were illustrated in that regard. The hydrodynamical simulations performed in this work show that about 25% of the total final entropy is generated during the hydrodynamic expansion of chemically non-equilibrium, initially pure glue matter. Calculations of photon and dilepton spectra show that existing agreement of models with the experimental data at LHC is not spoiled in the pure glue scenario. The obtained results do suggest a possibility to look for the traces of the chemically non-equilibrium gluon-dominated phase transition in collisions of small-sized nuclei at energies available at the RHIC.

Author hopes that these developments will be useful for practitioners in different fields, and that new exciting discoveries will be achieved on their basis.

# Bibliography

[1] H. Stoecker and W. Greiner, Phys. Rept. **137**, 277 (1986).

[2] P. Koch, B. Muller and J. Rafelski, Phys. Rept. **142**, 167 (1986).

[3] D. Hahn and H. Stoecker, Nucl. Phys. A **476**, 718 (1988).

[4] L.P. Csernai, *Introduction to relativistic heavy ion collisions*, (Wiley, New York, 1994).

[5] C. Y. Wong, *Introduction to high-energy heavy ion collisions*, (World Scientific, Singapore, 1994).

[6] W. Florkowski, *Phenomenology of Ultra-Relativistic Heavy-Ion Collisions*, (World Scientific, Singapore, 2010).

[7] D. J. Gross and F. Wilczek, Phys. Rev. Lett. **30**, 1343 (1973).

[8] H. D. Politzer, Phys. Rev. Lett. **30**, 1346 (1973).

[9] Y. Aoki, G. Endrodi, Z. Fodor, S. D. Katz and K. K. Szabo, Nature **443**, 675 (2006) [hep-lat/0611014].

[10] S. Durr *et al.*, Science **322**, 1224 (2008) [arXiv:0906.3599 [hep-lat]].

[11] K. Fukushima and T. Hatsuda, Rept. Prog. Phys. **74**, 014001 (2011) [arXiv:1005.4814 [hep-ph]].

[12] S. Borsanyi, Z. Fodor, C. Hoelbling, S. D. Katz, S. Krieg and K. K. Szabo, Phys. Lett. B **730**, 99 (2014) [arXiv:1309.5258 [hep-lat]].

[13] A. Bazavov *et al.* [HotQCD Collaboration], Phys. Rev. D **90**, 094503 (2014) [arXiv:1407.6387 [hep-lat]].

[14] P. Braun-Munzinger, K. Redlich and J. Stachel, In Hwa, R.C. (ed.) et al.: Quark gluon plasma 491-599 [nucl-th/0304013].

[15] J. Letessier and J. Rafelski, Eur. Phys. J. A **35**, 221 (2008) [nucl-th/0504028].

[16] F. Becattini, arXiv:0901.3643 [hep-ph].

[17] A. Andronic, Int. J. Mod. Phys. A **29**, 1430047 (2014) [arXiv:1407.5003 [nucl-ex]].

[18] S. A. Bass *et al.*, Prog. Part. Nucl. Phys. **41**, 255 (1998) [Prog. Part. Nucl. Phys. **41**, 225 (1998)] [nucl-th/9803035].

[19] M. Bleicher *et al.*, J. Phys. G **25**, 1859 (1999) [hep-ph/9909407].

[20] W. Cassing and E. L. Bratkovskaya, Phys. Rept. **308**, 65 (1999).

[21] W. Cassing and E. L. Bratkovskaya, Nucl. Phys. A **831**, 215 (2009) [arXiv:0907.5331 [nucl-th]].

[22] Y. Nara, N. Otuka, A. Ohnishi, K. Niita and S. Chiba, Phys. Rev. C **61**, 024901 (2000) [nucl-th/9904059].

[23] Z. Xu and C. Greiner, Phys. Rev. C **71**, 064901 (2005) [hep-ph/0406278].

[24] Z. W. Lin, C. M. Ko, B. A. Li, B. Zhang and S. Pal, Phys. Rev. C **72**, 064901 (2005) [nucl-th/0411110].

[25] P. Huovinen, P. F. Kolb, U. W. Heinz, P. V. Ruuskanen and S. A. Voloshin, Phys. Lett. B **503**, 58 (2001) [hep-ph/0101136].

[26] H. Petersen, J. Steinheimer, G. Burau, M. Bleicher and H. Stocker, Phys. Rev. C **78**, 044901 (2008) [arXiv:0806.1695 [nucl-th]].

[27] C. Gale, S. Jeon and B. Schenke, Int. J. Mod. Phys. A **28**, 1340011 (2013) [arXiv:1301.5893 [nucl-th]].

[28] I. Karpenko, P. Huovinen and M. Bleicher, Comput. Phys. Commun. **185**, 3016 (2014) [arXiv:1312.4160 [nucl-th]].

[29] C. Shen, Z. Qiu, H. Song, J. Bernhard, S. Bass and U. Heinz, Comput. Phys. Commun. **199**, 61 (2016) [arXiv:1409.8164 [nucl-th]].

[30] P. Romatschke, Eur. Phys. J. C **77**, 21 (2017) [arXiv:1609.02820 [nucl-th]].

[31] H. Stoecker *et al.*, J. Phys. G **43**, 015105 (2016) [arXiv:1509.00160 [hep-ph]].

[32] H. Stocker *et al.*, Astron. Nachr. **336**, 744 (2015) [arXiv:1509.07682 [hep-ph]].

[33] T. S. Biro, E. van Doorn, B. Muller, M. H. Thoma and X. N. Wang, Phys. Rev. C **48**, 1275 (1993) [nucl-th/9303004].

[34] K. Geiger and J. I. Kapusta, Phys. Rev. D **47**, 4905 (1993).

[35] J. Cleymans and H. Satz, Z. Phys. C **57**, 135 (1993) [hep-ph/9207204].

[36] J. Cleymans and K. Redlich, Phys. Rev. Lett. **81**, 5284 (1998) [nucl-th/9808030].

[37] J. Cleymans and K. Redlich, Phys. Rev. C **60**, 054908 (1999) [nucl-th/9903063].

[38] F. Becattini, J. Cleymans, A. Keranen, E. Suhonen and K. Redlich, Phys. Rev. C **64**, 024901 (2001) [hep-ph/0002267].

[39] F. Becattini, M. Gazdzicki, A. Keranen, J. Manninen and R. Stock, Phys. Rev. C **69**, 024905 (2004) [hep-ph/0310049].

[40] A. Andronic, P. Braun-Munzinger and J. Stachel, Nucl. Phys. A **772**, 167 (2006) [nucl-th/0511071].

[41] S. Borsanyi, Z. Fodor, S. D. Katz, S. Krieg, C. Ratti and K. Szabo, JHEP **1201**, 138 (2012) [arXiv:1112.4416 [hep-lat]].

[42] A. Bazavov *et al.* [HotQCD Collaboration], Phys. Rev. D **86**, 034509 (2012) [arXiv:1203.0784 [hep-lat]].

[43] R. Bellwied, S. Borsanyi, Z. Fodor, S. D. Katz, A. Pasztor, C. Ratti and K. K. Szabo, Phys. Rev. D **92**, no. 11, 114505 (2015) [arXiv:1507.04627 [hep-lat]].

[44] R. Bellwied, S. Borsanyi, Z. Fodor, S. D. Katz and C. Ratti, Phys. Rev. Lett. **111**, 202302 (2013) [arXiv:1305.6297 [hep-lat]].

[45] R. Dashen, S. K. Ma and H. J. Bernstein, Phys. Rev. **187**, 345 (1969).

[46] R. Hagedorn and J. Rafelski, Phys. Lett. **97B**, 136 (1980).

[47] R. Hagedorn, Z. Phys. C **17**, 265 (1983).

[48] M. I. Gorenstein, V. K. Petrov and G. M. Zinovev, Phys. Lett. **106B**, 327 (1981).

[49] J. I. Kapusta and K. A. Olive, Nucl. Phys. A **408**, 478 (1983).

[50] D. H. Rischke, M. I. Gorenstein, H. Stoecker and W. Greiner, Z. Phys. C **51**, 485 (1991).

[51] L. D. Landau and E. M. Lifshitz, Statistical Physics (Oxford: Pergamon) 1975.

[52] G. D. Yen, M. I. Gorenstein, W. Greiner and S. N. Yang, Phys. Rev. C **56**, 2210 (1997) [nucl-th/9711062].

[53] M. I. Gorenstein, A. P. Kostyuk and Y. D. Krivenko, J. Phys. G **25**, L75 (1999) [nucl-th/9906068].

[54] C. G. Broyden, Mathemathics of Computation **19**, 577 (1965).

[55] CuteHRG package, to be published.

[56] V. Vovchenko, D. V. Anchishkin and M. I. Gorenstein, Phys. Rev. C **91**, 024905 (2015) [arXiv:1412.5478 [nucl-th]].

[57] K. A. Olive *et al.* [Particle Data Group], Chin. Phys. C **38**, 090001 (2014).

[58] L. M. Satarov, V. Vovchenko, P. Alba, M. I. Gorenstein and H. Stoecker, Phys. Rev. C **95**, 024902 (2017) [arXiv:1610.08753 [nucl-th]].

[59] V. Vovchenko, V. V. Begun and M. I. Gorenstein, Phys. Rev. C **93**, 064906 (2016) [arXiv:1512.08025 [nucl-th]].

[60] V. Vovchenko and H. Stoecker, J. Phys. G **44**, 055103 (2017) [arXiv:1512.08046 [hep-ph]].

[61] V. Vovchenko and H. Stoecker, Phys. Rev. C **95**, 044904 (2017) [arXiv:1606.06218 [hep-ph]].

[62] V. Vovchenko, M. I. Gorenstein, L. M. Satarov and H. Stöcker, in "New Horizons in Fundamental Physics" of FIAS Interdisciplinary Science Series, pp. 127-137 (2017) [arXiv:1606.06350 [hep-ph]].

[63] V. Vovchenko and H. Stoecker, J. Phys. Conf. Ser. **779**, 012078 (2017) [arXiv:1610.02346 [nucl-th]].

[64] J. Rafelski, Eur. Phys. J. A **51**, 114 (2015) [arXiv:1508.03260 [nucl-th]].

[65] F. Becattini, J. Manninen and M. Gazdzicki, Phys. Rev. C **73**, 044905 (2006) [hep-ph/0511092].

[66] F. Becattini and G. Passaleva, Eur. Phys. J. C **23**, 551 (2002) [hep-ph/0110312].

[67] S. Wheaton, J. Cleymans and M. Hauer, Comput. Phys. Commun. **180**, 84 (2009) [hep-ph/0407174].

[68] F. James and M. Roos, Comput. Phys. Commun. **10**, 343 (1975).

[69] J. Cleymans, H. Oeschler, K. Redlich and S. Wheaton, Phys. Rev. C **73**, 034905 (2006) [hep-ph/0511094].

[70] A. Andronic, P. Braun-Munzinger and J. Stachel, Phys. Lett. B **673**, 142 (2009) Erratum: [Phys. Lett. B **678**, 516 (2009)] [arXiv:0812.1186 [nucl-th]].

[71] G. Torrieri, S. Steinke, W. Broniowski, W. Florkowski, J. Letessier and J. Rafelski, Comput. Phys. Commun. **167**, 229 (2005) [nucl-th/0404083].

[72] S. V. Afanasiev *et al.* [NA49 Collaboration], Phys. Rev. C **66**, 054902 (2002) [nucl-ex/0205002].

[73] V. Friese [NA49 Collaboration], Nucl. Phys. A **698**, 487 (2002).

[74] C. Alt *et al.* [NA49 Collaboration], Phys. Rev. Lett. **94**, 192301 (2005) [nucl-ex/0409004].

[75] C. Alt *et al.* [NA49 Collaboration], Phys. Rev. C **73**, 044910 (2006).

[76] C. Alt *et al.* [NA49 Collaboration], Phys. Rev. C **77**, 024903 (2008) [arXiv:0710.0118 [nucl-ex]].

[77] C. Alt *et al.* [NA49 Collaboration], Phys. Rev. C **78**, 034918 (2008) [arXiv:0804.3770 [nucl-ex]].

[78] C. Alt *et al.* [NA49 Collaboration], Phys. Rev. C **78**, 044907 (2008) [arXiv:0806.1937 [nucl-ex]].

[79] M. Lorenz [HADES Collaboration], Nucl. Phys. A **931**, 785 (2014).

[80] J. Cleymans, H. Oeschler and K. Redlich, Phys. Rev. C **59**, 1663 (1999) [nucl-th/9809027].

[81] R. Averbeck, R. Holzmann, V. Metag and R. S. Simon, Phys. Rev. C **67**, 024903 (2003) [nucl-ex/0012007].

[82] L. Ahle *et al.* [E-802 Collaboration], Phys. Rev. C **59**, 2173 (1999).

[83] L. Ahle *et al.* [E-802 and E-866 Collaborations], Phys. Rev. C **60**, 044904 (1999) [nucl-ex/9903009].

[84] L. Ahle *et al.* [E802 Collaboration], Phys. Rev. C **60**, 064901 (1999).

[85] B. Abelev *et al.* [ALICE Collaboration], Phys. Rev. C **88**, 044910 (2013) [arXiv:1303.0737 [hep-ex]].

[86] B. B. Abelev *et al.* [ALICE Collaboration], Phys. Rev. Lett. **111**, 222301 (2013) [arXiv:1307.5530 [nucl-ex]].

[87] B. B. Abelev *et al.* [ALICE Collaboration], Phys. Lett. B **728**, 216 (2014) Corrigendum: [Phys. Lett. B **734**, 409 (2014)] [arXiv:1307.5543 [nucl-ex]].

[88] B. B. Abelev *et al.* [ALICE Collaboration], Phys. Rev. C **91**, 024609 (2015) [arXiv:1404.0495 [nucl-ex]].

[89] J. Stachel, A. Andronic, P. Braun-Munzinger and K. Redlich, J. Phys. Conf. Ser. **509**, 012019 (2014) [arXiv:1311.4662 [nucl-th]].

[90] M. Floris, Nucl. Phys. A **931**, 103 (2014) [arXiv:1408.6403 [nucl-ex]].

[91] F. Becattini, E. Grossi, M. Bleicher, J. Steinheimer and R. Stock, Phys. Rev. C **90**, 054907 (2014) [arXiv:1405.0710 [nucl-th]].

[92] P. Braun-Munzinger, I. Heppe and J. Stachel, Phys. Lett. B **465**, 15 (1999) [nucl-th/9903010].

[93] A. Andronic, P. Braun-Munzinger, J. Stachel and M. Winn, Phys. Lett. B **718**, 80 (2012) [arXiv:1201.0693 [nucl-th]].

[94] A. Chodos, R. L. Jaffe, K. Johnson, C. B. Thorn and V. F. Weisskopf, Phys. Rev. D **9**, 3471 (1974).

[95] J. Noronha-Hostler, H. Ahmad, J. Noronha and C. Greiner, Phys. Rev. C **82**, 024913 (2010) [arXiv:0906.3960 [nucl-th]].

[96] M. Albright, J. Kapusta and C. Young, Phys. Rev. C **90**, 024915 (2014) [arXiv:1404.7540 [nucl-th]].

[97] M. Albright, J. Kapusta and C. Young, Phys. Rev. C **92**, 044904 (2015) [arXiv:1506.03408 [nucl-th]].

[98] S. Schuchmann, *PhD Thesis* (University of Frankfurt).

[99] J. Adam *et al.* [ALICE Collaboration], Phys. Rev. C **93**, 024917 (2016) [arXiv:1506.08951 [nucl-ex]].

[100] J. Rafelski and M. Danos, Phys. Lett. **97B**, 279 (1980).

[101] F. Becattini, Z. Phys. C **69**, 485 (1996).

[102] F. Becattini and U. W. Heinz, Z. Phys. C **76**, 269 (1997) Erratum: [Z. Phys. C **76**, 578 (1997)] [hep-ph/9702274].

[103] F. Becattini, L. Bellucci and G. Passaleva, Nucl. Phys. Proc. Suppl. **92**, 137 (2001).

[104] F. Becattini, P. Castorina, A. Milov and H. Satz, Eur. Phys. J. C **66**, 377 (2010) [arXiv:0911.3026 [hep-ph]].

[105] J. Cleymans, K. Redlich and E. Suhonen, Z. Phys. C **51**, 137 (1991).

[106] J. Cleymans, K. Redlich, H. Satz and E. Suhonen, Z. Phys. C **58**, 347 (1993).

[107] M. I. Gorenstein, A. P. Kostyuk, H. Stoecker and W. Greiner, Phys. Lett. B **509**, 277 (2001) [hep-ph/0010148].

[108] V. V. Begun, M. Gazdzicki, M. I. Gorenstein and O. S. Zozulya, Phys. Rev. C **70**, 034901 (2004) [nucl-th/0404056].

[109] M. I. Gorenstein, M. Hauer and D. O. Nikolajenko, Phys. Rev. C **76**, 024901 (2007) [nucl-th/0702081].

[110] J. Fu, Phys. Lett. B **722**, 144 (2013).

[111] P.W. Glynn and D.L. Iglehart, Management Science **35**, 1367 (1989).

[112] F. Becattini and L. Ferroni, Eur. Phys. J. C **35**, 243 (2004) [hep-ph/0307061].

[113] F. Becattini and L. Ferroni, Eur. Phys. J. C **38**, 225 (2004) Erratum: [Eur. Phys. J. **66**, 341 (2010)] [hep-ph/0407117].

[114] N. Abgrall *et al.* [NA61/SHINE Collaboration], Eur. Phys. J. C **74**, 2794 (2014) [arXiv:1310.2417 [hep-ex]].

[115] S. Pulawski [NA61/SHINE Collaboration], PoS CPOD **2014**, 010 (2015) [arXiv:1502.07916 [nucl-ex]].

[116] A. Aduszkiewicz [NA61/SHINE Collaboration], CERN-SPSC-2015-036; SPSC-SR-171, [http://cds.cern.ch/record/2059310].

[117] V. Koch, Chapter of the book "Relativistic Heavy Ion Physics", R. Stock (Ed.), Springer, Heidelberg, 2010, p. 626-652. (Landolt-Boernstein New Series I, v. 23). (ISBN: 978-3-642-01538-0, 978-3-642-01539-7 (eBook)) [arXiv:0810.2520 [nucl-th]].

[118] M. A. Stephanov, K. Rajagopal and E. V. Shuryak, Phys. Rev. D **60**, 114028 (1999) [hep-ph/9903292].

[119] M. Gorenstein, PoS CPOD **2014**, 017 (2015) [arXiv:1505.04135 [nucl-th]].

[120] M. A. Stephanov, K. Rajagopal and E. V. Shuryak, Phys. Rev. Lett. **81**, 4816 (1998) [hep-ph/9806219].

[121] M. Gazdzicki and P. Seyboth, Acta Phys. Polon. B **47**, 1201 (2016) [arXiv:1506.08141 [nucl-ex]].

[122] M. M. Aggarwal *et al.* [STAR Collaboration], Phys. Rev. Lett. **105**, 022302 (2010) [arXiv:1004.4959 [nucl-ex]].

[123] L. Adamczyk *et al.* [STAR Collaboration], Phys. Rev. Lett. **112**, 032302 (2014) [arXiv:1309.5681 [nucl-ex]].

[124] L. Adamczyk *et al.* [STAR Collaboration], Phys. Rev. Lett. **113**, 092301 (2014) [arXiv:1402.1558 [nucl-ex]].

[125] V. Vovchenko, D. V. Anchishkin and M. I. Gorenstein, J. Phys. A **48**, 305001 (2015) [arXiv:1501.03785 [nucl-th]].

[126] V. Vovchenko, R. V. Poberezhnyuk, D. V. Anchishkin and M. I. Gorenstein, J. Phys. A **49**, 015003 (2016) [arXiv:1507.06537 [nucl-th]].

[127] M. A. Stephanov, Phys. Rev. Lett. **102**, 032301 (2009) [arXiv:0809.3450 [hep-ph]].

[128] M. A. Stephanov, Phys. Rev. Lett. **107**, 052301 (2011) [arXiv:1104.1627 [hep-ph]].

[129] B. J. Schaefer and M. Wagner, Phys. Rev. D **85**, 034027 (2012) [arXiv:1111.6871 [hep-ph]].

[130] K. Morita, V. Skokov, B. Friman and K. Redlich, Eur. Phys. J. C **74**, 2706 (2014) [arXiv:1211.4703 [hep-ph]].

[131] S. Chatterjee and K. A. Mohan, arXiv:1502.00648 [nucl-th].

[132] M. I. Gorenstein and M. Gazdzicki, Phys. Rev. C **84**, 014904 (2011) [arXiv:1101.4865 [nucl-th]].

[133] T. Anticic *et al.* [NA49 Collaboration], Phys. Rev. C **92**, 044905 (2015) [arXiv:1509.04633 [nucl-ex]].

[134] A. Aduszkiewicz *et al.* [NA61/SHINE Collaboration], Eur. Phys. J. C **76**, 635 (2016) [arXiv:1510.00163 [hep-ex]].

[135] E. Andronov [NA61/SHINE Collaboration], arXiv:1610.05569 [nucl-ex].

[136] A. Seryakov [NA61/SHINE Collaboration], arXiv:1704.00751 [hep-ex].

[137] M. Gazdzicki, M. I. Gorenstein and M. Mackowiak-Pawlowska, Phys. Rev. C **88**, 024907 (2013) [arXiv:1303.0871 [nucl-th]].

[138] V. Vovchenko, D. V. Anchishkin and M. I. Gorenstein, Phys. Rev. C **91**, 064314 (2015) [arXiv:1504.01363 [nucl-th]].

[139] V. Vovchenko, D. V. Anchishkin, M. I. Gorenstein and R. V. Poberezhnyuk, Phys. Rev. C **92**, 054901 (2015) [arXiv:1506.05763 [nucl-th]].

[140] V. Vovchenko, Phys. Rev. C **96**, 015206 (2017) [arXiv:1701.06524 [nucl-th]].

[141] K. Redlich and K. Zalewski, arXiv:1605.09686 [cond-mat.quant-gas].

[142] L. P. Csernai and J. I. Kapusta, Phys. Rept. **131**, 223 (1986).

[143] J. P. Bondorf, A. S. Botvina, A. S. Ilinov, I. N. Mishustin and K. Sneppen, Phys. Rept. **257**, 133 (1995).

[144] B. D. Serot and J. D. Walecka, Adv. Nucl. Phys. **16**, 1 (1986).

[145] J. Zimanyi and S. A. Moszkowski, Phys. Rev. C **42**, 1416 (1990).

[146] R. Brockmann and R. Machleidt, Phys. Rev. C **42**, 1965 (1990).

[147] H. Mueller and B. D. Serot, Nucl. Phys. A **606**, 508 (1996) [nucl-th/9603037].

[148] M. Bender, P. H. Heenen and P. G. Reinhard, Rev. Mod. Phys. **75**, 121 (2003).

[149] J. E. Finn *et al.*, Phys. Rev. Lett. **49**, 1321 (1982).

[150] R. W. Minich *et al.*, Phys. Lett. **118B**, 458 (1982).

[151] A. S. Hirsch *et al.*, Phys. Rev. C **29**, 508 (1984).

[152] J. Pochodzalla *et al.*, Phys. Rev. Lett. **75**, 1040 (1995).

[153] J. B. Natowitz, K. Hagel, Y. Ma, M. Murray, L. Qin, R. Wada and J. Wang, Phys. Rev. Lett. **89**, 212701 (2002) [nucl-ex/0204015].

[154] V. A. Karnaukhov *et al.*, Phys. Rev. C **67**, 011601 (2003) [nucl-ex/0302006].

[155] J. B. Elliott, P. T. Lake, L. G. Moretto and L. Phair, Phys. Rev. C **87**, 054622 (2013).

[156] M. Asakawa, S. Ejiri and M. Kitazawa, Phys. Rev. Lett. **103**, 262301 (2009) [arXiv:0904.2089 [nucl-th]].

[157] J. W. Chen, J. Deng, H. Kohyama and L. Labun, Phys. Rev. D **93**, 034037 (2016) [arXiv:1509.04968 [hep-ph]].

[158] N.F. Carnahan and K.E. Starling, J. Chem. Phys. **51**, 635 (1969).

[159] O. Redlich and J.N.S. Kwong, Chem. Rev. **44**, 233 (1949).

[160] G. Soave, Chemical Engineering Science **27**, 1197 (1972).

[161] D.-Y. Peng, D. Robinson, Industrial & Engineering Chemistry Fundamentals, **15**, 59 (1985).

[162] J. R. Stone, N. J. Stone and S. A. Moszkowski, Phys. Rev. C **89**, 044316 (2014) [arXiv:1404.0744 [nucl-th]].

[163] M. Dutra *et al.*, Phys. Rev. C **90**, 055203 (2014) [arXiv:1405.3633 [nucl-th]].

[164] W. Broniowski, F. Giacosa and V. Begun, Phys. Rev. C **92**, 034905 (2015) [arXiv:1506.01260 [nucl-th]].

[165] B. Friman, P. M. Lo, M. Marczenko, K. Redlich and C. Sasaki, Phys. Rev. D **92**, 074003 (2015) [arXiv:1507.04183 [hep-ph]].

[166] V. Vovchenko, M. I. Gorenstein and H. Stoecker, arXiv:1609.03975 [hep-ph], Phys. Rev. Lett., in press.

[167] A. Bazavov *et al.*, Phys. Rev. Lett. **111**, 082301 (2013) [arXiv:1304.7220 [hep-lat]].

[168] F. Karsch, Acta Phys. Polon. Supp. **7**, 117 (2014) [arXiv:1312.7659 [hep-lat]].

[169] R. Venugopalan and M. Prakash, Nucl. Phys. A **546**, 718 (1992).

[170] S. Borsányi, PoS LATTICE **2015**, 015 (2016) [arXiv:1511.06541 [hep-lat]].

[171] Wuppertal-Budapest collaboration, in preparation.

[172] P. Alba, V. Vovchenko, M. I. Gorenstein and H. Stoecker, arXiv:1606.06542 [hep-ph].

[173] P. Alba, W. Alberico, R. Bellwied, M. Bluhm, V. Mantovani Sarti, M. Nahrgang and C. Ratti, Phys. Lett. B **738**, 305 (2014) [arXiv:1403.4903 [hep-ph]].

[174] K. Fukushima, Phys. Rev. C **91**, 044910 (2015) [arXiv:1409.0698 [hep-ph]].

[175] A. Mukherjee, J. Steinheimer and S. Schramm, arXiv:1611.10144 [nucl-th].

[176] X. Luo [STAR Collaboration], PoS CPOD **2014**, 019 (2015) [arXiv:1503.02558 [nucl-ex]].

[177] T. Ablyazimov *et al.* [CBM Collaboration], Eur. Phys. J. A **53**, 60 (2017) [arXiv:1607.01487 [nucl-ex]].

[178] P. de Forcrand and O. Philipsen, Nucl. Phys. B **642**, 290 (2002) [hep-lat/0205016].

[179] M. D'Elia and M. P. Lombardo, Phys. Rev. D **67**, 014505 (2003) [hep-lat/0209146].

[180] C. Czaban, F. Cuteri, O. Philipsen, C. Pinke and A. Sciarra, Phys. Rev. D **93**, 054507 (2016) doi:10.1103/PhysRevD.93.054507 [arXiv:1512.07180 [hep-lat]].

[181] J. Gunther, R. Bellwied, S. Borsanyi, Z. Fodor, S. D. Katz, A. Pasztor and C. Ratti, EPJ Web Conf. **137**, 07008 (2017) [arXiv:1607.02493 [hep-lat]].

[182] S. Borsányi *et al.* [Wuppertal-Budapest Collaboration], Talk at Quark Matter 2017 conference (5-11 February 2017, Chicago, USA).

[183] J. M. Lattimer and F. D. Swesty, Nucl. Phys. A **535**, 331 (1991).

[184] H. Shen, H. Toki, K. Oyamatsu and K. Sumiyoshi, Prog. Theor. Phys. **100**, 1013 (1998) [nucl-th/9806095].

[185] S. Typel, Eur. Phys. J. A **52**, no. 1, 16 (2016).

[186] L. M. Satarov, M. I. Gorenstein, A. Motornenko, V. Vovchenko, I. N. Mishustin and H. Stoecker, arXiv:1704.08039 [nucl-th].

[187] M. I. Gorenstein, K. A. Bugaev and M. Gazdzicki, Phys. Rev. Lett. **88**, 132301 (2002) [hep-ph/0112197].

[188] N. C. Patel and A. S. Teja, Chemical Engineering Science **37**, 463 (1982).

[189] J. V. Sengers, R. F. Kayser, C. J. Peters, H. J. White, *Equations of state for fluids and fluid mixtures*, (Elsevier, 2000). Chemical Engineering Science **37**, 463 (1982).

[190] V. Koch, A. Majumder and J. Randrup, Phys. Rev. Lett. **95**, 182301 (2005) [nucl-th/0505052].

[191] A. Bazavov *et al.*, Phys. Rev. Lett. **113**, 072001 (2014) [arXiv:1404.6511 [hep-lat]].

[192] V. Vovchenko, M. I. Gorenstein, L. M. Satarov, I. N. Mishustin, L. P. Csernai, I. Kisel and H. Stöcker, Phys. Rev. C **93**, 014906 (2016) [arXiv:1510.01235 [hep-ph]].

[193] V. Vovchenko, I. A. Karpenko, M. I. Gorenstein, L. M. Satarov, I. N. Mishustin, B. Kämpfer and H. Stoecker, Phys. Rev. C **94**, 024906 (2016) [arXiv:1604.06346 [nucl-th]].

[194] V. Vovchenko *et al.*, PoS BORMIO **2016**, 039 (2016) [arXiv:1608.04318 [nucl-th]].

[195] X. N. Wang and M. Gyulassy, Phys. Rev. D **44**, 3501 (1991).

[196] K. J. Eskola and K. Kajantie, Z. Phys. C **75**, 515 (1997) [nucl-th/9610015].

[197] L. D. McLerran and R. Venugopalan, Phys. Rev. D **49**, 2233 (1994) [hep-ph/9309289].

[198] V. K. Magas, L. P. Csernai and D. D. Strottman, Phys. Rev. C **64**, 014901 (2001) [hep-ph/0010307].

[199] I. N. Mishustin and J. I. Kapusta, Phys. Rev. Lett. **88**, 112501 (2002) [hep-ph/0110321].

[200] L. Van Hove and S. Pokorski, Nucl. Phys. B **86**, 243 (1975).

[201] J. P. Blaizot, F. Gelis, J. F. Liao, L. McLerran and R. Venugopalan, Nucl. Phys. A **873**, 68 (2012) [arXiv:1107.5296 [hep-ph]].

[202] L. V. Gribov, E. M. Levin and M. G. Ryskin, Phys. Rept. **100**, 1 (1983).

[203] S. Raha, Phys. Scripta T **32**, 180 (1990).

[204] E. V. Shuryak, Phys. Rev. Lett. **68**, 3270 (1992).

[205] J. Alam, B. Sinha and S. Raha, Phys. Rev. Lett. **73**, 1895 (1994).

[206] M. Strickland, Phys. Lett. B **331**, 245 (1994).

[207] C. T. Traxler and M. H. Thoma, Phys. Rev. C **53**, 1348 (1996) [hep-ph/9507444].

[208] D. M. Elliott and D. H. Rischke, Nucl. Phys. A **671**, 583 (2000) [nucl-th/9908004].

[209] D. Dutta, S. S. V. Suryanarayana, A. K. Mohanty, K. Kumar and R. K. Choudhury, Nucl. Phys. A **710**, 415 (2002) [hep-ph/0104134].

[210] F. Gelis, H. Niemi, P. V. Ruuskanen and S. S. Rasanen, J. Phys. G **30**, S1031 (2004) [nucl-th/0403040].

[211] F. Scardina, M. Colonna, S. Plumari and V. Greco, Phys. Lett. B **724**, 296 (2013) [arXiv:1202.2262 [nucl-th]].

[212] F. M. Liu and S. X. Liu, Phys. Rev. C **89**, 034906 (2014) [arXiv:1212.6587 [nucl-th]].

[213] A. Monnai, Phys. Rev. C **90**, 021901 (2014) [arXiv:1403.4225 [nucl-th]].

[214] M. Ruggieri, S. Plumari, F. Scardina and V. Greco, Nucl. Phys. A **941**, 201 (2015) [arXiv:1502.04596 [nucl-th]].

[215] S. Borsanyi, G. Endrodi, Z. Fodor, S. D. Katz and K. K. Szabo, JHEP **1207**, 056 (2012) [arXiv:1204.6184 [hep-lat]].

[216] P. Alba, W. M. Alberico, A. Nada, M. Panero and H. Stoecker, Phys. Rev. D **95**, 094511 (2017).

[217] J. D. Bjorken, Phys. Rev. D **27**, 140 (1983).

[218] P. Romatschke and U. Romatschke, Phys. Rev. Lett. **99**, 172301 (2007) [arXiv:0706.1522 [nucl-th]].

[219] H. Niemi, G. S. Denicol, P. Huovinen, E. Molnar and D. H. Rischke, Phys. Rev. Lett. **106**, 212302 (2011) [arXiv:1101.2442 [nucl-th]].

[220] I. A. Karpenko, Y. M. Sinyukov and K. Werner, Phys. Rev. C **87**, 024914 (2013) [arXiv:1204.5351 [nucl-th]].

[221] J. F. Paquet, C. Shen, G. S. Denicol, M. Luzum, B. Schenke, S. Jeon and C. Gale, Phys. Rev. C **93**, 044906 (2016) [arXiv:1509.06738 [hep-ph]].

[222] O. Linnyk, E. L. Bratkovskaya and W. Cassing, Prog. Part. Nucl. Phys. **87**, 50 (2016) [arXiv:1512.08126 [nucl-th]].

[223] P. B. Arnold, G. D. Moore and L. G. Yaffe, JHEP **0112**, 009 (2001) [hep-ph/0111107].

[224] J. Ghiglieri, J. Hong, A. Kurkela, E. Lu, G. D. Moore and D. Teaney, JHEP **1305**, 010 (2013) [arXiv:1302.5970 [hep-ph]].

[225] J. Adam *et al.* [ALICE Collaboration], Phys. Lett. B **754**, 235 (2016) [arXiv:1509.07324 [nucl-ex]].

[226] R. Chatterjee, H. Holopainen, T. Renk and K. J. Eskola, Phys. Rev. C **85**, 064910 (2012) [arXiv:1204.2249 [nucl-th]].

[227] H. van Hees, M. He and R. Rapp, Nucl. Phys. A **933**, 256 (2015) [arXiv:1404.2846 [nucl-th]].

[228] O. Linnyk, V. Konchakovski, T. Steinert, W. Cassing and E. L. Bratkovskaya, Phys. Rev. C **92**, 054914 (2015) [arXiv:1504.05699 [nucl-th]].

[229] D. Lohner [ALICE Collaboration], J. Phys. Conf. Ser. **446**, 012028 (2013) [arXiv:1212.3995 [hep-ex]].

[230] M. F. M. Lutz *et al.* [PANDA Collaboration], arXiv:0903.3905 [hep-ex].

# Acknowledgements

I would like to thank all people who supported me during my doctoral studies.

First of all, I would like express my gratitude to my supervisor Prof. Dr. Horst Stoecker for his constant support, advice, and motivation. Without his help this thesis would never see the light of day. His ability to generate new ideas, and to motivate different people to work together is invaluable. I am very grateful to him for making the research in physics a fun and enjoyable experience.

I am grateful to Prof. Dr. Ivan Kisel for his crucial role in providing me the opportunity to start my Ph.D. in Frankfurt. I gratefully acknowledge his continued encouragement, patience, and understanding throughout my study. I am also thankful for a chance to learn some valuable skills in the modern high performance computing.

I thank my mentor, Dr. Iouri Vassiliev, for his constant and kind support throughout the whole period of my studies. I learned a lot from him about the experimental aspect of the heavy-ion collision physics. I thank Prof. Dr. Peter Senger, my external advisor, for always giving an upright advice, and for all his effort put into running the CBM experiment as smoothly as possible, creating a good working environment for CBM students. I also acknowledge helpful remarks and advice from Prof. Dr. Elena Bratkovskaya, especially at earlier stage of my studies.

I extend my deepest gratitude to my colleagues in Kiev. I thank Prof. Dr. Dmitry Anchishkin, my Master thesis advisor, for bringing me into the field of heavy-ions, for constant encouragement, and for his frequent visits to Darmstadt and Frankfurt during the past few years. I thank Prof. Dr. Mark Gorenstein for very fruitful collaboration, his selfless help, and for really pushing it with the van der Waals equation. I also thank Prof. Dr. Stanislav Yezhov, my initial

# Volodymyr Vovchenko

*Curriculum Vitae*

*Frankfurt Institute for Advanced Studies*
*FIAS 3|101*
☎ *+49-69798-47525*
✉ *vovchenko@fias.uni-frankfurt.de, V.Vovchenko@gsi.de*

---
## Personal Information

| | |
|---|---|
| Date of Birth | March 31, 1990 |
| Place of Birth | Kyiv, Ukraine |
| Citizenship | Ukrainian |

---
## Education

**Since 2014** **PhD Student**, *Johann Wolfgang Goethe University*, Frankfurt am Main, Germany.
Thesis Title: Quantum statistical van der Waals equation and its QCD applications
Supervisor: Prof. Dr. Horst Stoecker
Scholarship through the HGS-HIRe Graduate School for Hadron and Ion Research

**2011–2013** **Master Student**, *Taras Shevchenko National University*, Kyiv, Ukraine, Grade: Excellent.
Subject: Theoretical Physics
Thesis Title: Evolution of the interacting hadronic system in relativistic nucleus-nucleus collisions
Supervisor: Prof. Dr. Dmitry Anchishkin

**2007–2011** **Bachelor Student**, *Taras Shevchenko National University*, Kyiv, Ukraine, Grade: Excellent.
Subject: Physics
Thesis Title: Description of the initial stage of evolution of the nucleon subsystem in relativistic nucleus-nucleus collisions using the Boltzmann equation
Supervisor: Prof. Dr. Dmitry Anchishkin

**2004–2007** **Pupil**, *Ukrainian Physics and Mathathics Lyceum*, Kyiv, Ukraine.

**1997–2004** **Pupil**, *Secondary school #316*, Kyiv, Ukraine.

---
## Experience

**08.2014– 09.2014** **Student**, *CERN School of Computing*, Braga, Portugal.
Attended series of intensive lectures and performed exercises in different subjects of high-performance scientific computing. Obtained a diploma for completing a final exam.

**02.2012– 04.2012** **Intern**, *Institut Matériaux Microélectronique Nanosciences de Provence*, Marseille, France.
Performed quantum chemistry calculations on computer cluster for molecules and polymers sheets. Worked on theoretical description of the time-dependent transport through the quantum dot. Experience working in theoretical and computational research group.

| | |
|---|---|
| 08.2011– 09.2011 | **Summer Student**, *GSI Helmholtz Centre for Heavy Ion Research*, Darmstadt, Germany.<br>Performed algorithm design and implementation (C++) for short-lived particle reconstruction in the CBM experiment. |

## Awards and achievements

| | |
|---|---|
| 2016 | Recipient of the Giersch-Excellence-Grant 2016 for the outstanding work and progress in the PhD thesis project within the past year. |
| 2013 | Award of the National Academy of Sciences of Ukraine for the best scientific works of young scientists and students in 2012. |
| 2011 | Recipient of the grant of the Ministry of Education and Science of Ukraine (Program "100+100+100" for studying and training abroad in 2011/2012). |

## Languages

| | | |
|---|---|---|
| Native | **Ukrainian, Russian** | |
| Advanced | **English** | *Conversationally fluent* |
| Beginner | **German, French** | *Basic words and phrases only* |

## Teaching experience

| | |
|---|---|
| Winter semester 2016/2017 | **Tutorials**, *Physics Department, Johann Wolfgang Goethe University*, Frankfurt am Main, Germany.<br>Title: Classical electrodynamics<br>Level: Bachelor's degree |
| Winter semester 2012/2013 | **Seminars**, *Physics Department, Taras Shevchenko National University*, Kyiv, Ukraine.<br>Title: Methods of mathematical physics<br>Level: Bachelor's degree |

## Publication list

**Journal articles**

1. **V. Vovchenko**, M.I. Gorenstein, and H. Stoecker, *van der Waals Interactions in Hadron Resonance Gas: From Nuclear Matter to Lattice QCD*, Physical Review Letters **118**, 182301 (2017).
2. L.M. Satarov, M.I. Gorenstein, A. Motornenko, **V. Vovchenko**, and H. Stoecker, *Bose-Einstein condensation and liquid-gas phase transition in alpha-matter*, submitted for publication
3. **V. Vovchenko**, *Equations of state for real gases on nuclear scale*, submitted for publication
4. L.M. Satarov, **V. Vovchenko**, P. Alba, M.I. Gorenstein, and H. Stoecker, *New scenarios for hard-core interactions in a hadron resonance gas*, Physical Review C **95**, 024902 (2017).
5. J. Steinheimer, **V. Vovchenko**, J. Aichelin, M. Bleicher, and H. Stoecker, *Conserved charge fluctuations are not conserved during the hadronic phase*, arXiv:1608.03737 [nucl-th], submitted for publication
6. P. Alba, **V. Vovchenko**, M.I. Gorenstein, and H. Stoecker, *Flavor-dependent eigenvolume interactions in hadron resonance gas and its implications for hadron yields at LHC energies*, arXiv:1606.06542 [hep-ph], submitted for publication
7. **V. Vovchenko** and H. Stoecker, *Examination of the sensitivity of the thermal fits to heavy-ion*

*hadron yield data to the modeling of the eigenvolume interactions*, Physical Review C **95**, 044904 (2017).

8. **V. Vovchenko**, Iu.A. Karpenko, M.I. Gorenstein, L.M. Satarov, I.N. Mishustin, B. Kämpfer, and H. Stoecker, *Electromagnetic probes of a pure-glue initial state in nucleus-nucleus collisions at energies available at the CERN Large Hadron Collider*, Physical Review C **94**, 024906 (2016).

9. **V. Vovchenko** and H. Stoecker, *Surprisingly large uncertainties in temperature extraction from thermal fits to hadron yield data at LHC*, Journal of Physics G: Nuclear and Particle Physics **44**, 055103 (2017).

10. **V. Vovchenko**, V.V. Begun, and M.I. Gorenstein, *Hadron multiplicities and chemical freeze-out conditions in proton-proton and nucleus-nucleus collisions* , Physical Review C **93**, 064906 (2016).

11. R.V. Poberezhnyuk, **V. Vovchenko**, D.V. Anchishkin, and M.I. Gorenstein, *Limiting temperature of pion gas with the van der Waals equation of state*, Journal of Physics G: Nuclear and Particle Physics **43**, 095105 (2016).

12. **V. Vovchenko**, M.I. Gorenstein, L.M. Satarov, I.N. Mishustin, L.P. Csernai, I. Kisel, and H. Stoecker, *Entropy production in chemically nonequilibrium quark-gluon plasma created in central Pb+Pb collisions at energies available at the CERN Large Hadron Collider*, Physical Review C **93**, 014906 (2016).

13. H. Stoecker, K. Zhou, S. Schramm, F. Senzel, C. Greiner, M. Beitel, K. Gallmeister, M. Gorenstein, I. Mishustin, D. Vasak, J. Steinheimer, J. Struckmeier, **V. Vovchenko**, L. Satarov, Z. Xu, P. Zhuang, L.P. Csernai, B. Sinha, S. Raha, T.S. Biró, M. Panero, *Glueballs amass at RHIC and LHC Colliders! - The early quarkless 1st order phase transition at T=270 MeV - from pure Yang-Mills glue plasma to GlueBall-Hagedorn states*, Journal of Physics G: Nuclear and Particle Physics **43**, 015105 (2016).

14. **V. Vovchenko**, R.V. Poberezhnyuk, D.V. Anchishkin, and M.I. Gorenstein, *Non-Gaussian particle number fluctuations in vicinity of the critical point for van der Waals equation of state*, Journal of Physics A: Mathematical and Theoretical **49**, 015003 (2016).

15. **V. Vovchenko**, D.V. Anchishkin, M.I. Gorenstein, and R.V. Poberezhnyuk, *Scaled variance, skewness, and kurtosis near the critical point of nuclear matter*, Physical Review C **92**, 054901 (2015).

16. D. Anchishkin and **V. Vovchenko**, *Mean-field approach in the multi-component gas of interacting particles applied to relativistic heavy-ion collisions*, Journal of Physics G: Nuclear and Particle Physics **42**, 105102 (2015).

17. **V. Vovchenko**, D.V. Anchishkin, and M.I. Gorenstein, *Van der Waals equation of state with Fermi statistics for nuclear matter*, Physical Review C **91**, 064314 (2015).

18. **V. Vovchenko**, D.V. Anchishkin, and M.I. Gorenstein, *Particle Number Fluctuations for van der Waals Equation of State*, Journal of Physics A: Mathematical and Theoretical **48**, 305001 (2015).

19. **V. Vovchenko**, D.V. Anchishkin, and M.I. Gorenstein, *Hadron Resonance Gas Equation of State from Lattice QCD*, Physical Review C **91**, 024905 (2015).

20. **V.Yu. Vovchenko**, D.V. Anchishkin, and M.I. Gorenstein, *Mean transverse mass of hadrons in proton-proton reactions*, Nuclear Physics A **936**, 1-5 (2015).

21. **V. Vovchenko**, D. Anchishkin, and L.P. Csernai, *Time dependence of partition into spectators and participants in relativistic heavy-ion collisions*, Physical Review C **90**, 044907 (2014).

22. **V.Yu. Vovchenko**, D.V. Anchishkin, and M.I. Gorenstein, *System-size and energy dependence of particle momentum spectra: The UrQMD analysis of p+p and Pb+Pb collisions*, Physical Review C **90**, 024916 (2014).

23. **V. Vovchenko**, D. Anchishkin, J. Azema, P. Lombardo, R. Hayn, and A.-M. Daré, *A new*

*approach to time-dependent transport through an interacting quantum dot within the Keldysh formalism*, Journal of Physics: Condensed Matter **26**, 015306 (2014).

24. **V. Vovchenko**, D. Anchishkin, and L.P. Csernai, *Longitudinal fluctuations of the center of mass of the participants in heavy-ion collisions*, Physical Review C **88**, 014901 (2013).
25. D. Anchishkin, **V. Vovchenko**, and S. Yezhov, *Hadronic Reaction Zones in Relativistic Nucleus-Nucleus Collisions*, International Journal of Modern Physics E **22**, 1350042 (2013).
26. D. Anchishkin, **V. Vovchenko**, and L.P. Csernai, *Pionic freeze-out hypersurfaces in relativistic nucleus-nucleus collisions*, Physical Review C **87**, 014906 (2013).
27. L. Vovchenko and **V. Vovchenko**, *Simulation of percolation threshold in composites filled with conducting particles of various morphologies*, Materialwissenschaft und Werkstofftechnik **42**, 70-74 (2011).

## Conference proceedings

1. **V. Vovchenko** and H. Stoecker, *Analysis of hadron yield data within hadron resonance gas model with multi-component eigenvolume corrections*, Journal of Physics: Conference Series **779**, 012078 (2017).
2. V.V. Begun, **V. Vovchenko**, and M.I. Gorenstein, *Updates to the p+p and A+A chemical freeze-out lines from the new experimental data*, Journal of Physics: Conference Series **779**, 012080 (2017).
3. P. Alba, **V. Vovchenko**, and H. Stoecker, *Study of hard core repulsive interactions in an hadronic gas from a comparison with lattice QCD*, Journal of Physics: Conference Series **736**, 012022 (2016).
4. H. Stoecker, M. Beitel, T.S. Biró, L.P. Csernai, K. Gallmeister, M.I. Gorenstein, C. Greiner, I.N. Mishustin, M. Panero, S. Raha, L.M. Satarov, S. Schramm, F. Senzel, B. Sinha, J. Steinheimer, J. Struckmeier, **V. Vovchenko**, Z. Xu, K. Zhou, P. Zhuang, *Undersaturation of quarks at early stages of relativistic nuclear collisions: the hot glue initial scenario and its observable signatures*, Astronomische Nachrichten **336**, 744 (2015).
5. D.V. Anchishkin, A.O. Muskeyev, **V.Yu. Vovchenko**, and S.N. Yezhov, *Evolution of the hadronic system created in relativistic nucleus-nucleus collisions*, Problems of Atomic Science and Technology **57**, 115-120 (2012).
6. D. Anchishkin, A. Muskeyev, **V. Vovchenko**, and S. Yezhov, *The space-time structure of relativistic nucleus-nucleus collisions*, Uzhgorod University Scientific Herald. Series: Physics (Visnyk Uzhgorodskogo Universytetu) **29**, 129-134 (2011).